

INVESTIGATION OF THE DYNAMIC OUTCOMES OF BIOPHYSICAL AND
CHEMICAL CELL-TISSUE INTERACTIONS IN VASCULAR ANASTOMOSIS
AND CANCER METABOLISM

A Dissertation

Presented to the Faculty of the Graduate School
of Cornell University

In Partial Fulfillment of the Requirements for the Degree of
Doctor of Philosophy

by

Mengrou Shan

May 2018

© 2018 Mengrou Shan

INVESTIGATION OF DYNAMIC OUTCOMES OF BIOPHYSICAL AND
CHEMICAL CELL-TISSUE INTERACTIONS IN VASCULAR ANASTOMOSIS
AND CANCER METABOLISM

Mengrou Shan, Ph. D.

Cornell University 2018

The functionalities of tissues evolve from the complex cell-cell and cell-tissue interactions. How individual organisms and their collective behaviors impact the global structure and in turn how the dynamics of the whole, shape the individual units remain outstanding research topics in both physiological and pathological contexts – Studies of these topics provide insight into the fundamentals of tissue development and open new routes to therapeutic strategies for various diseases. This thesis is an exploration of several research topics underlying the structural and functional outcomes of multi-scale interactions in tissues using both experimental and computational approaches. This thesis has five chapters. In the first chapter, motivations for each of the studies are discussed. The fundamental concepts involved in these studies are also introduced. The second chapter discusses the first study of the thesis. This study focuses on the understanding of anastomosis during angiogenesis and vasculogenesis and the dynamics of endothelial cells in these processes with an experimental set-up *in vitro*. The third chapter discusses a study aiming to dissect the impact of three common hypotheses in cancer metabolism on solid tumor growth by building a multi-scale modeling platform using various computational tools. The

fourth chapter discusses an experimental study on how breast cancer cells mitigate redox homeostasis in the mitochondria under chronic hypoxia. The final chapter summarizes the concluding remarks and points to future works for these studies.

BIOGRAPHICAL SKETCH

Mengrou Shan was born on June 12, 1990 in Baoding, Hebei, China. Although she is the only child of her parents, Mengrou grew up surrounded by her extended family and friends in a small community. When she was 10, her family moved to Beijing where she attended elementary, middle and high school. Mengrou's tendency of developing various interests appealed at a very young age. At school, she found herself fascinated by mathematics and chemistry. Outside of school, Mengrou was involved in many activities such as painting, singing, calligraphy and dancing. After graduating high school, Mengrou came to the U.S. to pursue higher education at Purdue University. The study experience at Purdue taught her how to be independent, collaborative and persistent. While at Purdue, Mengrou was involved in several research projects as an undergraduate researcher experiencing different aspects of chemical and biomolecular engineering which ultimately inspired her to attend graduate school at Cornell University. At Cornell, she continued to explore different research topics centered on multi-scale cell-tissue interactions under the mentorship of Dr. Abraham Stroock. She was awarded the Fleming Fellowship for 1 year for her work on cancer metabolism. While studying at Cornell, Mengrou also met her future husband, John Heron, whom she shares a passion for science and sense of humor with. Mengrou defended her PhD in Chemical and Biomolecular Engineering in Jan. 2018. She will be joining the Lyssiotis lab at University of Michigan in the Department of Physiology as a postdoctoral researcher. At Michigan, she will continue her exploration in science and venture deeper into the orderly chaos of cancer.

To My Mom, Dad and John

ACKNOWLEDGMENTS

I would like to express my deepest appreciation to many individuals who supported me through the wild journey of graduate school; and more importantly, those who have helped shape me into whom I am today.

First, I would like to thank my advisor, Abe Stroock, who has always been there to motivate, challenge, guide and support me along the way. To me, Abe will always be an inspiring figure in my academic career for his pure passion and pursuit for science and knowledge. I'd like to thank my husband, John, for being there and cheering for me whenever I struggle to pick myself up. I enjoyed very much our many brainstorming sessions and conversations about science. I'd like to thank my parents, without whose support I would not have been able to make it to where I am now. They brought me to this world and enabled me to see so much more that I could have ever asked for. I'd like to acknowledge my former colleagues Arunodai Vudem, David Dai and Michael Lukey, from whom I learnt many computational and experimental skills. I am grateful for their wisdom, insight and help with my projects. Thank you to Dr. Matt Paszek for serving as my minor thesis member and working side-by-side in lab with me to train me on molecular biology. I'd like to thank Dr. Rick Cerione for his generosity of bringing me into his lab and sharing resources with me so I can finish my last study during my last few months at Cornell. Finally, I want to thank all my friends at Cornell for being there: Bill Bedell, Lingfeng Cheng, Kenville Hendrickson, Hanwen Lu, Ghazal Shoorideh, Meghan Smith, and Siyu Zhu.

TABLE OF CONTENTS

Biographical Sketch		iv
Dedication		v
Acknowledgements		vi
Table of Contents		vii
List of Figures		ix
List of Tables		xi
List of Abbreviations		xii
List of Symbols		xvi
Chapter 1	Introduction	1
	1-1 Motivation for studying anastomosis in vitro	1
	1-2 Vascular Development	3
	1-3 Motivation for studying cancer metabolism and mitochondrial redox homeostasis in tumor cells under chronic hypoxia	6
	1-4 Warburg effect	8
	1-5 Reverse Warburg effect	10
	1-6 Glutamine Addiction	11
	1-7 Tumor hypoxia	13
	1-8 References	15
Chapter 2	Endothelial Cell Dynamics during Anastomosis <i>In Vitro</i>	26
	2-1 Introduction	26
	2-2 Results and Discussion	30
	2-3 Materials and Methods	47

2-4	Conclusions	53
2-5	References	54
Chapter 3	Multi-scale Study of Warburg Effect, Reverse Warburg Effect and Glutamine Addiction in Solid Tumors	62
3-1	Introduction	62
3-2	Model	67
3-3	Results	81
3-4	Discussion	96
3-5	Methods	100
3-6	References	107
Chapter 4	Mitochondrial Redox Homeostasis in Breast Cancer Cells under Chronic Hypoxia	121
4-1	Introduction	121
4-2	NADPH Generation in Tumor Cells	122
4-3	Results and Discussion	125
4-4	Conclusions and Future Works	127
4-5	Materials and methods	134
4-6	References	136
Chapter 5	Concluding Remarks and Future Directions	141
5-1	Chapter 2	141
5-2	Chapter 3	143
5-3	Chapter 4	144
5-4	References	146

LIST OF FIGURES

1-1	Vascular development	4
1-2	Blood vessel maturation	6
1-3	Tumor microenvironment	7
1-4	Pasteur effect vs. Warburg effect	9
1-5	Reverse Warburg effect	11
1-6	Major fates of glutamine in tumor cells	12
2-1	Schematic diagrams of anastomosis in homotypic co-culture of endothelial cells	29
2-2	Schematic diagrams of experimental configurations and conditions	31
2-3	Fluorescent confocal sections of angiogenesis and vasculogenesis mono-culture models after 7 days of culture	33
2-4	Fluorescent confocal sections of various configurations after 7 days of culture	35
2-5	Depth distribution of cell populations with time	38
2-6	Comparison across configurations at Day 7	41
2-7	Invasion as a function of time of seeding	45
2-8	Live tracking of individual cells in Mono+Bulk (Medium) on Day 7	46
2-9	Generating PDMS wells for vertical anastomosis assays	50
2-10	Analysis method for vertical anastomosis assays	52
3-1	Multi-scale modeling of cancer metabolism	64
3-2	Metabolic profiles of various cell types in different hypotheses	71
3-3	Distribution of cells in radial simulations	82

3-4	Axial agent-based model of growth of Warburg tumor cells in a perivascular tissue	83
3-5	Warburg tumor cells	86
3-6	Reverse Warburg effect	90
3-7	Glutamine addiction	94
3-8	Full mammalian central metabolic network used in flux balance analysis	101
3-9	Boundary conditions in axial simulations	105
3-10	Calculation of Krogh lengths based on diffusion and zero th order consumption by tumor cells	106
4-1	Major NADP ⁺ /NADPH coupled metabolic pathways in the mitochondria	123
4-2	NADPH regeneration in mitochondrial one-carbon (folate) cycle	124
4-3	Doubling time of breast cancer cell under normoxia vs. hypoxia	128
4-4	Hypoxia induces expression of enzymes associated with glycolysis	129
4-5	Enzymes in one-carbon metabolism are down regulated under prolonged hypoxia	130
4-6	Metabolic enzymes catalyzing reactions coupled with NADP ⁺ /NADPH are down regulated under prolonged hypoxia	131
4-7	Immunoblots of IDH2 and succinyl-CoA synthetase across different basal breast cancer cell lines	132
4-8	Hypothesis of IDH-mediated redox shuttle under prolonged hypoxia in breast cancer cell lines	133
4-9	¹³ C-labeling experiment with U- ¹³ C glutamine under normoxia vs. hypoxia	134

LIST OF TABLES

3-1	Summary of uptake/production rates and yield coefficients of metabolites under different cellular metabolic phenotypes	68
3-2	Summary of simulation parameters	103

LIST OF ABBREVIATIONS

3-D – three-dimensional

3PG – 3-phosphoglycerate

ABM – agent-based model

AcCoA – acetyl coenzyme A

ALDH1L2 – aldehyde dehydrogenase 1 family member L2

α KG – alpha-ketoglutarate

α -SMA – alpha-smooth muscle actin

ATP – Adenosine triphosphate

BCs – bulk cells

bFGF – basic fibroblast growth factor

BM – basement membrane

BO – bulk only

BPTES – Bis-2-(5-phenylacetamido-1,3,4-thiadiazol-2-yl)ethyl sulfide

BSA – bovine serum albumin

CAFs – cancer-associated fibroblasts

DAPI – 4',6-diamidino-2-phenylindole

DW – dry mass

ECGS – endothelial cell growth supplement

ECM – extracellular matrix

ECs – endothelial cells

EDTA – Ethylenediaminetetraacetic acid

EPCs – endothelial progenitor cells

ETC – electron transport chain

FBA – flux balance analysis

FBS – fetal bovine serum

GFP⁺ – green fluorescent protein labeled

GLS (2) – glutaminase (2)

GLUD1/2 – glutamate dehydrogenase 1/2

GLUT1 – glucose transporter 1

GM – growth media

HBPVCs – human brain perivascular cells

HEPES – 4-(2-hydroxyethyl)-1-piperazineethanesulfonic acid

HIF1 α – hypoxia-induced factor 1-alpha

HREs – hypoxic response elements

HUVECs – human umbilical vein endothelial cells

IDH – isocitrate dehydrogenase

iDynoMiCS – individual-based Dynamics of Microbial Communities Simulator

K_i – Half saturation constant of metabolite i

LC-MS – liquid chromatography-mass spectrometry

MB – Mono + Bulk

MCs – monolayer cells

ME – malic enzyme

MeOH – methanol

MgCl₂ – magnesium chloride

MO – monolayer only

MTHFD2/1L/2L – methylene tetrahydrofolate dehydrogenase 2/1-like/2-like

NaCl – sodium chloride

NADH – Nicotinamide adenine dinucleotide

NADPH – Nicotinamide adenine dinucleotide phosphate

NaF – sodium fluoride

NaOH – sodium hydroxide

Na₃VO₄ – Sodium orthovanadate

NH₂ – amide

NNT – nicotinamide nucleotide transhydrogenase

O₂ – oxygen

OAA – oxaloacetate

OXPHOS – oxidative phosphorylation

PBS – phosphate buffered saline

PCs – pericytes

PDGF-B – platelet-derived growth factor subunit B

PDHK1 – pyruvate dehydrogenase kinase 1

PDMS – (poly)-dimethylsiloxane

PEI – (poly)ethylenimine

PHGDH – phosphoglycerate dehydrogenase

PMA – phorbol-12-myristate-13-acetate

PPP – pentose phosphate pathway

QTOP – quadruple time of flight

RFP⁺ – red fluorescent protein labeled

ROS – reactive oxygen species

RW – reverse Warburg

S1P – sphingosine-1-phosphate

SDS – sodium dodecyl sulfate

SHMT2 – serine hydroxymethyl transferase 2

shRNA – short hairpin RNA

TCA – tricarboxylic acid

TME – tumor microenvironment

UDP-GlcNAc – uridine diphosphate N-acetylglucosamine

UHPLC – ultra-high performance liquid chromatography

VEGF – vascular endothelial growth factor

VM – vasculogenesis media

WN – Warburg number

LIST OF SYMBOL

C_i – concentration of i^{th} metabolite

D_i – Diffusion coefficient of i^{th} metabolite

$f_n(C_j)_{Monod}$ – Monod function of metabolite concentrations

$f(z)$ – intensity distribution as a function of depth

I – total intensity of an image

m – index of the pixels

z – index of the depth

μ_l – first moment of the intensity distribution

$\mu_{m/n}$ – maximum growth rate at n^{th} metabolic phenotype of m^{th} cell type

$q_{i/n}$ – uptake/production rate of i^{th} metabolite in the n^{th} phenotype

ρ – dry mass density of the cell

V_m – volume of the cell

X_m – biomass growth of the cell

$Y_{i/n}$ – yield coefficient of i^{th} metabolite in the n^{th} phenotype

CHAPTER 1

INTRODUCTION

1-1 Motivation for studying anastomosis in vitro

The beauty of a living organism is its extreme complexity evolved from the multi-scale interactions of individual units within. Processes including multicellular interactions [1–4], biochemical signaling [3,5–8] and mechanical mechanisms [9–11] work in an integrated manner in development, healing and disease to maintain the health and functionality of the tissue. Studying the fundamental principles of these processes combined with proper engineering designs can provide both fundamental biological insights and lead to the generation of tissues for the study of pathologies and organ replacement therapies, which will significantly improve patient health and quality of life. Among all the components that constitute the complex tissue structure, blood vessel formation (vascularization) is one of the most important and challenging processes that must be addressed. This complex system consists of local microvascular networks and each of them defines the microenvironments within the tissue by enabling transport of oxygen and nutrients. Therefore, vascular development is indispensable in the developmental and adult stages of every tissue type. Additionally, vascularization remains a primary challenge in the reconstruction and repair of biological systems in diseased states, ischemic tissue conditions, and trauma induced loss of vasculature [12]. Specifically, development of perfusable vascular networks for implantation cannot be properly assessed partially due to the poor understanding of

mechanisms involved in anastomosis, a process happens downstream of angiogenesis and vasculogenesis which involves fusion of tip cells and thus allows blood circulation in a closed vascular network (**Fig. 1**). Many investigators have contributed to the understanding of vascularization, specifically anastomosis, by utilizing various models both *in vivo* and *in vitro*. Some studies deserve particular attention: early work by Levenberg *et al.* [13] and Koike *et al.* [14] showed that capillaries could be grown in three-dimensional (3-D) matrices *in vitro* and that these capillaries spontaneously connected (anastomosed) with host vasculature and became functional after implantation in mice. However, these approaches are constrained with respect to the cellular density and dimension of constructs prepared *in vitro* by the diffusion of oxygen (the Krogh length). A recent study by Cheng *et al.* utilized both *in vitro* technique and *in vivo* model to provide insights in mechanical and biomolecular mechanisms involved in anastomosis [15]. Additionally, several studies have looked at vascular networks *in vitro* in a format of 3-D microfluidic devices [16–22]. Specifically, Chrobak *et al.* [22] and Zheng *et al.* [18] have successfully demonstrated large-scale, 3-D, perfusable vascularized tissue *in vitro*. These studies represent a step toward fabrication of thick tissues based on the creation of microvessels that can traverse macroscopic distances and provide connections for the delivery of nutrients and blood. Nevertheless, it remains challenging to bridge from the fabricated microvessels to pervasive capillary structure. Therefore, detailed understanding of the fundamentals in anastomosis needs to be established before moving towards large-scale tissue fabrication *in vitro*. To address this challenge, we propose a simple high-throughput assay that enables occurrence and investigation of anastomosis *in vitro*. In

the first study of this thesis (**Chapter 2**), I will discuss how we introduce a homotypic co-culture system in the aim of properly observing and studying the dynamics of endothelial cells during and post anastomosis *in vitro*. This assay allows for tracking of the dynamics of distinct populations of endothelial cells originating in an endothelium (sprouting angiogenesis) and an adjacent 3-D matrix (vasculogenesis). This strategy provides a new route to the study of anastomosis *in vitro*, elucidates the role of cellular migration within vascular remodeling, and suggests a means to accelerate the vascularization of engineered tissue constructs.

In the following section, I will provide a brief overview of the physiology of vascular development.

1-2 Vascular Development

There are two major processes that define vascular development, vasculogenesis and angiogenesis (**Fig.1**).

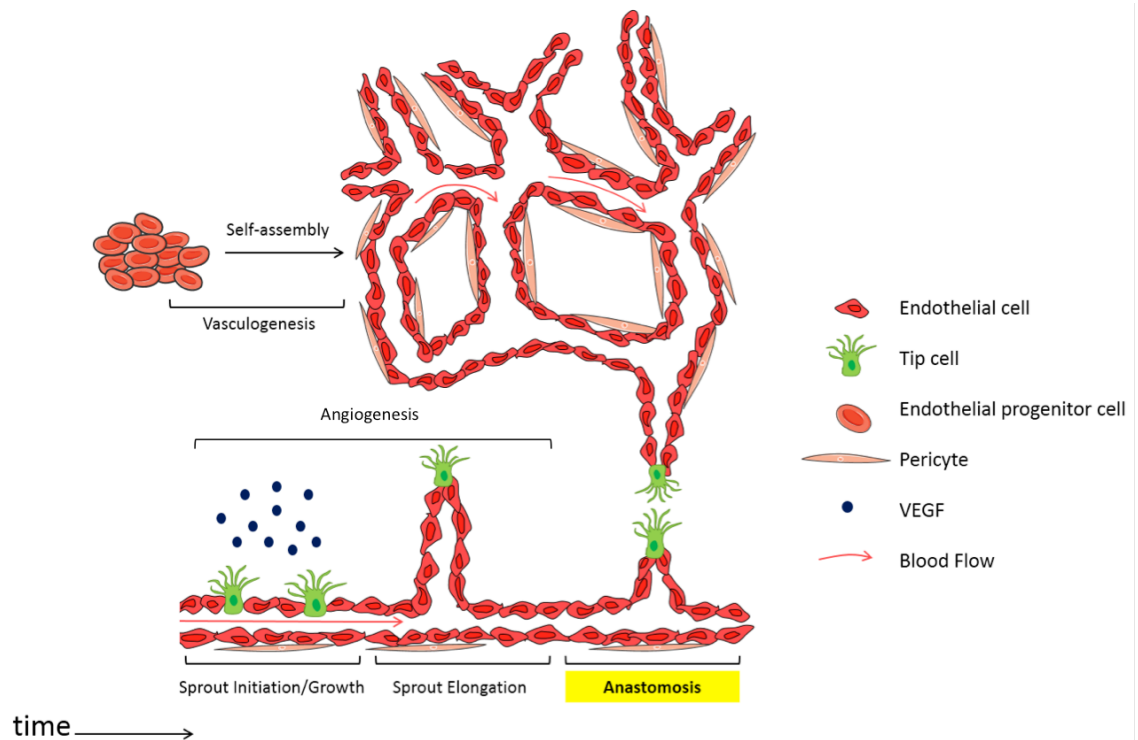


Figure 1-1: Vascular development. Vasculogenesis refers to the process in which endothelial progenitor cells undergo self-assembly to form a primitive vascular network that can further serve as the basis for angiogenesis to initiate from. When the endothelium is exposed to signaling cues such as VEGF, a tip cell is selected and protrudes outwards followed by proliferating stalk cells forming an angiogenic sprout. This process is defined as angiogenesis. Note that angiogenesis does not occur until blood flow is established within the lumen. Both vasculogenesis and angiogenesis require degradation of the ECM by ECs, cell migration and a process called anastomosis (fusion of tip cells).

Vasculogenesis is the process in which endothelial progenitor cells (EPCs) spontaneously assemble into an interconnected capillary vascular network in the three-dimensional extracellular matrix (ECM) [23]. This self-assembly of individual endothelial cells (ECs) involves a series of complex biochemical and mechanical actions of the cells such as paracrine signaling and cellular migration. On the other hand, angiogenesis or sprouting angiogenesis describes the process when endothelial cells sense biochemical cues (e.g. vascular endothelial growth factor, VEGF) and

emerge from pre-existing vascular network to form new blood vessels (**Fig. 1**). Each angiogenic sprout is led by a tip cell followed by stalk cells forming a luminal structure behind it [24]. It has been demonstrated that the tip-stalk interaction is very dynamic and the tip cell is repeatedly replaced by an adjacent stalk cell to lead the protrusion [25]. At late stage (i.e. maturation of the vessels) of both processes, when two tip cells encounter one another, the fusion of the two occurs – a process termed anastomosis, to allow properly closed blood circulation (**Fig. 1**). This process during the maturation of the vascular network is also accompanied by recruitment of surrounding mural cells and deposition of the basement membrane (**Fig. 3**) [26]. There are two types of mural cells, smooth muscle and pericytes. Smooth muscle cells are associated with large vessels such as arteries and veins whereas pericytes are observed in the microvessels such as capillaries. These perivascular mural cells interact with endothelial cells closely during maturation promoting the stability and functionality of the blood vessels [2,26,27].

In **Chapter 2**, I will discuss how we manipulate the aforementioned components during vascular development to establish anastomosis *in vitro* and how we use such a platform to observe endothelial cell dynamics in these vascular processes.

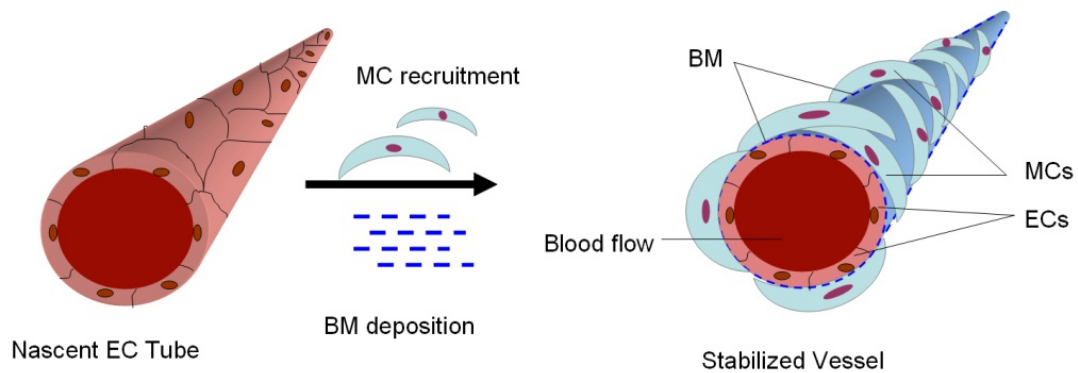


Figure 1-2: Blood vessel maturation. During the maturation of blood vessels, endothelial cells deposit basement membranes and secrete growth factors such as platelet-derived growth factor subunit B (PDGF-B) to recruit surrounding mural cells. Both events promote the stability and normal function of the blood vessel. (Adapted from Jiang and Brey, 2011; [28])

1-3 Motivation for studying cancer metabolism and mitochondrial redox homeostasis in tumor cells under chronic hypoxia

The battle between the human race and cancer has been on for centuries. In the past few decades, modern science and technology have significantly advanced our understanding of cancer, leading to important advances in both diagnostic and therapeutic strategies. However, cancer remains a leading cause of death worldwide [29]. The difficulties of treating cancer come from not only the complexity of tumor cells themselves, but also the rich, highly organized milieu that surrounds tumor cells – the tumor microenvironment.

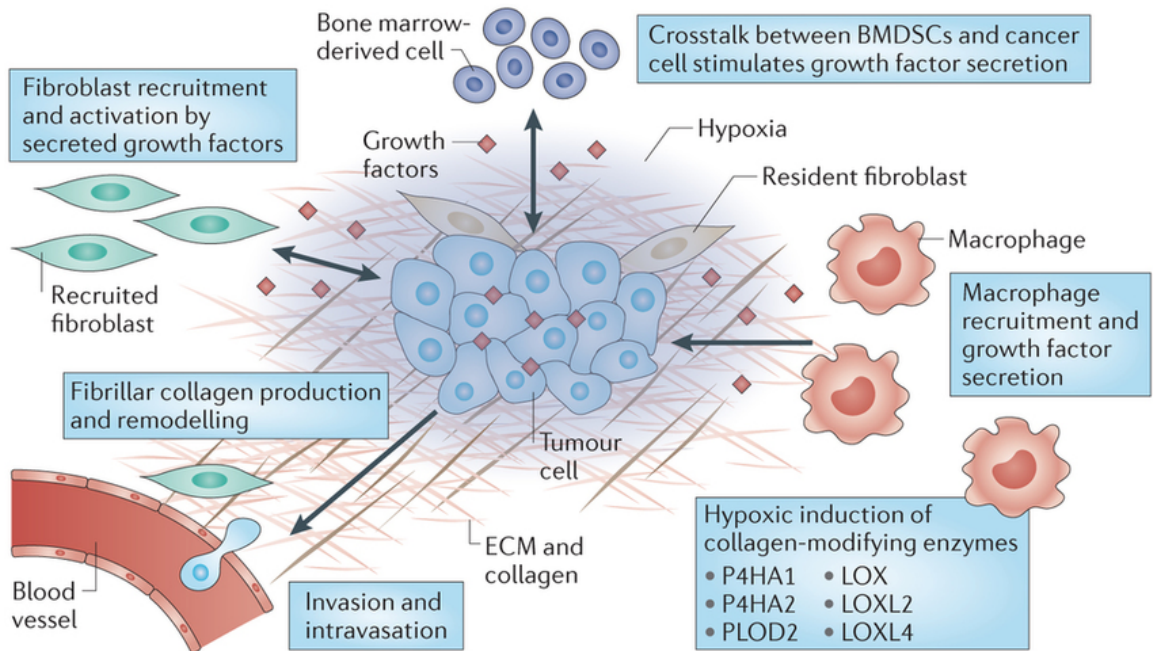


Figure 1-3: Tumor microenvironment. Tumors evolve in a functionally multifaceted microenvironment that interacts with tumor cells closely and dynamically. Cell types in the tumor microenvironment include immune cells, endothelial cells, fibroblasts etc. These cells are often influenced by tumor cells epigenetically and promote tumor progression at different stages. Additionally, tumor cells are known to modify the stiffness of the ECM, pH level, concentrations of metabolites, and signaling molecules in their surroundings through interaction with the microenvironment to further advance in growth. (Adapted from Gilkes, Semenza and Wirtz, 2014; [30])

The tumor microenvironment has been overlooked in cancer research for a long time. It wasn't until recently (~20 years ago) that biophysicists and bioengineers in cancer research started to recognize the importance of tumor microenvironment in tumor progression (**Fig. 3**) [31].

Indeed, tumors are not simply clones of tumor cells. In normal physiology, tissue is composed of various cells types and the ECM. Tissues further serve as the structural and functional units to form organs by joining together in an interconnected and organized way [32]. Interestingly, tumors resemble organs but with their own

abnormal ecology – the complex interactions between different cell types and ECM in solid tumors contribute to tumor progression in ways that resemble organ development. For example, uncontrolled proliferation of tumor cells requires adequate delivery of nutrients through the vascular network. As tumor mass quickly expands, local depletion of metabolites leads to hypoxic regions in tumor tissue, impacting the metabolism of both tumor cells and the supporting stromal cells, as well as promoting tumor angiogenesis in the long term [33]. Therefore, understanding how tumor cells adapt to/manipulate their microenvironment (e.g. through exchange of metabolites) and how the microenvironmental factors such as hypoxia impact tumor progression may open up new routes for therapeutic interventions to treating cancer.

In **Chapter 3**, I will discuss how we interpret popular hypotheses in cancer metabolism, namely the Warburg effect, the reverse Warburg effect and glutamine addiction with mathematical descriptions and investigate their impact on solid tumor growth using a multi-scale modeling platform.

In **Chapter 4**, I will discuss how tumor cells adapt to chronic hypoxia by rewiring their metabolic pathways to mitigate redox stress in mitochondria using different basal breast cancer cell lines.

1-4 Warburg effect

Almost a century ago, Otto Warburg observed that tumor cells present a distinct metabolic phenotype in which they maintain high levels of glycolytic fermentation, an energetically unfavorable metabolic pathway, even in the presence of oxygen [34]. This observation has since been termed as aerobic glycolysis, also known as the Warburg effect (**Fig. 4**). This initial observation subsequently led Warburg to

hypothesize that tumor cells develop from normal cells with an irreversible injuring of respiration followed by a reliance on glycolysis to replace the irretrievably lost respiration energy [35]. However, recent work showed that most cancer cells retain their mitochondrial function, pointing to the indispensable role of aerobic glycolysis in tumor cell survival and proliferation [36]. Additionally, compelling evidence has now suggested that the Warburg effect is a common trait in many proliferating cells [24,37,38]. This metabolic profile of proliferating cells is fundamentally different from the Pasteur effect, in which cells undergo oxidative phosphorylation (OXPHOS) in the mitochondria to generate ATP for cellular function and maintenance under normoxia but switch to use glycolysis to fulfill the energy requirement under hypoxia, commonly seen in healthy quiescent somatic cells (**Fig. 4**).

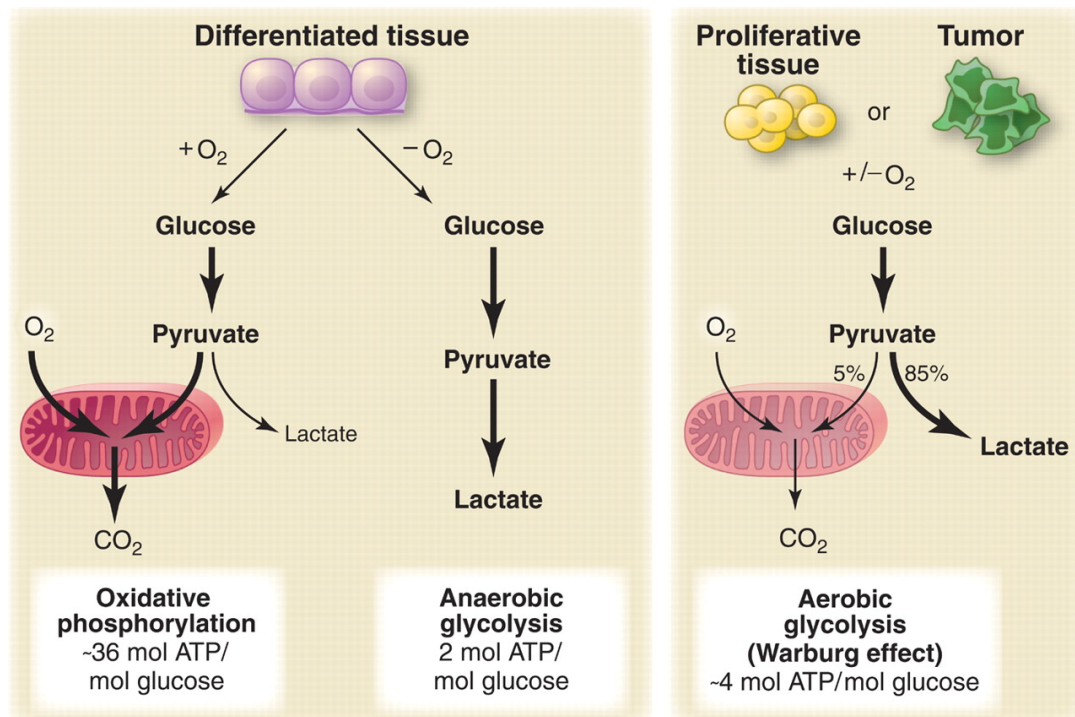


Figure 1-4: Pasteur effect vs. Warburg effect. *Pasteur effect:* In the presence of oxygen, cells convert glucose into pyruvate through glycolysis, shunt pyruvate into the mitochondria to feed the tricarboxylic acid (TCA) cycle and further generate ATP via

OXPPOS. A total of 36 ATPs per glucose consumed is generated in this pathway. In the absence of oxygen (i.e. hypoxia), cells undergo anaerobic fermentation by converting pyruvate into lactate. This process is inefficient in energy production as it results in a total production of 2 ATPs per glucose consumed. (Depicted on the left) *Warburg effect*: With or without the presence of oxygen, proliferating cells undergo aerobic glycolysis by converting glucose to pyruvate and subsequently lactate to produce 4 ATP per glucose consumed. (Depicted on the right) (Adapted from Vander Heiden, Cantley and Thompson, 2009; [36])

This so-called Warburg effect has received renewed interest recently as a potential target for cancer therapy that would be orthogonal to conventional chemotherapies. Yet, despite decades of scrutiny, fundamental questions about the Warburg effect persist. For example, to what extent and in which scenarios does the glycolytic phenotype provide growth and survival advantages to cancer cells? How do cancer cells interact with and manipulate the metabolic behavior of the genetically untransformed cells that are associated with the tumor?

In **Chapter 3**, I will explore how the Warburg effect impacts tumor growth at the population level.

1-5 Reverse Warburg effect

The reverse Warburg effect is a relatively new hypothesis describing the tumor – stromal metabolic dynamics in tumors (**Fig. 5**) [39–41]. In the hypothesis of the reverse Warburg effect, tumor cells uptake lactate in addition to glucose to feed their TCA cycle [42,43]. The lactate in the microenvironment could be the waste product of tumor cells undergoing anaerobic fermentation in the hypoxic regions of tumor, or of the epigenetically rewired stromal cells, possibly due to the modification by tumor cells [44,45]. This kind of cooperative behaviors between the two cell types is referred

as symbiosis from the perspective of population ecology [46–51]. The reverse Warburg effect has been proposed to be a new therapeutic target to treat cancer.

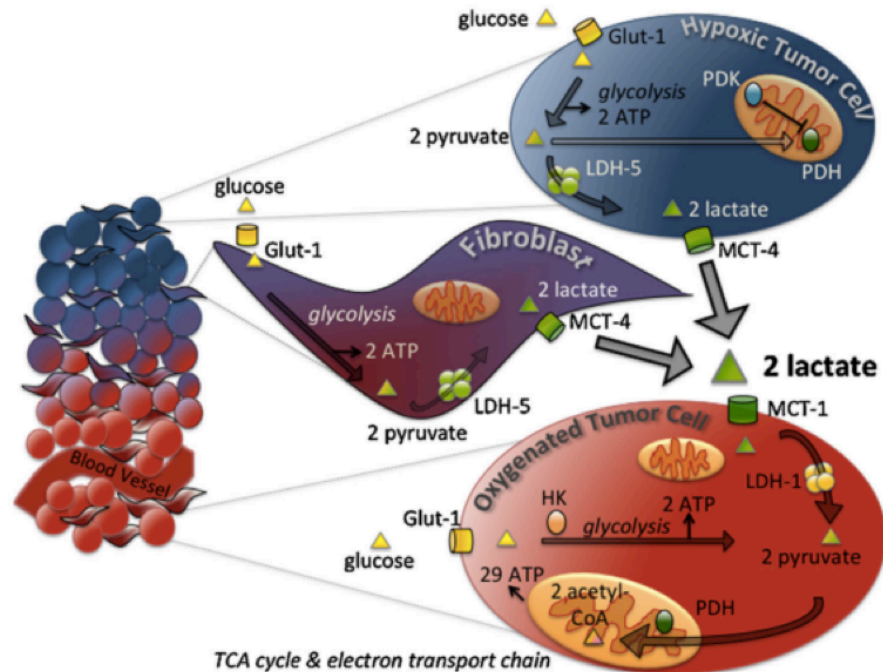
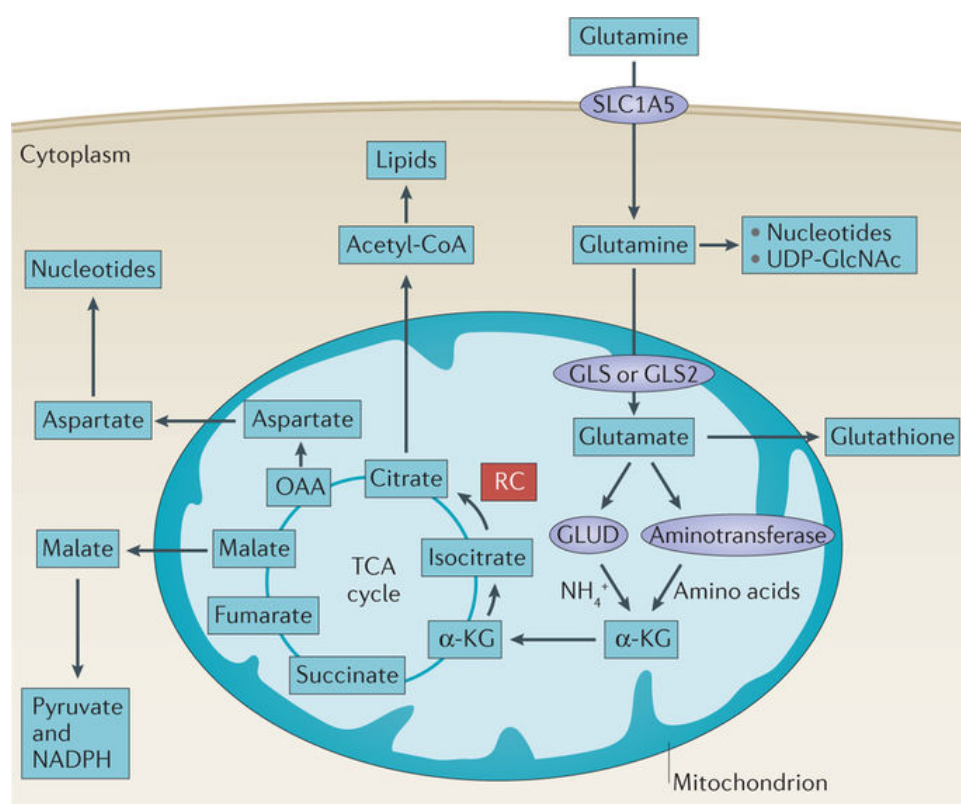


Figure 1-5: Reverse Warburg effect. The three main metabolic phenotypes in the metabolic scenario of reverse Warburg effect: Oxygenated tumor cells (red), hypoxic tumor cells (blue) and “hijacked” stromal cells (cancer-associated fibroblasts, CAFs, purple). The CAFs are epigenetically modified by tumor cells and undergo aerobic glycolysis to produce lactate. Additionally, lactate also comes from the hypoxic tumor cells undergoing anaerobic glycolysis. The oxygenated tumor cells then use the lactate produced by hypoxic tumor cells and the CAFs to fuel their mitochondria for ATP production. (Adapted from Nakajima *et. al*, 2013; [46])

1-6 Glutamine Addiction

Glutamine addiction has emerged as one of the most popular hypotheses in cancer metabolism [52]. Although glutamine addiction is not a common trait across all tumor cells, glutamine as a key substrate for anabolic growth of mammalian cells has started to be recognized as a hallmark of metabolic rewiring in cancer (**Fig. 6**) [52–55]. Specifically, the protein-coding gene *c-Myc* has been found to be crucial in

regulating glutamine uptake in tumor cells. When the tumor cell is Myc-positive, it becomes glutamine-addicted and cannot survive without glutamine [56,57]. Important roles of glutamine in tumor cell survival include supplying carbon and nitrogen for biosynthetic processes, and maintaining redox balance via the production of NADPH and glutathione (**Fig. 6**) [53,55,58]. Although several experimental studies have shown glucose-independent glutamine-dependent cell growth (with different degrees of compromised growth) possibly via gluconeogenesis demonstrating the adaptive characteristic of tumor cells [59–64], the observed heterogeneity in choice of carbon source across different tumor cells is still not well understood.



Nature Reviews | **Cancer**

Figure 1-6: Major fates of glutamine in tumor cells. The use of glutamine in central metabolism of tumor cells is first through the uptake of glutamine via glutamine transporter SLC1A1. Glutamine further contributes to nucleotide biosynthesis and uridine diphosphate N-acetylglucosamine (UDP-GlcNAc) synthesis for support of

protein folding and trafficking in the cytosol. The incorporation of glutamine into the mitochondria is through conversion into glutamate via glutaminases (GLS and GLS2), a process termed glutaminolysis. The glutamine-derived glutamate can further produce glutathione for redox regulation or be converted into alpha-ketoglutarate (α -KG) to feed the TCA cycle. The latter fate of glutamine-derived glutamate is considered the anaplerotic role of glutamine and only regards glutamine as an alternative carbon source to glucose (Adapted from Altman, Stine and Dang, 2016; [65]).

1-7 Tumor hypoxia

Hypoxia is a common characteristic of solid tumors due to a combination of inadequate supply of oxygen (O_2) and high consumption rate by tumor cell metabolism. Tumor hypoxia can be categorized into different types caused by several factors [66,67]:

- Diffusion-limited (chronic) hypoxia is caused by a combination of the structural and functional abnormalities of tumor microvessels and an increase in diffusion distances due to tumor expansion.
- Perfusion-limited (acute) hypoxia is usually a transient state in the tumor tissue and results from inadequate blood flow. Comparing to the hierarchically organized normal vasculature, microvessels in tumor tissues are disorganized, dilated, tortuous and leaky which lead to temporary closure or reduced flow in vessels.
- Anemic hypoxia is caused by reduced oxygen transport capacity of the blood due to tumor-associated or therapy-induced anemia.

Tumor hypoxia impacts tumor progression through mediating the proteomic and genomic changes of cells within the tumor tissues. The short-term impact of hypoxia on cells (malignant and non-malignant) in the tumor tissues is the proteomic

changes. The proteomic changes could be mediated through hypoxia-induced cell cycle arrest, differentiation, apoptosis or necrosis, which lead to tumor growth stasis or impairment [67]. Alternatively, proteomic changes in tumor cells may promote tumor progression through metabolic adaptation, encouragement of tumor cell motility and tumor angiogenesis and so on. Note that reactive oxygen species generated due to hypoxia acts as the intracellular signaling molecule and initiate these proteomic changes in the cells [68].

In addition to the positive impact of proteomic changes on tumor progression is the genomic changes in tumor cells: tumor hypoxia promotes genomic instability, thereby encouraging the genetic heterogeneity in tumor cell populations. At the same time, hypoxia exerts a strong selection pressure on tumor cell population favoring the hypoxia-adapted tumor clones for survival. These clones are not constrained by hypoxia in growth and expand through clonal selection [69]. In turn, the growth of these hypoxia- adapted tumor clones further exacerbates hypoxia, escalating tumor malignancy.

Tumor hypoxia has been an impeding factor in cancer treatments since it can lead to resistance to radiotherapy and chemotherapy. Additionally, tumor hypoxia can impact prognosis and therapeutic outcomes by inducing proteomic and genomic changes in malignant cells [66,70]. However, hypoxia may also provide opportunities for tumor-specific therapeutic strategies. Therefore, understanding how tumor cells respond and adapt to hypoxia for survival and proliferation may lead to novel cancer treatments.

In **Chapter 4**, I will discuss our efforts towards understanding how basal breast cancer cells tune their redox balance to reduce elevated reactive oxygen species (ROS) under prolonged hypoxia for survival and proliferation.

1-8 *References*

- [1] C. Lamagna, M. Aurrand-Lions, B. a Imhof, Dual role of macrophages in tumor growth and angiogenesis., *J. Leukoc. Biol.* 80 (2006) 705–13.
doi:10.1189/jlb.1105656.
- [2] G.E. Davis, A.N. Stratman, A. Sacharidou, W. Koh, Molecular basis for endothelial lumen formation and tubulogenesis during vasculogenesis and angiogenic sprouting., 1st ed., Elsevier Inc., 2011. doi:10.1016/B978-0-12-386041-5.00003-0.
- [3] T. Tammela, G. Zarkada, H. Nurmi, L. Jakobsson, K. Heinolainen, D. Tvorogov, W. Zheng, C.A. Franco, A. Murtoämäki, E. Aranda, N. Miura, S. Ylä-Herttuala, M. Fruttiger, T. Mäkinen, A. Eichmann, J.W. Pollard, H. Gerhardt, K. Alitalo, VEGFR-3 controls tip to stalk conversion at vessel fusion sites by reinforcing Notch signalling., *Nat. Cell Biol.* 13 (2011) 1202–13.
doi:10.1038/ncb2331.
- [4] B.M. Dulmovits, I.M. Herman, Microvascular remodeling and wound healing: a role for pericytes., *Int. J. Biochem. Cell Biol.* 44 (2012) 1800–12.
doi:10.1016/j.biocel.2012.06.031.
- [5] L. Jakobsson, K. Bentley, H. Gerhardt, VEGFRs and Notch: a dynamic collaboration in vascular patterning., *Biochem. Soc. Trans.* 37 (2009) 1233–6.
doi:10.1042/BST0371233.

- [6] H. Gerhardt, M. Golding, M. Fruttiger, C. Ruhrberg, A. Lundkvist, A. Abramsson, M. Jeltsch, C. Mitchell, K. Alitalo, D. Shima, C. Betsholtz, VEGF guides angiogenic sprouting utilizing endothelial tip cell filopodia., *J. Cell Biol.* 161 (2003) 1163–77. doi:10.1083/jcb.200302047.
- [7] A. Eichmann, M. Simons, VEGF signaling inside vascular endothelial cells and beyond., *Curr. Opin. Cell Biol.* 24 (2012) 188–93. doi:10.1016/j.ceb.2012.02.002.
- [8] R. Blanco, H. Gerhardt, VEGF and Notch in tip and stalk cell selection., *Cold Spring Harb. Perspect. Med.* 3 (2013) a006569. doi:10.1101/cshperspect.a006569.
- [9] J.L. Lucitti, E. a V Jones, C. Huang, J. Chen, S.E. Fraser, M.E. Dickinson, Vascular remodeling of the mouse yolk sac requires hemodynamic force., *Development.* 134 (2007) 3317–26. doi:10.1242/dev.02883.
- [10] S. Chien, Mechanotransduction and endothelial cell homeostasis: the wisdom of the cell., *Am. J. Physiol. Heart Circ. Physiol.* 292 (2007) H1209-24. doi:10.1152/ajpheart.01047.2006.
- [11] L. Lamallice, F. Le Boeuf, J. Huot, Endothelial cell migration during angiogenesis., *Circ. Res.* 100 (2007) 782–94. doi:10.1161/01.RES.0000259593.07661.1e.
- [12] P. Carmeliet, Angiogenesis in life, disease and medicine., *Nature.* 438 (2005) 932–6. doi:10.1038/nature04478.
- [13] S. Levenberg, J. Rouwkema, M. Macdonald, E.S. Garfein, D.S. Kohane, D.C. Darland, R. Marini, C.A. van Blitterswijk, R.C. Mulligan, P.A. D’Amore, R.

- Langer, Engineering vascularized skeletal muscle tissue., *Nat. Biotechnol.* 23 (2005) 879–84. doi:10.1038/nbt1109.
- [14] N. Koike, D. Fukumura, O. Gralla, P. Au, J.S. Schechner, R.K. Jain, Tissue engineering: creation of long-lasting blood vessels., *Nature.* 428 (2004) 138–9. doi:10.1038/428138a.
- [15] G. Cheng, S. Liao, H. Kit Wong, D. a Lacorre, E. di Tomaso, P. Au, D. Fukumura, R.K. Jain, L.L. Munn, Engineered blood vessel networks connect to host vasculature via wrapping-and-tapping anastomosis., *Blood.* 118 (2011) 4740–9. doi:10.1182/blood-2011-02-338426.
- [16] J.M. Chan, I.K. Zervantonakis, T. Rimchala, W.J. Polacheck, J. Whisler, R.D. Kamm, Engineering of in vitro 3D capillary beds by self-directed angiogenic sprouting., *PLoS One.* 7 (2012) e50582. doi:10.1371/journal.pone.0050582.
- [17] J.W. Song, D. Bazou, L.L. Munn, Anastomosis of endothelial sprouts forms new vessels in a tissue analogue of angiogenesis., *Integr. Biol. (Camb).* 4 (2012) 857–62. doi:10.1039/c2ib20061a.
- [18] Y. Zheng, J. Chen, M. Craven, N.W. Choi, S. Totorica, A. Diaz-Santana, P. Kermani, B. Hempstead, C. Fischbach-Teschl, J. a López, A.D. Stroock, In vitro microvessels for the study of angiogenesis and thrombosis., *Proc. Natl. Acad. Sci. U. S. A.* 109 (2012) 9342–7. doi:10.1073/pnas.1201240109.
- [19] J.H. Yeon, H.R. Ryu, M. Chung, Q.P. Hu, N.L. Jeon, In vitro formation and characterization of a perfusable three-dimensional tubular capillary network in microfluidic devices., *Lab Chip.* 12 (2012) 2815–22. doi:10.1039/c2lc40131b.
- [20] M.L. Moya, Y.-H. Hsu, A.P. Lee, C.C.W. Hughes, S.C. George, In Vitro

- Perfused Human Capillary Networks., *Tissue Eng. Part C. Methods.* 19 (2013) 730–7. doi:10.1089/ten.TEC.2012.0430.
- [21] L.L.Y. Chiu, M. Montgomery, Y. Liang, H. Liu, M. Radisic, Perfusable branching microvessel bed for vascularization of engineered tissues., *Proc. Natl. Acad. Sci. U. S. A.* 109 (2012) E3414-23. doi:10.1073/pnas.1210580109.
- [22] K.M. Chrobak, D.R. Potter, J. Tien, Formation of perfused, functional microvascular tubes in vitro., *Microvasc. Res.* 71 (2006) 185–96. doi:10.1016/j.mvr.2006.02.005.
- [23] W. Risau, Mechanisms of angiogenesis., *Nature.* 386 (1997) 671–4. doi:10.1038/386671a0.
- [24] D. Verdegem, S. Moens, P. Stapor, P. Carmeliet, Endothelial cell metabolism: parallels and divergences with cancer cell metabolism, *Cancer Metab.* 2 (2014) 19. doi:10.1186/2049-3002-2-19.
- [25] L. Jakobsson, C. a Franco, K. Bentley, R.T. Collins, B. Ponsioen, I.M. Aspalter, I. Rosewell, M. Busse, G. Thurston, A. Medvinsky, S. Schulte-Merker, H. Gerhardt, Endothelial cells dynamically compete for the tip cell position during angiogenic sprouting., *Nat. Cell Biol.* 12 (2010) 943–53. doi:10.1038/ncb2103.
- [26] A.M. Goodwin, P. D’Amore, Vessel maturation and perivascular cells, in: *Tumor Angiogenesis. Basic Mech. Cancer Ther.*, Springer Berlin Heidelberg, Berlin, Heidelberg, 2008: pp. 273–288. doi:10.1007/978-3-540-33177-3_15.
- [27] a. N. Stratman, K.M. Malotte, R.D. Mahan, M.J. Davis, G.E. Davis, Pericyte recruitment during vasculogenic tube assembly stimulates endothelial basement membrane matrix formation, *Blood.* 114 (2009) 5091–5101. doi:10.1182/blood-

2009-05-222364.

- [28] B. Jiang, E. M., Formation of Stable Vascular Networks in Engineered Tissues, in: Regen. Med. Tissue Eng. - Cells Biomater., InTech, 2011.
doi:10.5772/23223.
- [29] J. Ferlay, I. Soerjomataram, M. Ervik, R. Dikshit, S. Eser, C. Mathers, M. Rebelo, D.M.M. Parkin, D. Forman, F. Bray, GLOBOCAN 2012 v1.0, Cancer Incidence and Mortality Worldwide, IARC CancerBase No. 11 [Internet]. 11 (2013) <http://globocan.iarc.f>. doi:10.1016/j.ucl.2013.01.011.
- [30] D.M. Gilkes, G.L. Semenza, D. Wirtz, Hypoxia and the extracellular matrix: Drivers of tumour metastasis, *Nat. Rev. Cancer.* 14 (2014) 430–439.
doi:10.1038/nrc3726.
- [31] T.L. Whiteside, The tumor microenvironment and its role in promoting tumor growth, *Oncogene.* 27 (2008) 5904–5912. doi:10.1038/onc.2008.271.
- [32] M. Egeblad, E.S. Nakasone, Z. Werb, Tumors as organs: Complex tissues that interface with the entire organism, *Dev. Cell.* 18 (2010) 884–901.
doi:10.1016/j.devcel.2010.05.012.
- [33] K.L. Eales, K.E.R. Hollinshead, D.A. Tennant, Hypoxia and metabolic adaptation of cancer cells, *Oncogenesis.* 5 (2016) e190.
doi:10.1038/oncsis.2015.50.
- [34] B.Y.O. Warburg, F. Wind, *The Metabolism of Tumors in the Body*, (1927).
- [35] O. Warburg, *On the Origin of Cancer Cells* (Science 1956).pdf, 123 (1956).
- [36] M.G. Vander Heiden, L.C. Cantley, C.B. Thompson, Understanding the Warburg effect: the metabolic requirements of cell proliferation., *Science.* 324

- (2009) 1029–1033. doi:10.1126/science.1160809.
- [37] F. Polet, O. Feron, Endothelial cell metabolism and tumour angiogenesis: Glucose and glutamine as essential fuels and lactate as the driving force, *J. Intern. Med.* 273 (2013) 156–165. doi:10.1111/joim.12016.
- [38] K. Renner, K. Singer, G.E. Koehl, E.K. Geissler, K. Peter, P.J. Siska, M. Kreutz, Metabolic hallmarks of tumor and immune cells in the tumor microenvironment, *Front. Immunol.* 8 (2017) 248. doi:10.3389/fimmu.2017.00248.
- [39] N. Draoui, O. Feron, Lactate shuttles at a glance: from physiological paradigms to anti-cancer treatments, *Dis. Model. Mech.* 4 (2011) 727–732. doi:10.1242/dmm.007724.
- [40] C.T. Hensley, B. Faubert, Q. Yuan, N. Lev-Cohain, E. Jin, J. Kim, L. Jiang, B. Ko, R. Skelton, L. Loudat, M. Wozzak, C. Klimko, E. McMillan, Y. Butt, M. Ni, D. Oliver, J. Torrealba, C.R. Malloy, K. Kernstine, R.E. Lenkinski, R.J. DeBerardinis, Metabolic Heterogeneity in Human Lung Tumors, *Cell.* 164 (2016) 681–694. doi:10.1016/j.cell.2015.12.034.
- [41] P. Sonveaux, F. Végran, T. Schroeder, M.C. Wergin, J. Verrax, Z.N. Rabbani, C.J. De Saedeleer, K.M. Kennedy, C. Diepart, B.F. Jordan, M.J. Kelley, B. Gallez, M.L. Wahl, O. Feron, M.W. Dewhirst, Targeting lactate-fueled respiration selectively kills hypoxic tumor cells in mice, *J. Clin. Invest.* 118 (2008) 3930–3942. doi:10.1172/JCI36843.
- [42] S. Hui, J.M. Ghergurovich, R.J. Morscher, C. Jang, X. Teng, W. Lu, L.A. Esparza, T. Reya, L. Zhan, J. Yanxiang Guo, E. White, J.D. Rabinowitz,

Glucose feeds the TCA cycle via circulating lactate, *Nature*. 551 (2017) 115–118. doi:10.1038/nature24057.

- [43] B. Faubert, K.Y. Li, L. Cai, J.D. Young, K. Kernstine, R.J. Deberardinis Correspondence, C.T. Hensley, J. Kim, L.G. Zacharias, C. Yang, Q.N. Do, S. Doucette, D. Burguete, H. Li, G. Huet, Q. Yuan, T. Wigal, Y. Butt, M. Ni, J. Torrealba, D. Oliver, R.E. Lenkinski, C.R. Malloy, J.W. Wachsmann, R.J. Deberardinis, Lactate Metabolism in Human Lung Tumors Human non-small cell lung cancer preferentially utilizes lactate over glucose to fuel TCA cycle and sustain tumor metabolism in vivo. *Lactate Metabolism in Human Lung Tumors*, *Cell*. 171 (2017) 358–367.e9. doi:10.1016/j.cell.2017.09.019.
- [44] G. Bonuccelli, D. Whitaker-Menezes, R. Castello-Cros, S. Pavlides, R.G. Pestell, A. Fatatis, A.K. Witkiewicz, M.G. Vander Heiden, G. Migneco, B. Chiavarina, P.G. Frank, F. Capozza, N. Flomenberg, U.E. Martinez-Outschoorn, F. Sotgia, M.P. Lisanti, The reverse Warburg effect: Glycolysis inhibitors prevent the tumor promoting effects of caveolin-1 deficient cancer associated fibroblasts, *Cell Cycle*. 9 (2010) 1960–1971. doi:10.4161/cc.9.10.11601.
- [45] S. Pavlides, D. Whitaker-Menezes, R. Castello-Cros, N. Flomenberg, A.K. Witkiewicz, P.G. Frank, M.C. Casimiro, C. Wang, P. Fortina, S. Addya, R.G. Pestell, U.E. Martinez-Outschoorn, F. Sotgia, M.P. Lisanti, The reverse Warburg effect: Aerobic glycolysis in cancer associated fibroblasts and the tumor stroma, *Cell Cycle*. 8 (2009) 3984–4001. doi:10.4161/cc.8.23.10238.
- [46] E.C. Nakajima, B. Van Houten, Metabolic symbiosis in cancer: Refocusing the

- Warburg lens, *Mol. Carcinog.* 52 (2013) 329–337. doi:10.1002/mc.21863.
- [47] E. Obre, R. Rossignol, Emerging concepts in bioenergetics and cancer research: Metabolic flexibility, coupling, symbiosis, switch, oxidative tumors, metabolic remodeling, signaling and bioenergetic therapy, *Int. J. Biochem. Cell Biol.* 59 (2015) 167–181. doi:10.1016/j.biocel.2014.12.008.
- [48] C. Phipps, H. Molavian, M. Kohandel, A microscale mathematical model for metabolic symbiosis : Investigating the effects of metabolic inhibition on ATP turnover in tumors, *J. Theor. Biol.* 366 (2015) 103–114. doi:10.1016/j.jtbi.2014.11.016.
- [49] O. Feron, Pyruvate into lactate and back: From the Warburg effect to symbiotic energy fuel exchange in cancer cells, *Radiother. Oncol.* 92 (2009) 329–333. doi:10.1016/j.radonc.2009.06.025.
- [50] J.B. McGillen, C.J. Kelly, A. Martínez-González, N.K. Martin, E. a Gaffney, P.K. Maini, V.M. Pérez-García, Glucose-lactate metabolic cooperation in cancer: insights from a spatial mathematical model and implications for targeted therapy., *J. Theor. Biol.* 361 (2014) 190–203. doi:10.1016/j.jtbi.2014.09.018.
- [51] B. Mendoza-Juez, A. Martínez-González, G.F. Calvo, V.M. Pérez-García, A Mathematical Model for the Glucose-Lactate Metabolism of in Vitro Cancer Cells, *Bull. Math. Biol.* 74 (2012) 1125–1142. doi:10.1007/s11538-011-9711-z.
- [52] N.N. Pavlova, C.B. Thompson, The Emerging Hallmarks of Cancer Metabolism, *Cell Metab.* 23 (2016) 27–47. doi:10.1016/j.cmet.2015.12.006.
- [53] D.R. Wise, C.B. Thompson, Glutamine addiction: a new therapeutic target in

- cancer, *Trends Biochem. Sci.* 35 (2010) 427–433.
doi:10.1016/j.tibs.2010.05.003.
- [54] L. Alberghina, D. Gaglio, Redox control of glutamine utilization in cancer, *Cell Death Dis.* 5 (2014) e1561. doi:10.1038/cddis.2014.513.
- [55] D. Daye, K.E. Wellen, Metabolic reprogramming in cancer: Unraveling the role of glutamine in tumorigenesis, *Semin. Cell Dev. Biol.* 23 (2012) 362–369.
doi:10.1016/j.semcdb.2012.02.002.
- [56] D.R. Wise, R.J. DeBerardinis, A. Mancuso, N. Sayed, X.-Y. Zhang, H.K. Pfeiffer, I. Nissim, E. Daikhin, M. Yudkoff, S.B. McMahon, C.B. Thompson, Myc regulates a transcriptional program that stimulates mitochondrial glutaminolysis and leads to glutamine addiction., *Proc. Natl. Acad. Sci. U. S. A.* 105 (2008) 18782–18787. doi:10.1073/pnas.0810199105.
- [57] M. Yuneva, N. Zamboni, P. Oefner, R. Sachidanandam, Y. Lazebnik, Deficiency in glutamine but not glucose induces MYC-dependent apoptosis in human cells, *J. Cell Biol.* 178 (2007) 93–105. doi:10.1083/jcb.200703099.
- [58] R. Moreno-Sánchez, S. Rodríguez-Enríquez, A. Marín-Hernández, E. Saavedra, Energy metabolism in tumor cells, *FEBS J.* 274 (2007) 1393–1418.
doi:10.1111/j.1742-4658.2007.05686.x.
- [59] E.D. Montal, R. Dewi, K. Bhalla, L. Ou, B.J. Hwang, A.E. Ropell, C. Gordon, W.J. Liu, R.J. DeBerardinis, J. Sudderth, W. Twaddel, L.G. Boros, K.R. Shroyer, S. Duraisamy, R. Drapkin, R.S. Powers, J.M. Rohde, M.B. Boxer, K.K. Wong, G.D. Girnun, PEPCK Coordinates the Regulation of Central Carbon Metabolism to Promote Cancer Cell Growth, *Mol. Cell.* 60 (2015) 571–

583. doi:10.1016/j.molcel.2015.09.025.

- [60] E. Balsa-Martinez, P. Puigserver, Cancer Cells Hijack Gluconeogenic Enzymes to Fuel Cell Growth, *Mol. Cell.* 60 (2015) 509–511.
doi:10.1016/j.molcel.2015.11.005.
- [61] K. Leithner, A. Hrzenjak, M. Trötzmüller, T. Moustafa, H.C. Köfeler, C. Wohlkoenig, E. Stacher, J. Lindenmann, L. Harris, A. Olschewski, H. Olschewski, PCK2 activation mediates an adaptive response to glucose depletion in lung cancer, *Oncogene.* 34 (2015) 1044–1050.
doi:10.1038/onc.2014.47.
- [62] J. Chen, H.-J. Lee, X. Wu, L. Huo, S.-J. Kim, L. Xu, Y. Wang, J. He, L.R. Bollu, G. Gao, F. Su, J. Briggs, X. Liu, T. Melman, J. Asara, I.J. Fidler, L.C. Cantley, J.W. Locasale, Z. Weihua, Gain of glucose-independent growth upon metastasis of breast cancer cells to the brain., *Cancer Res.* 75 (2015) 554–565.
doi:10.1158/0008-5472.CAN-14-2268.
- [63] E.E. Vincent, A. Sergushichev, T. Griss, M.C. Gingras, B. Samborska, T. Ntimbane, P.P. Coelho, J. Blagih, T.C. Raissi, L. Choinière, G. Bridon, E. Loginicheva, B.R. Flynn, E.C. Thomas, J.M. Tavaré, D. Avizonis, A. Pause, D.J.E. Elder, M.N. Artyomov, R.G. Jones, Mitochondrial Phosphoenolpyruvate Carboxykinase Regulates Metabolic Adaptation and Enables Glucose-Independent Tumor Growth, *Mol. Cell.* 60 (2015) 195–207.
doi:10.1016/j.molcel.2015.08.013.
- [64] A. Le, A.N.N. Lane, M. Hamaker, S. Bose, A. Gouw, J. Barbi, T. Tsukamoto, C.J.J. Rojas, B.S.S. Slusher, H. Zhang, L.J.J. Zimmerman, D.C.C. Liebler,

- R.J.C.J.C. Slebos, P.K.K. Lorkiewicz, R.M.M. Higashi, T.W.M.W.M. Fan, C.V. V. Dang, Glucose-independent glutamine metabolism via TCA cycling for proliferation and survival in b cells, *Cell Metab.* 15 (2012) 110–121.
doi:10.1016/j.cmet.2011.12.009.
- [65] B.J. Altman, Z.E. Stine, C. V. Dang, From Krebs to clinic: glutamine metabolism to cancer therapy, *Nat. Rev. Cancer.* 16 (2016) 619–634.
doi:10.1038/nrc.2016.71.
- [66] J.M. Brown, W.R. Wilson, Exploiting tumour hypoxia in cancer treatment., *Nat. Rev. Cancer.* 4 (2004) 437–47. doi:10.1038/nrc1367.
- [67] P. Vaupel, Tumor Hypoxia: Causative Factors, Compensatory Mechanisms, and Cellular Response, *Oncologist.* 9 (2004) 4–9. doi:10.1634/theoncologist.9-90005-4.
- [68] M. Tafani, L. Sansone, F. Limana, T. Arcangeli, E. De Santis, M. Polese, M. Fini, M.A. Russo, The Interplay of Reactive Oxygen Species, Hypoxia, Inflammation, and Sirtuins in Cancer Initiation and Progression, *Oxid. Med. Cell. Longev.* 2016 (2016) 1–18. doi:10.1155/2016/3907147.
- [69] M. Hockel, P. Vaupel, Tumor Hypoxia: Definitions and Current Clinical, Biologic, and Molecular Aspects, *JNCI J. Natl. Cancer Inst.* 93 (2001) 266–276.
doi:10.1093/jnci/93.4.266.
- [70] J.M. Brown, Tumor Hypoxia in Cancer Therapy, *Methods Enzymol.* 435 (2007) 295–321. doi:10.1016/S0076-6879(07)35015-5.

CHAPTER 2

ENDOTHELIAL CELL DYNAMICS DURING ANASTOMOSIS IN VITRO

This chapter is adapted from a published work:

A. Diaz-Santana*, M. Shan*, A.D. Stroock. Endothelial cell dynamics during anastomosis *in vitro*. *Integr. Biol.* 2015, **7**(4):454–66.

*These authors contributed equally to this work.

2-1 Introduction

Vasculature is indispensable in higher organisms as it transports metabolites, waste products, and immune cells to sustain and protect tissues. In adults, angiogenesis – the sprouting of new vessels from pre-existing vasculature – occurs in response to physiological stimuli during, for example wound healing and the menstrual cycle [1,2]. However, an imbalance in the stimulating and inhibiting cues for vessel growth can lead to pathological angiogenesis, implicated in a variety of diseases such as cancer and diabetic retinopathy [3].

Currently, a broad variety of models both *in vivo* and *in vitro* are being used to study angiogenesis[4]. In the past three decades, studies have begun to elucidate the major molecular [5] and cellular players [6], signaling pathways [7], as well as cellular dynamics [8–11] involved in angiogenesis. As our understanding of angiogenesis

develops, it has become a target for a variety of therapeutic strategies, with both pro-angiogenic and anti-angiogenic drugs in the clinic and under development [2,12,13].

In the context of regenerative medicine, the possibility of growing living tissues *in vitro* followed by implantation holds promise as a route to repair damaged tissues and correct congenital defects. Clinical successes of this tissue engineering strategy include: skin section replacements [14], bladder replacements [15], and large scale arterial or venous grafts in cardiovascular diseases [16]. Generalizing this approach to larger tissue constructs and full organs [17] poses significant, outstanding challenges which include 1) appropriate physiology on both macroscopic and microscopic scales (e.g. suitable sources of cell and biomaterials); 2) proper maintenance during *in vitro* culture; and 3) compatibility with surgical implantation (e.g. surgical connections from engineered tissue to host). In many contexts, the induction of vascularization of scaffolds represents a particular challenge in tissue engineering as the oxygen depletion length (the distance over which oxygen can diffuse before being consumed, known as the Krogh length [18,19]) requires that capillary vessels in living tissues be within 50-100 μm of one another. *In vivo*, vascularization occurs via two processes: vasculogenesis, the spontaneous formation of capillaries from individual endothelial cells (ECs) and sprouting angiogenesis, the emergence of new vessels from pre-existing ones [20]. Both of these steps require anastomosis, the fusion of vessels segments to eliminate dead-ends and allow for blood circulation. The growth of clinically relevant tissues *in vitro* similarly requires the formation of blood vessels and their anastomosis in order to provide closed blood circulation on all scales, from the surgically accessible dimension (1-2 mm) [21] and down to capillary dimension.

Tackling this challenge could be enabled by the appropriate induction of anastomosis. Distinct approaches have shown the occurrence of anastomosis between two angiogenic sprouting events and perfusion at capillary scale [22–26]. These approaches based on confining micro-scale tissue constructs within microfluidic devices allow tight control of capillary-scale growth processes. However, they are incompatible with engineering of large-scale tissues due to the limited volume of the tissue. These preliminary successes point to the need to understand the dynamics of anastomosis in more detail and for a readily available tool with which anastomosis can be generated in large volumes of tissue. These specific challenges motivated our effort to develop a simple assay to study anastomosis based on parallel action of sprouting angiogenesis and vasculogenesis.

In this study, we exploit a 3-D culture platform [27,28] to focus on the cellular dynamics during and post anastomosis (**Fig. 2-1**). Our system is comprised of an endothelium seeded on top of matrix of type I collagen of well-defined dimensions and seeded with cells. This design represents a simple mimic of the architecture of the endothelium of a mature vessel adjacent to a cellularized tissue. Our base case was a homotypic co-culture, with endothelial cells (Human Umbilical Vein Endothelial Cells, HUVECs) initially in two distinct sub-populations: on the surface of the collagen and in the bulk collagen. To enable the identification and tracking of these two populations (spatial distribution of cell populations, “population tracking”) we labeled them prior to culture: RFP⁺-HUVECs in the monolayer and GFP⁺-HUVECs in the bulk collagen. We also generated heterotypic co-cultures with the incorporation of perivascular cells (Human Brain Perivascular Cells, HBPVCs) in the bulk collagen (blue cells in **Fig. 2-1A**).

In the presence of pro-angiogenic media, this platform allows for sprouting angiogenesis from the endothelium and vasculogenesis in the bulk collagen (**Fig. 2-1B**). Across the conditions shown in **Figure 2-2**, we performed immunohistological and fluorescence confocal microscopy; analyzed these images to extract qualitative information about the structure and quantitative information on distributions of individual sub-populations (those originating at monolayer and those originating in bulk); and captured live 3-D images of homotypic co-culture to clarify cell-scale dynamics of migration on pre-existing vessels in bulk.

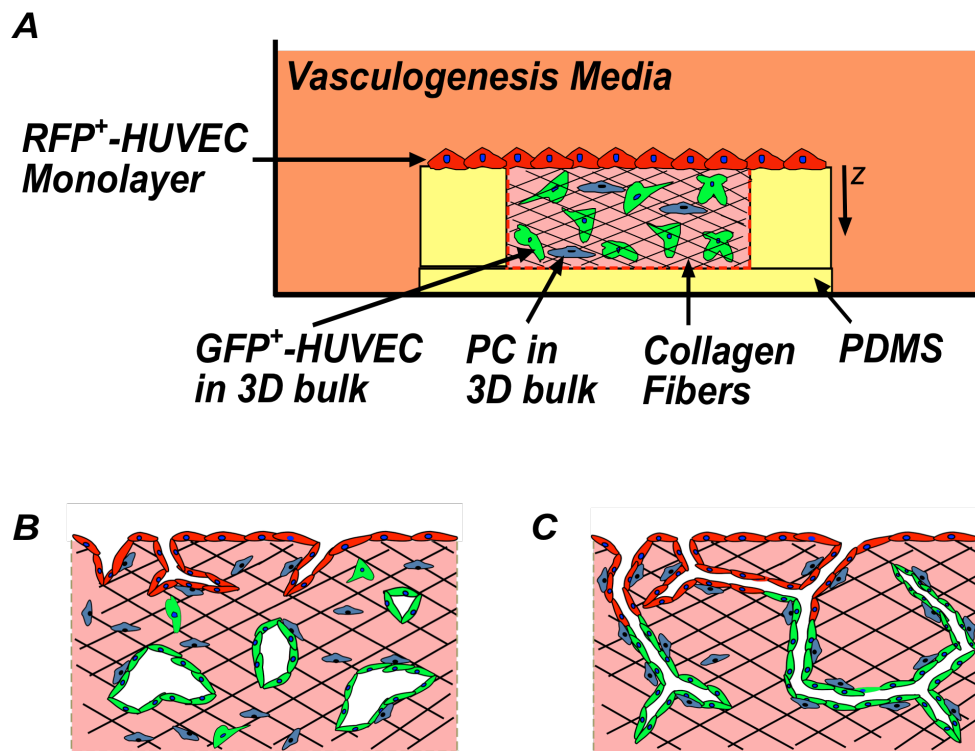


Figure 2-1: Schematic diagrams of anastomosis in homotypic co-culture of endothelial cells. RFP⁺-HUVECs (red) form a quiescent endothelium. GFP⁺-HUVECs (green) and pericytes (blue) in 3-D matrix of collagen (pink). Fibers formed within the collagen (black). (A) Overall experimental set-up, side-view. (B) Sprouting angiogenesis occurs from the endothelium (RFP⁺-HUVECs) in the presence of pro-angiogenic growth factors. GFP⁺-HUVECs undergo vasculogenesis. (C) Hypothesis: Anastomosis occurs

between sprouting angiogenesis and vasculogenesis. Pericytes are recruited to cover the nascent endothelial cell tubules to provide stability.

We exploited this platform to test the hypotheses that 1) vascular anastomosis would occur between sprouts formed from the endothelium and tubes formed by vasculogenesis (**Fig. 2-1C**); and **2-2**) this process would depend on the density of cells in the bulk and presence of pericytes. We further exploited the ability to perform population tracking in order to investigate the dynamics of cell migration during anastomosis.

2-2 Results and Discussion

2-2-1 Culture configurations

Figure 2 presents the specific configurations used in this study: 1) Mono Only (**Fig. 2-2A**) – this configuration represents a confluent monolayer that mimics an endothelium from which angiogenesis will occur upon; 2) Bulk Only (**Fig. 2-2B-C**) – this configuration resembles the process of vasculogenesis where ECs self-assemble to form lumenized tubes; 3) Mono + Bulk (**Fig. 2-2D-F**) – this configuration allows us to assess the interactions of the two process – angiogenic sprouting from an endothelium and vasculogenesis in the bulk collagen – occurring in parallel; 4) Mono + Bulk + Pericytes (**Fig. 2-2G**) – this configuration incorporates PCs in the system, which serves as a comparison to Mono + Bulk as well as providing insights in the effects of PCs on vessel maturation.

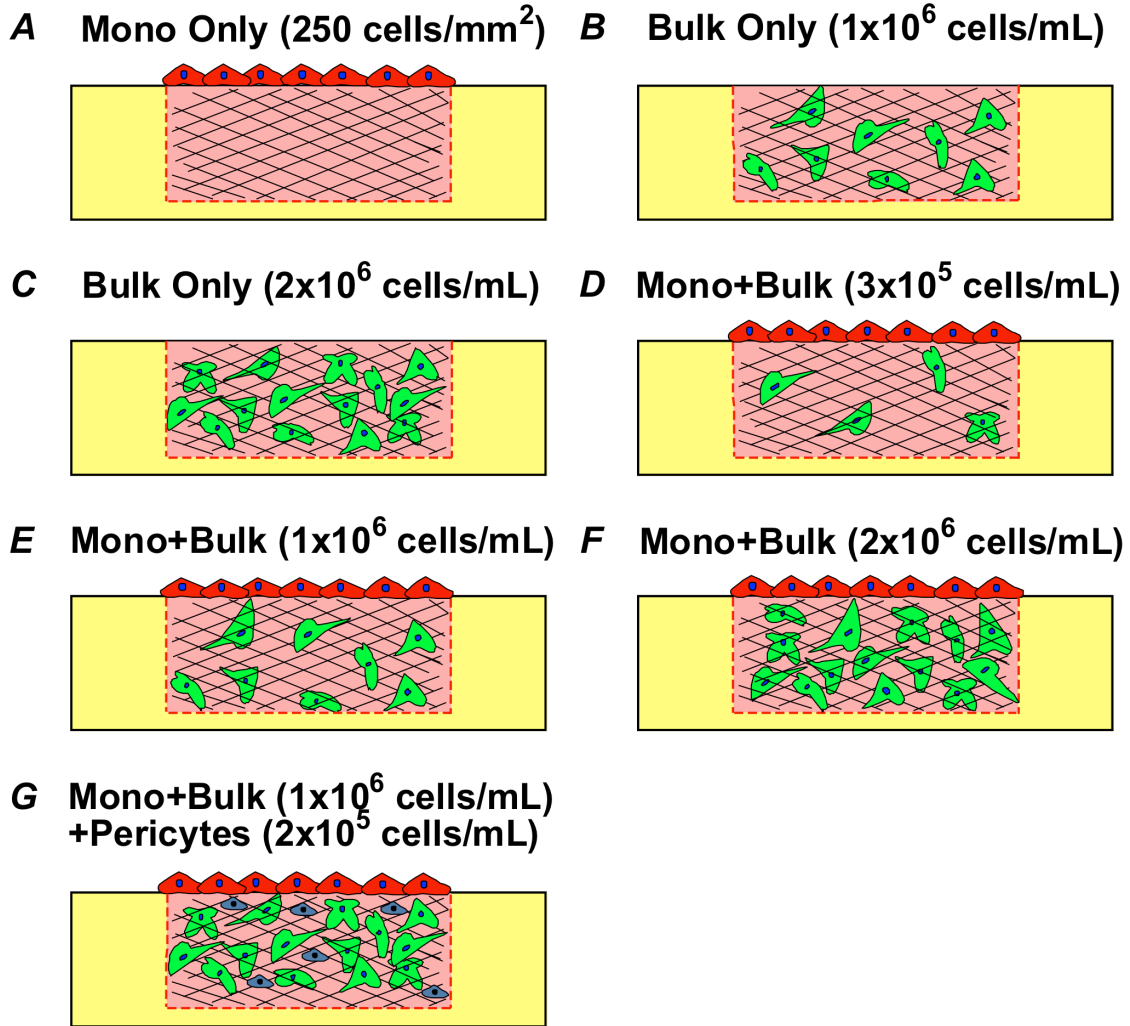


Figure 2-2: Schematic diagrams of experimental configurations and conditions. (A) Monolayer (Mono) only. (B-C) Bulk only, with bulk density of 1×10^6 cells/mL (B) and 2×10^6 cells/mL (C). (D-F) Mono + Bulk, with bulk density of 3×10^5 cells/mL (D), 1×10^6 cells/mL (E), and 2×10^6 cells/mL (F). (G) Mono + Bulk + Pericytes, with bulk density of 1×10^6 cells/mL and PCs density of 2×10^5 cells/mL.

2-2-2 Independent angiogenesis and vasculogenesis

We first examined angiogenesis and vasculogenesis individually in this platform. These mono-cultures represent controls for the behaviors we observe in the homotypic co-culture. Previous studies have used this format to study angiogenesis and

vasculogenesis, and showed that these two processes can be recapitulated with this specific geometry using a pro-angiogenic media containing vascular endothelial growth factor (VEGF), basic fibroblast growth factor (bFGF) and phorbol-12-myristate-13-acetate (PMA) [27–29].

In the angiogenesis model, multi-cellular, lumenized sprouts emerged from the planar configuration of monolayer cells (MCs) into the bulk collagen (**Fig. 2-3A**) by Day 7. The horizontal (xy) cross-section of the matrix acquired by confocal fluorescence microscopy in **Figure 2-3A** shows that the angiogenic sprouts led by single cells are continuous extensions from the monolayer and the vascular structures are present at all depths up to 45 μm ; the greatest depths at which we observed sprouts in this configuration was $\sim 100 \mu\text{m}$. In the vasculogenesis model, with bulk cells (BCs) density of 1×10^6 cells/mL (hereafter referred as “medium”), the cells formed a minimum of vacuoles but did not undergo tubulogenesis (formation of multicellular, lumenized structures) in the bulk collagen by Day 7 (**Fig. 2-3B, Fig. 2-3C**); more extensive vacuoles formed at greater depths (**Fig. 2-3C**). At a density of BCs of 2×10^6 cells/mL (hereafter referred as “high”), the cells formed more, larger vacuoles at small depths (data not shown) and underwent tubulogenesis at greater depths (**Fig. 2-3D**). No extended tubes were observed at Day 7. This density-dependence of the vasculogenesis agrees with our previous work [27] with this platform and points to bulk density of ECs as an important parameter in tuning the properties of the homotypic co-culture.

2-2-3 *Anastomosis between the sub-populations of cells*

In vivo, angiogenic sprouts from an endothelium, invade into the bulk tissue, and eventually anastomose with a pre-existing vascular network [20,30]. However, we are unaware of observation of anastomosis between angiogenic sprouts and tubes formed by vasculogenesis, *in vitro*. The recapitulation of this process *in vitro* could provide a basis for rapidly forming connections between engineered microvessels (e.g., [Zheng et al., 2012]) and pervasive capillary structure in engineered tissues. In order to model anastomosis between these two processes, we used a configuration where RFP⁺-HUVECs were seeded on collagen as MCs (250 cells/mm²) to generate angiogenic invasions, and GFP⁺-HUVECs were seeded as BCs at medium (1×10⁶ cells/mL) density to undergo vasculogenesis, simultaneously (**Fig. 2-2E**).

Figure 2-4A presents fluorescent micrographs that show the qualitative features observed for the medium density of GFP⁺-HUVECs in the bulk after Day 7 of homotypic co-culture. We observe that BCs migrated upwards and became part of the monolayer (green cells present in monolayer at $z = 0 \mu\text{m}$). Further, lumenized sprouts formed of MCs emerged from the surface ($z = 0 \mu\text{m}$) and propagated into the bulk (labeled with asterisks at $z = 15$ and $30 \mu\text{m}$). Lumenized structures in the bulk were formed of BCs (arrow at $z = 45 \mu\text{m}$). Additionally, an abundance of lumenized, multicellular structures formed of both monolayer and bulk cells were observed throughout the captured depth (labeled with arrow heads at $z = 15, 30,$ and $45 \mu\text{m}$).

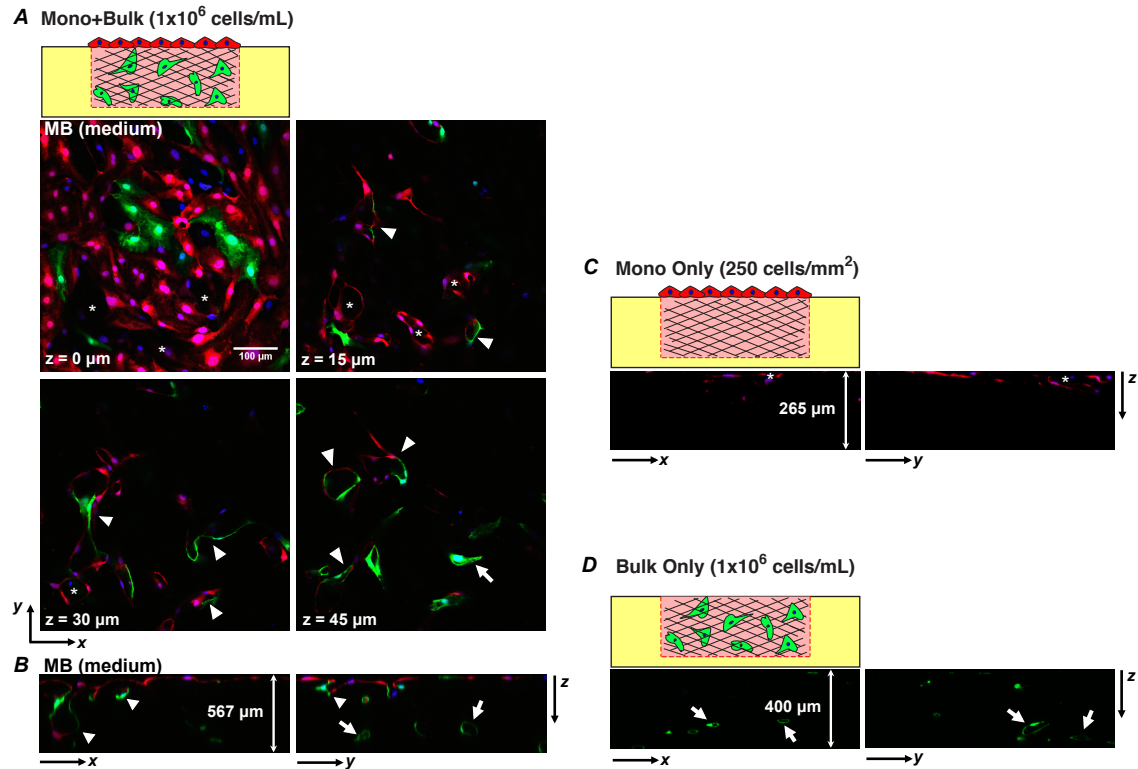


Figure 2-4: Fluorescence confocal sections of various configurations after 7 days of culture. (A) Horizontal cross-sections at $z = 0, 15, 30$ and $45 \mu\text{m}$ of the configuration of Mono + Bulk with 1×10^6 cells/mL in bulk, “MB (medium)”. (B-D) Vertical cross-sections showing zx - and zy -sections from MB (medium) culture in frame (A) (B –depth of the z -stack is $\sim 567 \mu\text{m}$), from MO culture (C –depth of the z -stack is $\sim 265 \mu\text{m}$), and from BO (medium) culture (D –depth of the z -stack is $\sim 400 \mu\text{m}$). Asterisk: Angiogenic invasion from monolayer with lumen structures. Arrow: Lumen structures formed by *de novo* vasculogenesis. Arrowhead: lumenized structures formed by anastomosis of cells from monolayer (red) and bulk (green).

Looking more closely in **Figure 2-4B**, we observe that MCs were present as deep as $\sim 400 \mu\text{m}$ (red signals in the bulk collagen at a greater depth) as part of a lumen structure whereas no MCs traveled further greater than $\sim 100 \mu\text{m}$ in the configuration of “Mono Only” (**Fig. 2-4C**). This comparison suggests that BCs or the tubes structures formed by BCs facilitated the migration of MCs. Notably, the intermixed lumen

structures were significantly larger than the angiogenic sprouts formed by pure angiogenesis in **Figure 2-3A**. Furthermore, **Figure 2-4A** and **Figure 2-4B** show that several multi-cellular lumen structures appeared at all depths, in contrast to the angiogenic sprouts led by single cells in **Figure 2-3A**. The observation that lumen structures were enlarged and became multi-cellular suggests that angiogenesis was enhanced by the presence of BCs. Compared to the vasculogenesis experiments (**Fig. 2-3B**, **Fig. 2-4D**), lumen structures formed in the bulk closer to the top surface of the gel via vasculogenesis (**Fig. 2-4A**, white arrow at $z = 45 \mu\text{m}$) whereas cells did not undergo tubulogenesis at this depth in the configuration of Bulk Only (“medium”, **Fig. 2-3B**). This observation indicates that the presence of MCs promoted vasculogenesis by BCs with a medium density. Importantly, the observations that 1) lumenized angiogenic sprouts extended into the bulk as continuous lumen structures, 2) BCs underwent vasculogenesis in the bulk collagen and 3) the mixed composition of cells suggest that anastomosis occurred between sprouting angiogenesis originated from the monolayer and open-lumen vascular structures in the bulk formed by vasculogenesis.

In contrast to our hypothetical mode of interaction between MCs and BCs (**Fig. 2-1C**), the lumenized invasions presented a locally mixed composition with respect to the sub-populations of cells: At the monolayer, invasions were predominately composed of RFP⁺-HUVECs (MCs) (**Fig. 2-4A**, $z = 15 \mu\text{m}$, star and arrowheads); in the bulk, tubes were formed of purely of GFP⁺-HUVECs (BCs) (**Fig. 2-4A**, $z = 45 \mu\text{m}$, arrow) and of mixture of MCs and BCs (arrowheads in **Fig. 2-4A**, **Fig. 2-4B**). Comparison with Mono Only (**Fig. 2-4C**) or Bulk Only (medium, **Fig. 2-4D**) suggests that the larger vessel structures were not simply the result of extensive vasculogenesis or pure anastomosis.

We will return to a further consideration of the process that led to this intermixing after a global quantification of the degree of migration as a function of culture conditions.

2-2-4 Migration of monolayer cells into the bulk

We sought to understand how the inclusion of ECs in the bulk influenced the process of cellular invasions during sprouting angiogenesis. To characterize the distribution of red and green cells in a stack, we calculated the total intensity of red (for RFP⁺-HUVECs) and green (for GFP⁺-HUVECs) in each image within the stack; we normalized the intensities of an image with respect to the total intensity of the stack (see **Section 2.3**). To characterize the progression of cells as they migrated, we quantified standard configurations (Mono + Bulk, medium) with end-points of 1, 3, 5, and 7 days. **Figures 2-5A** and **2-5B** present this normalized intensity as a function of depth into the matrix for RFP⁺-HUVECs (originating from the endothelium) and GFP⁺-HUVECs (originating from the bulk) respectively. At Day 1 of culture (**Fig. 2-5A**, black), the presence of MCs at the monolayer interface ($z = 0 \mu\text{m}$) was found to be the highest compared to 3, 5 and 7 days (**Fig. 2-5A**, red, blue and grey, respectively). This trend suggests that MCs progressively left the monolayer (lowering of red signal at $z = 0 \mu\text{m}$) and penetrated further into the collagen at later days. Conversely, for the cells originally seeded in the bulk collagen, the intensity at the surface ($z = 0 \mu\text{m}$) rose toward the surface with time (**Fig. 2-5B**). We associate this increase in intensity with the incorporation of BCs into the monolayer, as is seen in **Figure 2-4A**. Beyond a depth of $25 \mu\text{m}$, the distributions of BCs remained similar at different end-points of culture time (**Fig. 2-5B**). We note that an alternative explanation for the variation in normalized intensities could be due to cell proliferation or apoptosis in a spatially dependent manner. However, we

favor the interpretation of cell migration because of the noted correlation with qualitative images and lack of evidence of apoptosis and mitosis during the culture period. We note that there is a small loss of cellularity up to 25% and we propose that this may be due to migration of cells out of the field of view.

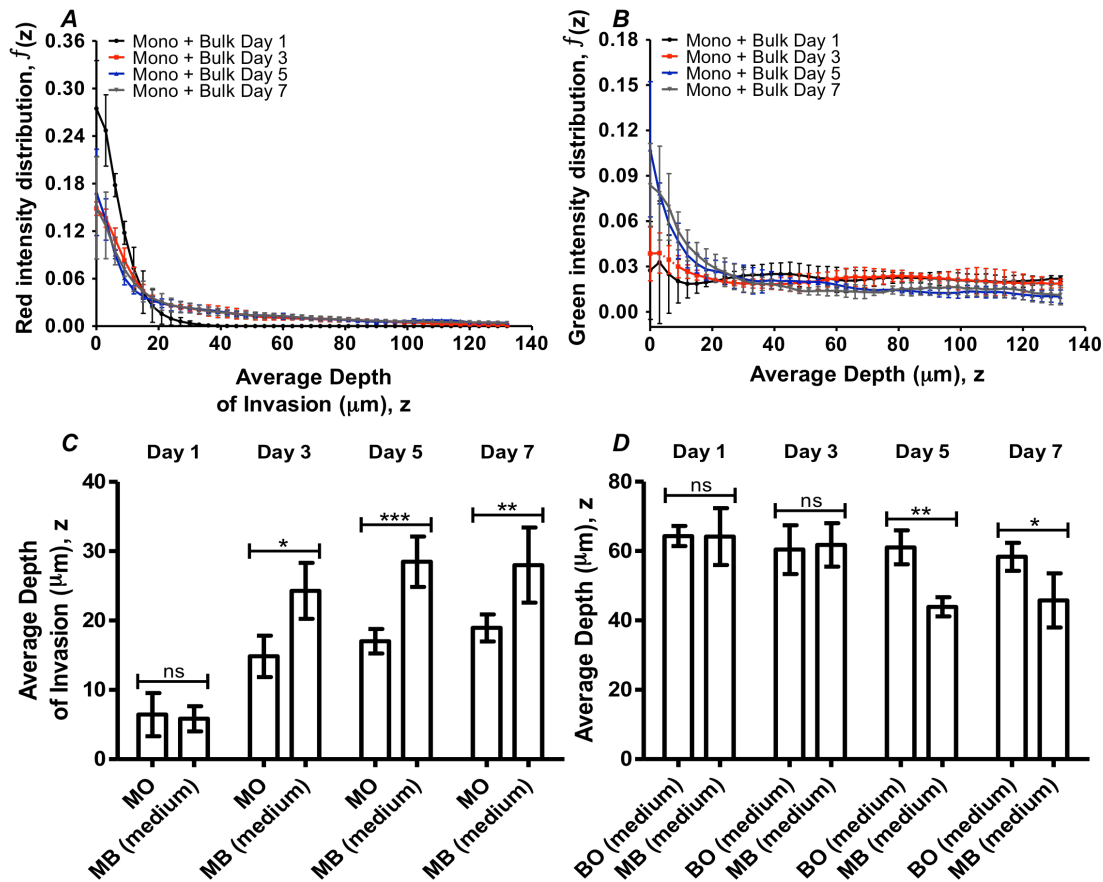


Figure 2-5: Depth distribution of cell populations with time. (A-B) Distributions of the fluorescence intensity in the depth measured from the position of the monolayer. Cells initially seeded on the surface of the gel (RFP⁺-HUVECs) (A); cells initially distributed within the bulk (GFP⁺-HUVECs) of the gels (B). BCs were seeded at a density of 1×10^6 cells/mL; MCs at 250 cells/ μm^2 . Time-points of Day 1 (black), Day 3 (red), Day 5 (blue), and Day 7 (grey) are shown. (C) Comparison of intensity-weighted average depth of invasion in Mono Only, “MO” and Mono + Bulk (medium), “MB (medium)” configurations. (D) Comparison of intensity-weighted average depth of BCs in Bulk Only (medium), “BO (medium)” and Mono + Bulk (medium), “MB (medium)” configurations. Error bar: Standard Deviation. (ns: not significant; *: $p < 0.05$; **: $p < 0.01$; ***: $p < 0.001$)

To further characterize the progression of these distributions of the two populations of cells, we calculated the first moments (or intensity weighted average depth; see *Section 2.3*) of the intensity distributions in configurations of Mono Only, Bulk Only (medium) and Mono + Bulk (medium), at designated time-points (**Fig. 2-5C, 2-5D**). We performed unpaired t-tests to compare red or green intensity of Mono + Bulk (medium) to Mono Only and Bulk Only respectively at each time-point. The tests identified significant differences in the average depth of MCs between Mono + Bulk (medium) and Mono Only at later time-points, indicating a role of BCs in promoting the migratory behavior of MCs (**Fig. 2-5C**). **Figure 2-5C** also shows that after 3 days of culture, the average depth of MCs in both Mono Only and Mono + Bulk (medium) approach a plateau at ~ 20 mm and ~ 30 mm respectively. We also note that as the culture time progressed, distribution of BCs shifted towards the monolayer, as indicated by lower values of average depth; this net migration of BCs was significantly larger for the Mono + Bulk (medium) than for the Bulk Only (medium) at Day 5 and Day 7 (**Fig. 2-5D**). This phenomenon suggests that the presence of MCs drove an upward migratory behavior of BCs. These results confirm the qualitative observations of inter-migration of MCs into the bulk (**Figs. 2-4A, 2-4B**) and presence of BCs on the monolayer (**Fig. 2-4A**).

2-2-5 Different cellular conditions: network robustness

To further explore the dependence of angiogenic invasion on cellular composition, we examined the impact of different cellular conditions on the ability of MCs to migrate into the bulk and anastomose with BCs. We first explored the idea that the depth to which MCs migrate would depend on the presence and concentration of BCs in the bulk. We

tested this hypothesis by exposing the MCs to a collagen containing BCs at a low bulk EC density (3×10^5 cells/mL - **Fig. 2-2D**) and a high bulk EC density (2×10^6 cells/mL - **Fig. 2-2F**), to compare with the medium bulk EC density case (1×10^6 cells/mL - **Fig. 2-2E**). In addition, we introduced pericytes (PCs) to the anastomosis model at a concentration of 2×10^5 cells/mL (**Fig. 2-2G**), a ratio of 1:5 to BCs [31], because PCs are known to associate with blood vessels and aid in their stabilization by providing quiescence cues to the morphogenetic vasculature [29,32].

Figures 2-6A-C present fluorescent micrographs across configurations of anastomosis models with different bulk EC densities after Day 7 of homotypic co-culture. We first observe that lumen structures formed of cells from both sub-populations appeared in all three configurations indicated by white arrowheads (**Fig. 2-6A-C**). Lumenized angiogenic sprouts formed purely of MCs (RFP⁺-HUVECs; asterisks) as well as lumens evolved via vasculogenesis from purely BCs (GFP⁺-HUVECs; white arrows) were present at $z = 45$ mm in both Mono + Bulk (low; **Fig. 2-6A**) and Mono + Bulk (medium; **Fig. 2-6B**). The Mono + Bulk (high) condition presents no structures of pure origin; we see only lumenized structures formed of both monolayer and bulk cells (arrow head; **Fig. 2-6C**). We further observe in **Figure 2-6A-C** that, although MCs intermixed with BCs at low BC density, as the density of BCs increased, lumens were more highly branched and interconnected. This characteristic is maximized in Mono + Bulk (high), with a dramatically larger number of the vascular structures present. Additionally, association between MCs and BCs became stronger as the density of BCs increased, as indicated by fewer individual angiogenic sprouts or lumens formed purely of BCs.

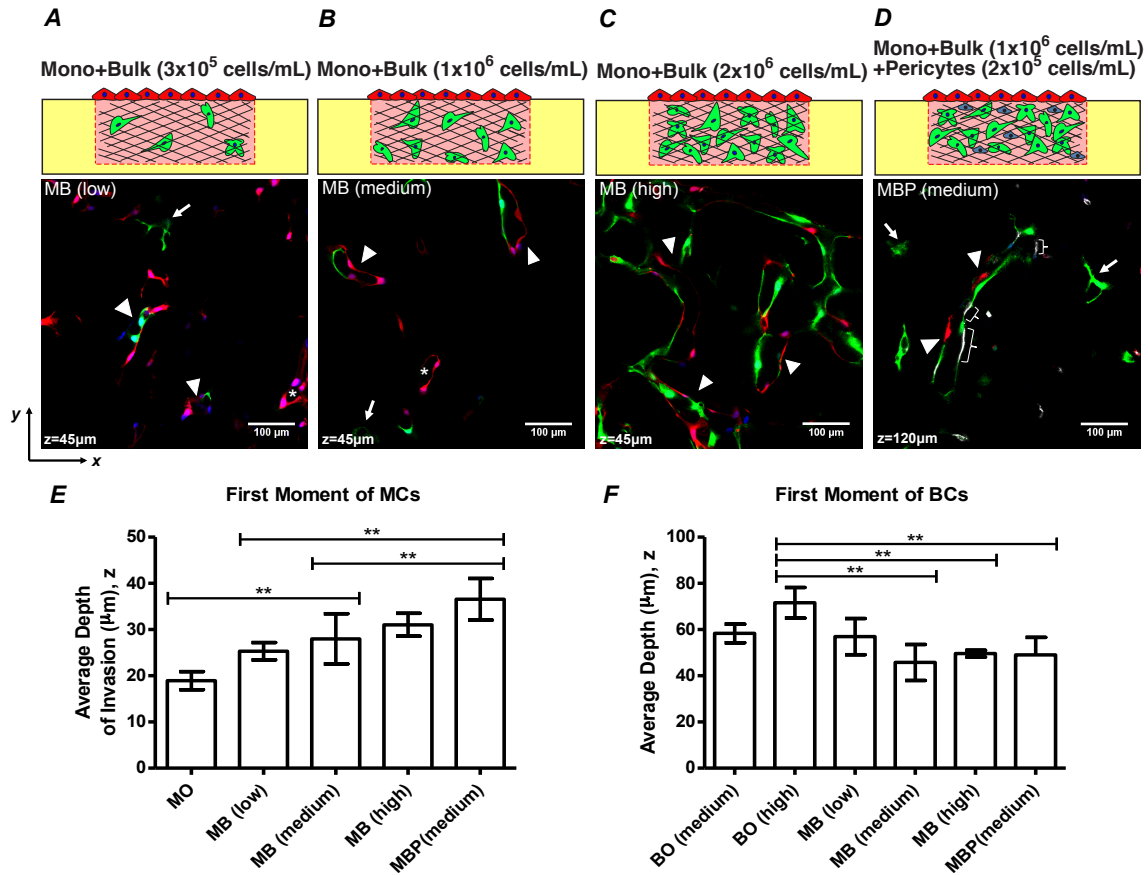


Figure 2-6: Comparison across configurations at Day 7. (A-D) Fluorescence confocal micrographs of horizontal planes within co-cultures after 7 days in culture. (A) Mono + Bulk with bulk density of 3×10^5 cells/mL, “MB (low)” (B) Mono + Bulk with bulk density of 1×10^6 cells/mL, “MB (medium)”. (C) Mono + Bulk with bulk density of 2×10^6 cells/mL, “MB (high)”. (D) Mono + Bulk (medium) + Pericytes with BC density of 1×10^6 cells/mL and PCs density of 2×10^5 cells/mL, “MBP (medium)”. Asterisk: angiogenic invasion from monolayer with lumen structures. Arrow: Lumen structures formed by *de novo* vasculogenesis. Arrowhead: Mixed cell lumen structures formed by anastomosis. Brace: staining of pericytes. (E) Comparison of intensity-weighted depth of MCs across configurations at Day 7. (F) Comparison of intensity-weighted depth of BCs distribution across configurations at Day 7. Error bars: Standard Deviation. (*: $p < 0.05$; **: $p < 0.01$)

Figure 2-6D presents a fluorescent micrograph of Mono + Bulk (medium) + Pericytes at $z = 120 \mu\text{m}$. Once again, we can observe lumens formed via vasculogenesis

(white arrows) as well as with intermixing of MCs and BCs (white arrowheads). We also identify a co-localization of PCs with vessel structures in the bulk collagen (**Fig. 2-6D**, white braces). Although further investigation is required, the observation that PCs are incorporated into the vessel structures to aid vessel maturation is consistent with expectations based on the literature.

Figures 2-6E-F present comparisons of average depths of both MCs and BCs at Day 7 across all configurations. Quantitatively, MCs migrated significantly deeper into the bulk collagen for the configurations of Mono + Bulk (medium), Mono + Bulk (high), and Mono + Bulk (medium) + Pericytes compared to the case of Mono Only (**Fig. 2-6E**). This observation suggests that the incorporation of BCs promoted the migration of MCs, even at low densities. Although more extensive lumen structures were present as the density of BCs increases (**Fig. 2-6A-C**), there is no statistically significant difference in the invasion depth of MCs among Mono + Bulk (low), Mono + Bulk (medium) and Mono + Bulk (high) (**Fig. 2-6E**). However, as the density of the BCs increases, instead of forming purely angiogenic sprouts, the MCs were incorporated into the lumen structures, which led to the intermixing feature via anastomosis. Looking closer at Mono + Bulk (medium) and Mono + Bulk (medium) + Pericytes, under the same cellular conditions but with the incorporation of pericytes in the bulk collagen, MCs migrated significantly deeper (**Fig. 2-6E**). Along with the qualitative observation of association of PCs with tubes (**Fig. 2-6D**), this increased invasion distance suggests that PCs facilitated vessel maturation in the bulk and in turns promoted the migration of MCs by allowing MCs to migrate along stable vessel structures. Additionally, the shift of BCs toward monolayer was observed quantitatively in the configurations where MCs were present except Mono

+ Bulk (low) (**Fig. 2-6F**). This observation is cohesive with the characteristic time-dependent shift of BCs in the case of Mono + Bulk (medium) in comparison to Bulk Only (medium) in **Figure 2-5D** which suggests that MCs promoted the upward migration of BCs.

2-2-6 Increased migration and intermixing

The intermixing of the two cell sub-populations (as seen clearly in **Fig. 2-6A-C**) was an unanticipated feature of the interactions during the process of anastomosis. The ability of individual MCs to rapidly incorporate into endothelial structures in the bulk, and the integration of BCs into the monolayer were striking observations. To explain these phenomenon, we hypothesize that the existing lumen structures serve as cellular tracks for MCs to migrate along; in other words, MCs prefer to migrate along the established tube structures instead of the extracellular matrix, a phenomenon previously reported in other contexts [33,34].

To test this hypothesis, an experiment with delayed seeding of MCs was conducted to examine the effects on the migration of MCs due to pre-existing vessel structures in the bulk collagen. Delayed seeding experiment was performed with culture of BCs in the collagen matrix for 4 days in pro-angiogenic media. At the end of the 4th day, RFP⁺-HUVECs were seeded on the surface of the collagen (hereafter referred as “delayed co-culture”) and the co-culture was carried on under the same conditions and terminated at designated time-points for comparison with the configuration of Mono + Bulk (medium). In other words, after four days of pre-culture of the BCs, the co-culture was cultured an additional period of one, three and five days and compared to co-seeding of bulk and monolayer cells cultured for these same periods.

We observe a significant difference on Day 1 between regular and delayed co-cultures (**Fig. 2-7**): In the delayed co-culture, the depth of invasion reached nearly 70% of the maximum observed for the regular case within the first day of co-culture; in the regular case, the MCs reached the same depth as in the delayed co-culture by Day 3. One possible origin of this behavior is that the rapid, early migration of MCs in the delayed case was facilitated by the collagen degradation during the pre-culture of BCs as Stratman [29] and others [35,36] have demonstrated the central role played by proteolysis during vasculogenesis and angiogenesis. Another possible mechanism is that the pre-existing lumen structures facilitate the migration of MCs. In other words, MCs were in close contacts with the lumen structures formed by BCs and utilized the lumen structures to migrate. This facilitation could be due to physical support provided by the tube structures as well as active surface interactions mediated by ligand-receptor pairs spanning the junctions between cells. Finally, another possible contributor is the pro-angiogenic effects of ECs [37] in the bulk on MCs; that is in the delayed seeding experiment, BCs were proliferating and secreting pro-angiogenic factors in the period of pre-culture. This extra time of secretion of pro-angiogenic factors could drive faster or more directed migration of MCs in the delayed co-culture compared to regular conditions (Mono + Bulk, medium), especially on Day 1.

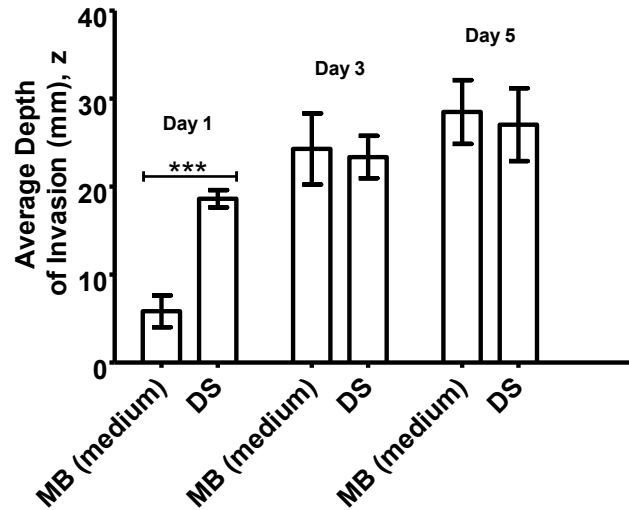


Figure 2-7: Invasion as a function of time of seeding. Comparison of intensity-weighted average depth of invasion of MCs in Mono + Bulk (medium), “MB (medium)” and Delayed Seeding, “DS”, at co-culture time-points of Day 1, Day 3 and Day5. The density of BCs in both configurations is 1×10^6 cells/mL. (***: $p < 0.001$)

2-2-7 Cellular track hypothesis

In order to assess the possible contribution of facilitated migration along pre-existing vessel structures, we performed a live imaging experiment (**Fig. 2-8**). After seven days of culture in pro-angiogenic media in a standard incubator, a series of horizontal confocal sections was captured with a time interval of 1 hour up to 13 hours for the configuration of Mono + Bulk (medium). **Figure 2-8** shows a vascularized lumen structure composed of both RFP⁺-HUVECs (MCs) and GFP⁺-HUVECs (BCs). The structure of the lumen changed dramatically during the time of imaging. Specifically, a single RFP⁺-HUVEC (MC) (circled by dashed line) migrated along the luminal tube and traveled from the top to the middle point in the field of view (**Fig. 2-8**). Similarly, another RFP⁺-HUVEC (MC) (circled by solid line) in the middle of the field of view migrated toward the bottom along the lumen structure (**Fig. 2-8**). This observation is compatible

with the hypothesis that pre-existing cellular structures act as conduits for cellular migration. We propose that this mechanism plays a role in the acceleration of EC migration and the formation of the mixed composition of tubes observed at later time points. We note that this observation does not exclude the possibility that proteolysis and secretion of growth factors operate in parallel with the process to increase the rate of sprouting and migration.

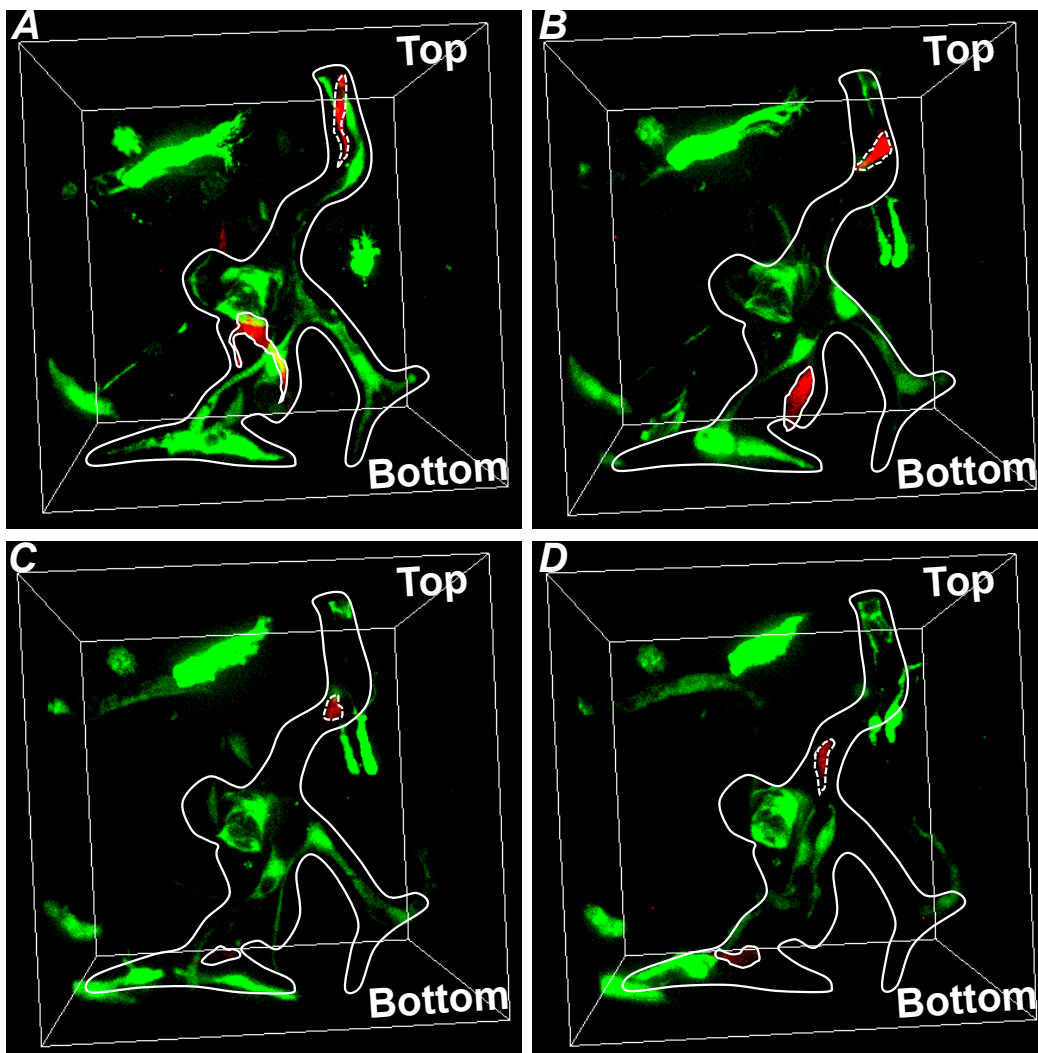


Figure 2-8: Live tracking of individual cells in Mono + Bulk (medium) on Day 7. (A) Time-point 1. **(B)** Time-point 5. **(C)** Time-point 9. **(D)** Time-point 14. Dashed line: cell 1; Solid line: cell 2. Each time point was separated by one hour.

2-3 Materials and methods

2-3-1 Reagents

The following cells, reagents, and materials were used: Human umbilical vein endothelial cells (HUVECs), 1× Medium 199 (1× M199), fetal bovine serum (FBS), L-glutamine, penicillin/streptomycin, trypsin/EDTA, HEPES buffered saline solution (Lonza); endothelial cell growth supplement (ECGS), basic fibroblast growth factor (bFGF), phosphate buffered saline (PBS) (Millipore); vascular endothelial cell growth factor (VEGF) (R&D Systems); rat tails (Pel-Freez Biologicals, Rogers AR); phorbol-12-myristate-13-acetate (PMA) (Cell Signaling Technology, Danvers, MA); (poly)ethylenimine (PEI) (MW 750,000) (Sigma-Aldrich, St. Louis, Missouri); heparin solution, 4',6-diamidino-2-phenylindole (DAPI), 10× Medium 199 (10× M199) (Invitrogen); Acetic Acid (Mallinckrodt Chemicals); L-ascorbic acid (Acros Organics, Atlanta, GA); Bovine Serum Albumin, Triton X-100 (MP Biomedicals, Inc., Solon, OH); (poly)-dimethylsiloxane (PDMS) (Sylgard[®] 184, Dow Corning, Midland, Michigan); glass coverslips (Fisher Scientific); Sodium Hydroxide (NaOH) (VWR); Biopsy Punches (Miltex by Kai); Glutaraldehyde (Fluka); Formaldehyde (Polysciences, Inc.).

2-3-2 Cell Culture Maintenance, Virus Production, Fluorescent Protein

Transduction and Collagen Stock Solution

HUVECs were used in passages 3-8. For expansion and maintenance, cells were cultured in M199 containing 20% FBS, 30 µg/mL of ECGS, 5 Units/ml of heparin solution, 2 mM of L-glutamine, and 150 U/ml of penicillin/streptomycin. This growth media (GM) was changed every 2-3 days. **Human Brain Vascular Pericytes (PCs)** were used in passages 2-5. PCs were cultured in PM containing 5% Fetal Bovine Serum (FBS)

and 1% penicillin/streptomycin. Both cell types were maintained at 5% CO₂ and 37°C. The constructs for lentivirus production were kindly provided by Dr. J. Lammerding's lab and were re-constructed to have mRuby2 and mNeonGreen fluorescent proteins respectively in-house with the help from Dr. Matthew Paszek's lab. The lentivirus production was carried out using 2nd generation packaging systems following a protocol provided by Dr. Matthew Paszek. A batch of HUVECs was transduced with viruses containing sequence of Red Fluorescent Protein (RFP) that is expressed constitutively inside the cell. Another batch was transduced with virus containing sequence of Green Fluorescent Protein (GFP) in a similar fashion.

Collagen was extracted from rat tails as described previously.[28] Acidic collagen solution was then lyophilized, and the dry mass was determined. The collagen was re-suspended in 0.1% v/v acetic acid to 15 mg/mL stock solution.

2-3-3 Preparation of Suspension of Cells in Collagen

Cells at 75-95% confluency were washed with 1× PBS, removed from culture flasks with 0.025% trypsin-EDTA, neutralized with GM, centrifuged, and re-suspended to a density of 3×10⁶ cells/mL. Cell-seeded collagen gels were prepared by mixing 10× M199 (1:10; compared to the desired final mixture volume), NaOH, 1N (1:50, compared to the required collagen stock volume), 1× M199 (as the last component added to complete final mixture volume), re-suspended HUVECs/PCs, and stock collagen solution. Both collagen solution and culture wells were kept on ice while preparing the suspension. NaOH, 10× M199, 1× M199, and collagen were mixed prior to adding cells in order to neutralize the collagen. The final pH of the solution was ~ 7.4. The working concentration of collagen was 6 mg/mL and the density of GFP⁺-HUVECs was 0.3 -

2×10^6 cells/mL. A volume of 1 mL of GM containing 50 $\mu\text{g/mL}$ of L-ascorbic acid, 50 ng/ml of PMA, 40 ng/ml of VEGF, and 40 ng/mL of bFGF was added to each well. We call this formulation Vasculogenesis Media (VM).

2-3-4 Preparation of PDMS Wells

Figure 2-9 depicts the process steps involved in making PDMS wells for the well assay. Uncured PDMS was poured onto a plexi-glass mold with an array of cylindrical posts 2-mm high and 4-mm in diameter. The mold had additional height to make a 2-mm thick base for each well. The mold with uncured PDMS was placed in an oven at 60°C for 2 hrs. Wells were separated from the master mold. Individual wells were separated from the array using a biopsy punch with an 8-mm diameter opening. An individual well of PDMS (**Fig. 2-9C**) was placed in the center of a well in a 24-well plate. The surface of PDMS wells was treated with oxygen plasma, dip-coated with 1% PEI for 10 minutes, and allowed to react with 0.1% glutaraldehyde for 30 minutes. These steps lead to covalent binding of collagen to the surfaces. Several rinses were performed thoroughly between each coating to avoid excess residuals of these chemicals. The 24-well plates containing coated PDMS wells were kept at 4°C before being loaded with cell-seeded (GFP⁺-HUVECs/PCs) or pure collagen. Cell-seeded or pure collagen were delivered to each well, a flat PDMS slab was positioned on top of the PDMS well, and the collagen was gelled inside an incubator for 30 minutes at 37°C.

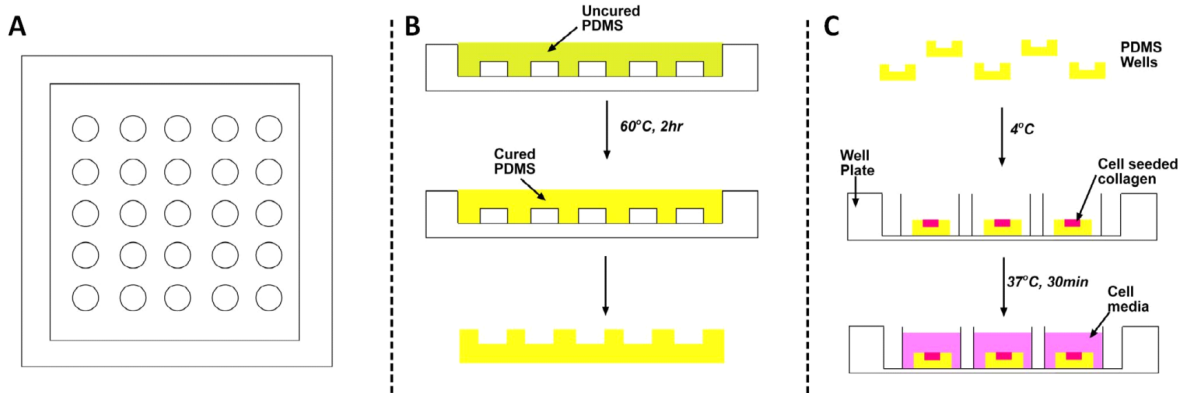


Figure 2-9: Generating PDMS wells for vertical anastomosis assays. (A) A plexi-glass mold formed by machining. **(B)** Uncured PDMS is molded onto the posts and cured. **(C)** Individual wells are punched out of the array of wells, placed in a standard well plate, seeded with cells and bathed in cell culture media.

2-3-5 Culture in Wells

Following gelation of collagen at 37°C for 30 minutes, a volume of RFP⁺-HUVECs suspension in GM was allowed to sit on the surface of the collagen-filled PDMS well for 2 hours inside an incubator. This volume of cell suspended media is predetermined to deposit a cell concentration of 250 cells/mm² of RFP⁺-HUVECs on the surface of the entire well to ensure a confluent monolayer of cells. VM was used to maintain the well assays. VM was replenished every 2 days.

2-3-6 Immunostaining

Cultures were fixed at designated time-points with 3.7% formaldehyde in PBS for 30 minutes, wash with 1× PBS carefully followed by blocking/permeablizing with 3% BSA, 0.5% Triton-X100 in 1× PBS for 1 hour at room temperature. The wells were then incubated with rabbit primary antibody to αSMA (Abcam ab32575) with ratio of 1:100 to 1% BSA in 1× PBS at 4°C over night. The wells were thoroughly washed then incubated

with Alexa Fluor® 647 Goat Anti-Rabbit IgG (Life Technologies P36930), DAPI, dilactate (Sigma-Aldrich) with a ratio of 1:100 and 1:1000 to 1% BSA in 1× PBS, respectively.

2-3-7 Microscopy and Image Analysis

Stacks of images of horizontal sections (567 μm by 567 μm) were acquired at 3 μm-intervals in the vertical direction using confocal microscopy (Zeiss 710). A water immersion 25× Carl Zeiss objective with a numerical aperture of 0.8 was used. The normalized pinhole was 28 μm and the scan zoom was set to 0.6. The end position used to collect a stack was varied but was always greater than 150 μm. Every well was taken to represent an independent experiment. Three locations away from the wall were randomly selected for a given culture well, and the average of stacks acquired at these positions in each well was reported as an independent experimental value (average of the normalized intensities, with respect to the total intensity in a stack, over the three positions at each depth – see **Eq. 1** for normalization). A custom Matlab® code was created to separate the red and green channels from the collected image stacks and to perform subsequent analyses (**Fig. 2-10**). To extract intensity distributions through the depth of the culture, $f(z)$, the total intensity of each color channel in each slice, $\sum_m I_z(m)$, was calculated and normalized with respect the total intensity in that channel in the entire stack:

$$f(z) = \frac{\sum_m I_z(m)}{\sum_z \sum_m I_z(m)} \quad , \quad (1)$$

where m is the index of the pixels and z is the index of the slices. The slice $z = 0$ of the stack of images was defined as the slice with highest intensity in the red channel which represents the monolayer.

To characterize the depth distributions we calculated the depth-weighted average or first moment of the intensity distribution, μ_1 , as follows:

$$\mu_1 = \sum z f(z). \quad (2)$$

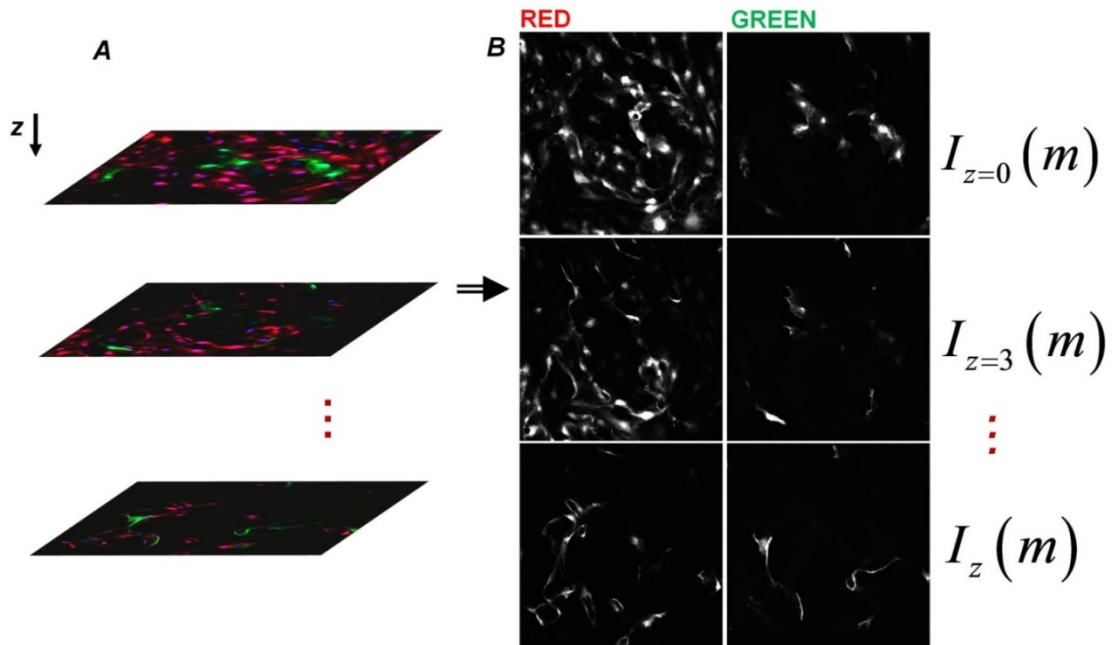


Figure 2-10: Analysis method for vertical anastomosis assays. (A) Stacks of $3\mu\text{m}$ -spaced images were collected using confocal microscopy. Every well represents an independent experiment. Three random non-overlapping locations within a well were used for averaging. (B) A custom Matlab® code was created to separate the red and green channels from the collected image stacks. The total intensity of an image (I) is

tracked along z-direction to characterize the distribution of red and green structures. m is the linear index of the intensity matrix elements.

2-4 Conclusions

This study utilized 3-D assays to recapitulate angiogenesis, vasculogenesis and a combination of both, *in vitro* with a focus on understanding the cell dynamics during and after anastomosis. We present the first reported evidence that anastomosis can occur between angiogenic sprouts and tubes formed by vasculogenesis in such a homotypic co-culture system. In this study, ECs originally in the monolayer via sprouting angiogenesis, extended continuously into the bulk collagen, while ECs originally in the bulk collagen underwent vasculogenesis; after the two processes anastomosed, ECs inter-dispersed themselves in the vascular structures. This cellular interaction *in vitro* could be analogous to the context of wound healing where the dispersed endothelial progenitor cells in disrupted tissue in the wound bed undergo vasculogenesis while sprouting angiogenesis occurs from intact vessels in the surrounding tissue [38,39].

We found that this process of anastomosis presented is dependent on seeding density of ECs in the bulk collagen: higher densities of ECs in the bulk collagen led to more highly interconnected vessels with the incorporation of cells from the monolayer in the vessel structures in the bulk. Additionally, vasculogenesis in the bulk was promoted with increasing seeding density in the bulk, with larger and more highly branched lumen structures formed.

The unexpected feature of the anastomosis process in our system was that the populations of MCs and BCs did not connect with each other to form a hybrid vessel with

a sharp transition between cells of distinct origin (**Fig. 2-1C**). Instead, these populations were found intermixed, with monolayer cells interspersed among bulk cells in vessel structures (**Fig. 2-4A, Fig. 2-6**) and bulk cells incorporated into the surface endothelium (**Fig. 2-4A**). Live microscopy indicated that cellular migration along pre-existing vessel structures plays a role in this dispersal process. This process, in which cellular networks act as tracks (“cellular tracks”), has been described in several other contexts, for example: networks of follicular dendritic cells served as a substratum for movement of follicular B cells within lymph nodes [34], angiogenic sprouts are found to be closely associated (or migrating) over astrocytic tracks [33], and motility of EC-associated pericytes depends on the presence of endothelial tubes [40].

Although *in vivo* and *in vitro* studies have studied cell dynamics by inducing the cell migrations through wound models [41–44], we have lacked tools with which to look at cell dynamics in anastomosis of blood vessel. This study showed that ECs are highly motile during and after anastomosis. The migratory behaviors of ECs along the cellular networks are potentially among the pre-requisites for remodeling and maturation of blood vessels, and need to be considered in the studies of blood vessel formation. The simple experimental platform introduced here provides a new basis for studying anastomosis *in vitro* and could open a new route to the formation of extensive networks of capillaries in engineered tissues.

2-5 **References**

- [1] P. Carmeliet, Angiogenesis in life, disease and medicine., Nature. 438 (2005) 932–6. doi:10.1038/nature04478.
- [2] J. Folkman, Angiogenesis: an organizing principle for drug discovery?, Nat. Rev.

- Drug Discov. 6 (2007) 273–86. doi:10.1038/nrd2115.
- [3] P. Carmeliet, R.K. Jain, Angiogenesis in cancer and other diseases., *Nature*. 407 (2000) 249–57. doi:10.1038/35025220.
- [4] C.A. Staton, S.M. Stribbling, S. Tazzyman, R. Hughes, N.J. Brown, C.E. Lewis, Current methods for assaying angiogenesis in vitro and in vivo., *Int. J. Exp. Pathol.* 85 (2004) 233–48. doi:10.1111/j.0959-9673.2004.00396.x.
- [5] G.E. Davis, A.N. Stratman, A. Sacharidou, W. Koh, Molecular basis for endothelial lumen formation and tubulogenesis during vasculogenesis and angiogenic sprouting., 1st ed., Elsevier Inc., 2011. doi:10.1016/B978-0-12-386041-5.00003-0.
- [6] M. Potente, H. Gerhardt, P. Carmeliet, Basic and therapeutic aspects of angiogenesis., *Cell*. 146 (2011) 873–87. doi:10.1016/j.cell.2011.08.039.
- [7] Z. Ahmed, R. Bicknell, Angiogenic signalling pathways., *Methods Mol. Biol.* 467 (2009) 3–24. doi:10.1007/978-1-59745-241-0_1.
- [8] I. Geudens, H. Gerhardt, Coordinating cell behaviour during blood vessel formation., *Development*. 138 (2011) 4569–83. doi:10.1242/dev.062323.
- [9] H.M. Eilken, R.H. Adams, Dynamics of endothelial cell behavior in sprouting angiogenesis., *Curr. Opin. Cell Biol.* 22 (2010) 617–25. doi:10.1016/j.ceb.2010.08.010.
- [10] L. Lamalice, F. Le Boeuf, J. Huot, Endothelial cell migration during angiogenesis., *Circ. Res.* 100 (2007) 782–94. doi:10.1161/01.RES.0000259593.07661.1e.
- [11] L. Jakobsson, C. a Franco, K. Bentley, R.T. Collins, B. Ponsioen, I.M. Aspalter, I.

- Rosewell, M. Busse, G. Thurston, A. Medvinsky, S. Schulte-Merker, H. Gerhardt, Endothelial cells dynamically compete for the tip cell position during angiogenic sprouting., *Nat. Cell Biol.* 12 (2010) 943–53. doi:10.1038/ncb2103.
- [12] J. Featherstone, S. Griffiths, From the analyst’s couch. Drugs that target angiogenesis., *Nat. Rev. Drug Discov.* 1 (2002) 413–4. doi:10.1038/nrd824.
- [13] P. Carmeliet, R.K. Jain, Molecular mechanisms and clinical applications of angiogenesis., *Nature.* 473 (2011) 298–307. doi:10.1038/nature10144.
- [14] A.D. Metcalfe, M.W.J. Ferguson, Tissue engineering of replacement skin: the crossroads of biomaterials, wound healing, embryonic development, stem cells and regeneration., *J. R. Soc. Interface.* 4 (2007) 413–37. doi:10.1098/rsif.2006.0179.
- [15] A. Atala, S.B. Bauer, S. Soker, J.J. Yoo, A.B. Retik, Tissue-engineered autologous bladders for patients needing cystoplasty., *Lancet.* 367 (2006) 1241–6. doi:10.1016/S0140-6736(06)68438-9.
- [16] N. L’Heureux, N. Dusserre, G. Konig, B. Victor, P. Keire, T.N. Wight, N.A.F. Chronos, A.E. Kyles, C.R. Gregory, G. Hoyt, R.C. Robbins, T.N. McAllister, Human tissue-engineered blood vessels for adult arterial revascularization., *Nat. Med.* 12 (2006) 361–5. doi:10.1038/nm1364.
- [17] Y. Ikada, Challenges in tissue engineering., *J. R. Soc. Interface.* 3 (2006) 589–601. doi:10.1098/rsif.2006.0124.
- [18] A. Krogh, The number and distribution of capillaries in muscles with calculations of the oxygen pressure head necessary for supplying the tissue., *J. Physiol.* 52 (1919) 409–15.

<http://www.pubmedcentral.nih.gov/articlerender.fcgi?artid=1402716&tool=pmcentrez&rendertype=abstract> (accessed July 4, 2014).

- [19] N.W. Choi, M. Cabodi, B. Held, J.P. Gleghorn, L.J. Bonassar, A.D. Stroock, Microfluidic scaffolds for tissue engineering., *Nat. Mater.* 6 (2007) 908–15. doi:10.1038/nmat2022.
- [20] W. Risau, Mechanisms of angiogenesis., *Nature.* 386 (1997) 671–4. doi:10.1038/386671a0.
- [21] E.I. Chang, M.G. Galvez, J.P. Glotzbach, C.D. Hamou, S. El-ftesi, C.T. Rappleye, K.-M. Sommer, J. Rajadas, O.J. Abilez, G.G. Fuller, M.T. Longaker, G.C. Gurtner, Vascular anastomosis using controlled phase transitions in poloxamer gels., *Nat. Med.* 17 (2011) 1147–52. doi:10.1038/nm.2424.
- [22] J.M. Chan, I.K. Zervantonakis, T. Rimchala, W.J. Polacheck, J. Whisler, R.D. Kamm, Engineering of in vitro 3D capillary beds by self-directed angiogenic sprouting., *PLoS One.* 7 (2012) e50582. doi:10.1371/journal.pone.0050582.
- [23] J.W. Song, D. Bazou, L.L. Munn, Anastomosis of endothelial sprouts forms new vessels in a tissue analogue of angiogenesis., *Integr. Biol. (Camb).* 4 (2012) 857–62. doi:10.1039/c2ib20061a.
- [24] J.H. Yeon, H.R. Ryu, M. Chung, Q.P. Hu, N.L. Jeon, In vitro formation and characterization of a perfusable three-dimensional tubular capillary network in microfluidic devices., *Lab Chip.* 12 (2012) 2815–22. doi:10.1039/c2lc40131b.
- [25] M.L. Moya, Y.-H. Hsu, A.P. Lee, C.C.W. Hughes, S.C. George, In Vitro Perfused Human Capillary Networks., *Tissue Eng. Part C. Methods.* 19 (2013) 730–7.

doi:10.1089/ten.TEC.2012.0430.

- [26] L.L.Y. Chiu, M. Montgomery, Y. Liang, H. Liu, M. Radisic, Perfusible branching microvessel bed for vascularization of engineered tissues., *Proc. Natl. Acad. Sci. U. S. A.* 109 (2012) E3414-23. doi:10.1073/pnas.1210580109.
- [27] W. Koh, A.N. Stratman, A. Sacharidou, G.E. Davis, In vitro three dimensional collagen matrix models of endothelial lumen formation during vasculogenesis and angiogenesis., *Methods Enzymol.* 443 (2008) 83–101. doi:10.1016/S0076-6879(08)02005-3.
- [28] V.L. Cross, Y. Zheng, N. Won Choi, S.S. Verbridge, B.A. Sutermeister, L.J. Bonassar, C. Fischbach, A.D. Stroock, Dense type I collagen matrices that support cellular remodeling and microfabrication for studies of tumor angiogenesis and vasculogenesis in vitro., *Biomaterials.* 31 (2010) 8596–607. doi:10.1016/j.biomaterials.2010.07.072.
- [29] A.N. Stratman, W.B. Saunders, A. Sacharidou, W. Koh, K.E. Fisher, D.C. Zawieja, M.J. Davis, G.E. Davis, Endothelial cell lumen and vascular guidance tunnel formation requires MT1-MMP-dependent proteolysis in 3-dimensional collagen matrices., *Blood.* 114 (2009) 237–47. doi:10.1182/blood-2008-12-196451.
- [30] A. Lenard, E. Ellertsdottir, L. Herwig, A. Krudewig, L. Sauteur, H.-G. Belting, M. Affolter, In vivo analysis reveals a highly stereotypic morphogenetic pathway of vascular anastomosis., *Dev. Cell.* 25 (2013) 492–506. doi:10.1016/j.devcel.2013.05.010.
- [31] a. N. Stratman, K.M. Malotte, R.D. Mahan, M.J. Davis, G.E. Davis, Pericyte

recruitment during vasculogenic tube assembly stimulates endothelial basement membrane matrix formation, *Blood*. 114 (2009) 5091–5101. doi:10.1182/blood-2009-05-222364.

- [32] D. von Tell, A. Armulik, C. Betsholtz, Pericytes and vascular stability., *Exp. Cell Res.* 312 (2006) 623–9. doi:10.1016/j.yexcr.2005.10.019.
- [33] H. Gerhardt, M. Golding, M. Fruttiger, C. Ruhrberg, A. Lundkvist, A. Abramsson, M. Jeltsch, C. Mitchell, K. Alitalo, D. Shima, C. Betsholtz, VEGF guides angiogenic sprouting utilizing endothelial tip cell filopodia., *J. Cell Biol.* 161 (2003) 1163–77. doi:10.1083/jcb.200302047.
- [34] M. Bajénoff, J.G. Egen, L.Y. Koo, J.P. Laugier, F. Brau, N. Glaichenhaus, R.N. Germain, Stromal cell networks regulate lymphocyte entry, migration, and territoriality in lymph nodes., *Immunity*. 25 (2006) 989–1001. doi:10.1016/j.immuni.2006.10.011.
- [35] J.E. Rundhaug, Matrix metalloproteinases and angiogenesis., *J. Cell. Mol. Med.* 9 267–85. <http://www.ncbi.nlm.nih.gov/pubmed/15963249> (accessed July 25, 2014).
- [36] V.W.M. van Hinsbergh, M.A. Engelse, P.H.A. Quax, Pericellular proteases in angiogenesis and vasculogenesis., *Arterioscler. Thromb. Vasc. Biol.* 26 (2006) 716–28. doi:10.1161/01.ATV.0000209518.58252.17.
- [37] H.F. Galley, N.R. Webster, Physiology of the endothelium., *Br. J. Anaesth.* 93 (2004) 105–13. doi:10.1093/bja/ae163.
- [38] H. Masuda, Post-natal endothelial progenitor cells for neovascularization in tissue regeneration, *Cardiovasc. Res.* 58 (2003) 390–398. doi:10.1016/S0008-

6363(02)00785-X.

- [39] A.L. George, P. Bangalore-Prakash, S. Rajoria, R. Suriano, A. Shanmugam, A. Mittelman, R.K. Tiwari, Endothelial progenitor cell biology in disease and tissue regeneration., *J. Hematol. Oncol.* 4 (2011) 24. doi:10.1186/1756-8722-4-24.
- [40] A.N. Stratman, A.E. Schwindt, K.M. Malotte, G.E. Davis, Endothelial-derived PDGF-BB and HB-EGF coordinately regulate pericyte recruitment during vasculogenic tube assembly and stabilization., *Blood.* 116 (2010) 4720–30. doi:10.1182/blood-2010-05-286872.
- [41] F. Castellino, A.Y. Huang, G. Altan-Bonnet, S. Stoll, C. Scheinecker, R.N. Germain, Chemokines enhance immunity by guiding naive CD8⁺ T cells to sites of CD4⁺ T cell-dendritic cell interaction., *Nature.* 440 (2006) 890–5. doi:10.1038/nature04651.
- [42] M. Reffay, L. Petitjean, S. Coscoy, E. Grasland-Mongrain, F. Amblard, a Buguin, P. Silberzan, Orientation and polarity in collectively migrating cell structures: statics and dynamics., *Biophys. J.* 100 (2011) 2566–75. doi:10.1016/j.bpj.2011.04.047.
- [43] M. Poujade, E. Grasland-Mongrain, A. Hertzog, J. Jouanneau, P. Chavrier, B. Ladoux, A. Buguin, P. Silberzan, Collective migration of an epithelial monolayer in response to a model wound., *Proc. Natl. Acad. Sci. U. S. A.* 104 (2007) 15988–93. doi:10.1073/pnas.0705062104.
- [44] M. Reffay, M.C. Parrini, O. Cochet-Escartin, B. Ladoux, a Buguin, S. Coscoy, F. Amblard, J. Camonis, P. Silberzan, Interplay of RhoA and mechanical forces in

collective cell migration driven by leader cells., *Nat. Cell Biol.* 16 (2014) 217–23.

doi:10.1038/ncb2917.

CHAPTER 3

MULTI-SCALE STUDY OF WARBURG EFFECT, REVERSE WARBURG EFFECT AND GLUTAMINE ADDICTION IN SOLID TUMORS

This chapter is adapted from a submitted manuscript:

M. Shan, D. Dai, A. Vudem, J.D. Varner, A.D. Stroock. Multi-scale study of Warburg effect, reverse Warburg effect and glutamine addiction in solid tumors. Submitted.

3-1 Introduction

Cancer remains one of the leading causes of death worldwide. A central challenge in understanding and treating cancer comes from its multi-scale nature, with interacting defects at the molecular, cellular and tissue scales. Specifically, the molecular profile at the intracellular level, behavior at the single-cell level and the interactions between tumor cells and the surrounding tissues all influence tumor progression and complicate extrapolation from molecular and cellular properties to tumor behavior [1–3]. Understanding the multi-scale responses of cancer to microenvironmental stress could provide important new insights into tumor progression and aid the development of new therapeutic strategies [2]. Therefore, cancer must be studied and treated as a cellular ecology made up of the individual cells and their microenvironment. This ecological view should account for the competition and cooperation of different molecular and cellular players, and for both the physical and biological characteristics of the environment in which tumor evolves. Such

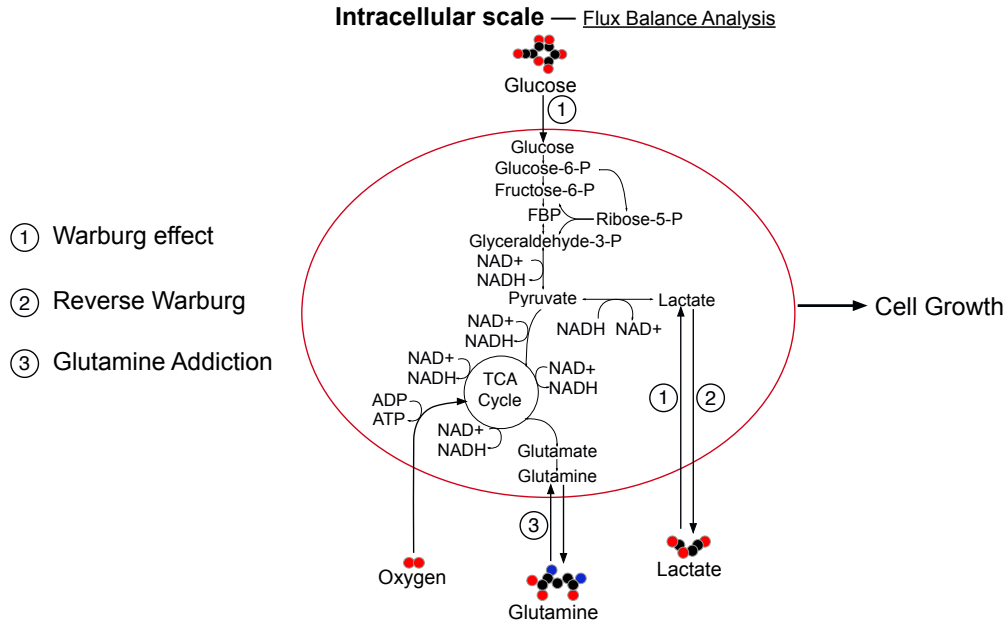
perspectives complement studies of the genetic drivers of tumor and potentially provide new bases for treating this disease [4].

Central to an ecological perspective of tumors is metabolism, the biochemical process by which cells derive energy and biomass from the nutrients available in their environment while excreting products of metabolism back to the environment. This exchange of metabolites impacts the distribution of resources in the environment and sets constraints on the availability of resources to individual cells [5]. Therefore, metabolism couples the behavior of individual cells to the characteristics – spatial-temporal organization and phenotypic make-up – of the full population. Recently, cancer metabolism has drawn renewed attention in the field of cancer biology [4,6]. Following the early observations of the unique tissue-scale metabolic profile of tumors made by Otto Warburg in the 1920s, discoveries of oncogenes and molecular cues in tumor-associated metabolic alterations have renewed the hope for therapeutic routes that target cancer metabolism [7].

In his seminal work, Warburg noted the distinct metabolic profile of tumor cells with high glycolytic rate and lactate production in the presence of oxygen. This so-called Warburg effect or aerobic glycolysis has been widely observed in different types of tumor cells (**Fig. 3-1A, ①**) [8]. This original observation by Warburg led him to hypothesize that aerobic glycolysis is caused by impaired respiration; in turn, this defect results in cancer [9]. It is now well accepted that this hypothesis is incorrect as most tumor cells retain functional mitochondria [10,11]; we still lack a full understanding of the origin and consequences of the Warburg effect. More recently, other hypotheses have been proposed in the field of cancer metabolism such as the reverse Warburg effect (**Fig. 3-1A, ②**) and glutamine addiction (**Fig. 3-1A, ③**) [3,12–16]. Despite support of these three hypotheses from various experimental

studies, significant uncertainty remains with respect to their definitions, their origin, and their impact on tumor progression and therapeutic interventions. Unraveling these fundamental questions could open a clearer path to targeting cancer metabolism as a therapeutic strategy.

A



B

Cellular scale

$$q_{i/n} = -\frac{\mu_{m,n}}{Y_{i/n}} \quad \text{(Equation 1)} \quad m = \text{individual cell type}$$

$$\frac{dX_m}{dt} = X_m \cdot \sum_n \mu_{m,n} \cdot f_n(C_j)_{\text{Monod}} \quad \text{(Equation 2)} \quad n = \text{metabolic phenotype}$$

$$\frac{dV_m}{dt} = \frac{1}{\rho} \cdot \frac{dX_m}{dt} \quad \text{(Equation 3)} \quad i, j = \text{metabolite}$$

C

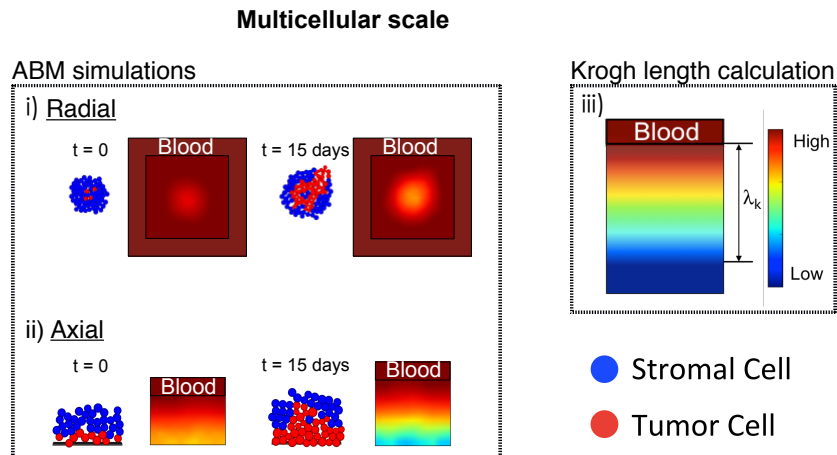


Figure 3-1: Multi-scale modeling of cancer metabolism. (A) **Intracellular scale: Flux Balance Analysis (FBA).** The arrows represent fluxes of species within a reduced representation of cell metabolism and cell growth; the detailed network used in FBA is presented in Figure 3-8. Key steps associated with three hypotheses are labeled: ① Warburg effect which is distinguished by high glycolytic flux and lactate production. ② Reverse Warburg which is distinguished by the uptake of lactate. ③ Glutamine addiction which is distinguished by uptake of glutamine as a carbon source to feed TCA cycle. (B) **Cellular scale:** uptake and production rates ($q_{i/n}$ [g/g-DW-hr]) are obtained from FBA and used to obtain yield coefficients ($Y_{i/n}$ [g/g-DW]) for each metabolite (i) and corresponding metabolic phenotype (n) (Equation 1). Biomass (X_m [g]) growth of each cell type is modeled as a Monod-like process parameterized by maximum growth rate at specific metabolic phenotype, $\mu_{m,n}$ [hr⁻¹] and a function of metabolite concentrations, $f_n(\{C_j\})_{Monod}$ (Equation 2). The change in Volume of the cell (V_m [L]) is calculated from biomass growth by applying a constant density of the cell (ρ [g-DW/L]) (Equation 3). These equations are solved within an agent-based model. (C) **Agent-based model (ABM):** The iDynaMiCS simulation package is used to track the growth of individual cells within a continuum matrix in which metabolites diffuse. Additionally, concentration of the i^{th} metabolite (C_i [g/L]) is tracked via a reaction-diffusion equation linked to biomass (term 2 in Equation 4). D_i [m²/hr] is diffusivity of the i^{th} metabolite. Cells are treated as hard spheres. [17]. i) Radial, two-dimensional growth: Tumor cells grow radially out from an initial cluster of cells with metabolites supplied at the edge of the cell mass such that radial gradients of concentration emerge (color map). Two phenotypes are displayed (red tumor cells and blue stroma cells). As the tumor grows, concentration gradients of metabolites become significant, making the tumor growth a diffusion-limited process that can result in different growth dynamics as well as distinct spatial distribution of cell subpopulations. ii) Axial, one-dimensional growth: Layers of tumor cells (red) and stromal cells (blue) are initiated near a blood vessel that supplies metabolites (from the top), such as glucose and oxygen in the blood stream. Growth pushes cells deeper into the tissue, away from the vessel, such that strong gradients of metabolite can again occur. iii) **Krogh length calculation:** To evaluate the impact of diffusion limitations in a simple model, we treat cells as continuum with uniform, zeroth order kinetics of metabolite consumption to calculate the distance over which the concentration of limiting metabolites falls to zero within the tumor mass; we refer to this distance as the Krogh length of a given metabolite.

In the past few years, studies of cancer metabolism have begun to elucidate how the metabolic alterations in tumor cells can influence tumor progression [9,18–21]. A definitive characteristic of tumor cells is uncontrolled proliferation. Compared to healthy cells that remain quiescent in most of their life cycle, tumor cells proliferate rapidly, accompanied by

high rates of metabolic uptake. This metabolic profile of tumor cells leads to significant depletion of metabolites in the local microenvironment, resulting in resource limitations. Additionally, byproducts and waste products produced by the metabolism of tumor cells can potentially hinder the growth of neighboring cells or act as sources of alternative metabolic substrates [16,22,23]. Although studies have made efforts to capture these experimental observations mathematically [21,24–29], we are unaware of computational studies that test the implications of these hypotheses with respect to metabolic behaviors at the individual cell level, intercellular interactions mediated by shared metabolic environment, and the collective behavior that together define fitness, growth potential, and potential responsiveness to therapeutic intervention. Recent computational work has made progress toward capturing the multi-scale complexity of cancer. These studies investigated the effect of tumor microenvironmental factors, specifically molecular cues and metabolites, on tumor population dynamics and provided insights into the cooperative behaviors of tumor subpopulations [30–34]. Similar intraspecies competition or cooperation are often observed in microbial organisms and heavily studied from a population ecology perspective [35–37]. Theories and modeling tools are better developed in the microbial field due to the relatively convenient validation from experiments [17,38,39].

In this study, we take a multi-scale modeling approach to describe the intracellular, cellular, and multicellular behaviors of cells within a tumor (**Fig. 3-1**). With this framework, we investigate the following hypotheses: Warburg Effect/Aerobic glycolysis (①), Reverse Warburg (②), and Glutamine Addiction (③). We begin by translating hypotheses from experimental studies into constraints and objectives within the FBA (**Fig. 3-1A**). We proceed to use FBA to obtain the yield coefficients ($Y = \text{maximum growth rate/flux of metabolite}$) for

use in Monod-like kinetics of cellular growth at the individual cell level as represented in Equations 1-3 in **Figure 3-1B**. Finally, we simulate the growth dynamics of these cells at the multicellular scale to elucidate the implications of these metabolic scenarios (**Fig. 3-1C**). We address the impact of the metabolic phenotypes implied by current hypotheses on the growth dynamics of tumor cells in the resource-limited microenvironments that emerge after tumor initiation. This modeling framework opens a route to explore tissue-scale tumor dynamics with explicit account taken for these metabolic scenarios in an efficient manner.

3-2 Model

3-2-1 Scale-bridging model formulation

Figure 3-1 illustrates, schematically, the multi-scale approaches we use. At the intracellular scale, we use Flux Balance Analysis (FBA) to construct a network that captures the central metabolism of mammalian cells (“Intracellular scale” in **Fig. 3-1**). We build the biomass template reaction based on major precursors for biomass synthesis by reducing Shlomi and coworker’s genome scale biomass template [21]. We impose a cellular maintenance reaction with a baseline rate to define the required minimum metabolism of cells (see Methods). We modify constraints and objective functions within the FBA network to define the characteristics of the different hypotheses (labeled in **Fig. 3-1A**, also see Methods). We acknowledge that the altered metabolic phenotype of tumor cells may be due to prior genetic events that occurred in the cell, such as loss of tumor suppressors (e.g., p53) [40]. However, we only consider the metabolic phenotypes of the cells at fixed genetic profiles here since we focus on impact of metabolic profiles on tumor growth over time scales (days) that are short relative to those required for the emergence and accumulation of genetic alterations in the cells (months or years). We estimate parameters (e.g., maximum

growth rates of different cell types at different growth conditions, $\mu_{m,n}$) based on literature (see **Table 3-1**). At the cellular scale (**Fig. 3-1B**), we use the metabolic uptake and production rates of the metabolites obtained from FBA to determine yield coefficients (Equation 1 in **Fig. 3-1B**) for a Monod-like treatment of growth kinetics (Equation 2 in **Fig. 3-1B**). Additionally, we use a threshold in cell diameter to define the doubling of the cell by linking biomass growth to the volume expansion of the cell at a fixed density (Equation 3 in **Fig. 3-1B**). To bridge the treatment of metabolic processes at the cellular and multicellular scales, we solve steady state species balances for each explicit metabolite at each time step within iDynoMiCS [17]:

$$\frac{\partial C_i}{\partial t} = D_i \nabla^2 C_i + \sum_m \rho \sum_n q_{i/n} \cdot f_n(C_j)_{Monod} \quad (4)$$

where C_i [g/L] is the concentration of i^{th} metabolite, D_i [m^2/day] is the diffusion coefficient of i^{th} metabolite, ρ [g-DW/L] is the dry mass density of the cell, $q_{i/n}$ [g/g-DW-hr] is the uptake/production rate of i^{th} metabolite in the n^{th} phenotype and $f_n(C_j)_{Monod}$ is the Monod function of metabolite concentrations. Here, the species balances can be safely treated as being at steady state because the time step in our simulation (1 hour) is selected to resolve cell growth and is long compared to typical transients in metabolism [17].

	Cell Type (m)	Phenotype (n)	$\mu_{m,n}$ (hr ⁻¹)	$q_{Glu/n}$ (g/g-DW-hr)	$q_{O2/n}$ (g/g-DW-hr)	$q_{Lac/n}$ (g/g-DW-hr)	$q_{Gln/n}$ (g/g-DW-hr)	$Y_{Glu/n}$ (g-DW/g)	$Y_{O2/n}$ (g-DW/g)	$Y_{Lac/n}$ (g-DW/g)	$Y_{Gln/n}$ (g-DW/g)
Warburg Effect	Healthy Stromal Cell	Aerobic	1×10^{-6}	-0.045	-0.048	N/A	N/A	2.22×10^{-5}	2.08×10^{-5}	N/A	N/A
		Anaerobic	1×10^{-6}	-0.45	-3.2×10^{-7}	N/A	N/A	2.22×10^{-6}	3.13	N/A	N/A
	Warburg Tumor Cell	Aerobic, WN = 0	0.018	-0.078	-0.064	N/A	N/A	0.231	0.281	N/A	N/A
		Aerobic, WN = 2	0.018	-0.183	-0.052	N/A	N/A	0.098	0.349	N/A	N/A
		Aerobic, WN = 10	0.018	-0.394	-0.0266	N/A	N/A	0.0456	0.68	N/A	N/A
		Aerobic, WN = 34	0.018	-0.573	-0.006	N/A	N/A	0.031	2.953	N/A	N/A
	Anaerobic	1×10^{-6}	-0.45	-3.2×10^{-7}	N/A	N/A	2.22×10^{-6}	3.13	N/A	N/A	
Reverse Warburg Effect	Hijacked Stromal Cell	Aerobic	1×10^{-6}	-0.45	-3.2×10^{-7}	0.45	N/A	2.22×10^{-6}	3.13	-2.22×10^{-6}	N/A
		Anaerobic	1×10^{-6}	-0.45	-3.2×10^{-7}	0.45	N/A	2.22×10^{-6}	3.13	-2.22×10^{-6}	N/A
	Reverse Warburg Tumor Cell	Aerobic, WN = 2	0.018	-0.183	-0.052	0.117	N/A	0.098	0.349	-0.154	N/A
		Aerobic, RW	0.018	-6.72×10^{-3}	-0.073	-0.079	N/A	2.68	0.247	0.227	N/A
		Hypoglycemic	1×10^{-6}	-3.73×10^{-7}	-0.053	-0.05	N/A	2.68	1.87×10^{-5}	2×10^{-5}	N/A
		Anaerobic	1×10^{-6}	-0.45	-3.2×10^{-7}	0.45	N/A	2.22×10^{-6}	3.13	-2.22×10^{-6}	N/A
Glutamine Addiction	Healthy Stromal Cell	Aerobic	1×10^{-6}	-0.045	-0.048	N/A	N/A	2.22×10^{-5}	2.08×10^{-5}	N/A	N/A
		Anaerobic	1×10^{-6}	-0.45	-3.2×10^{-7}	N/A	N/A	2.22×10^{-6}	3.13	N/A	N/A
	Glutamine-addicted Tumor Cell	Aerobic	0.018	-0.122	-0.059	N/A	-0.03	0.148	0.305	N/A	0.607
		Anaerobic	1×10^{-6}	-1.55×10^{-4}	-0.053	N/A	-0.054	6.46×10^{-3}	1.88×10^{-5}	N/A	1.86×10^{-5}

Table 3-1: Summary of uptake/production rates and yield coefficients of metabolites under different cellular metabolic phenotypes.

We simulate growth in both radial and axial geometries (**Fig. 3-1C**). The radial simulations (**Fig. 3-1C i**) provide a qualitative understanding of the growth dynamics in different metabolic scenarios; axial simulations (**Fig. 3-1C ii**) allow us to further quantify the observed dynamics. In both cases, we initiate tumor cell clones (same Monod parameters) surrounded by a varying number of layers of stromal cells (defined by distinct metabolic and growth parameters – see **Fig. 3-2** and **Table 3-1**). These arrangements capture tumor growth with initiation occurring at different distances from local vascular structure and thus at different levels of metabolic stress. We proceed to track growth as a function of depth of initiation and metabolic phenotype. We perform replicates with randomly seeded initial positions of tumor and stromal cells within their compartments. As we are interested in initial stages of avascular growth, we do not account for later stage processes such as angiogenesis. Further, we do not account for cell death explicitly in our simulations; tumor cells in zones with severely depleted metabolites remain quiescent based on the Monod-like growth kinetics. When evaluating total tumor size, this assumption is equivalent to counting dead cell mass within the necrotic core as part of the tumor; this definition is consistent with that of previous studies [41–45].

With the aim of providing intuition on the outcomes of simulations and characteristic physical parameters, we also calculate the Krogh length, shown schematically in **Fig. 3-1C iii**). Here, we define the Krogh length of a metabolite as the length at which the concentration of metabolite becomes zero given the uptake of the metabolite with zeroth order growth kinetics for the cell phenotype in the region (see Methods). While this is an extremely simple model that couples zeroth order kinetics with a continuum description of reaction and

diffusion in the tissue, we will show that it provides insights into the characteristics by which reaction and diffusion govern the growth of tumors.

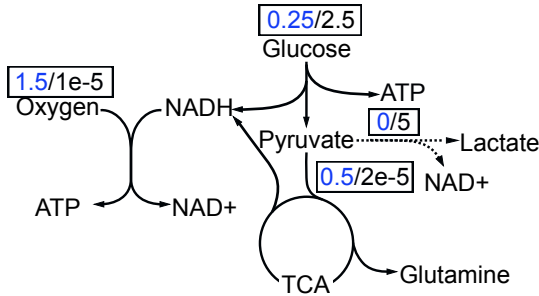
With this multi-scale computational framework, we study the tumor population dynamics in a spatial-temporal manner and investigate the consequences of different hypotheses in cancer metabolism from a population ecology perspective. This perspective examines the roles of phenotypic composition, spatial structure and reaction-diffusion on tumor growth.

3-2-2 Distinct metabolic profiles of various cells types implied by metabolic scenarios

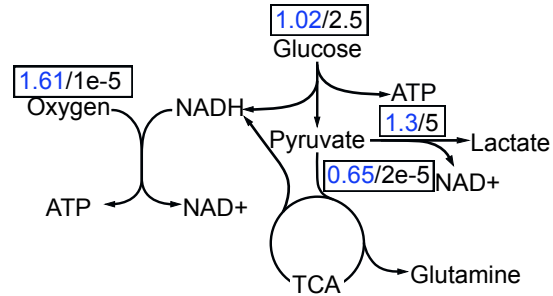
Before we further specify the hypotheses depicted in **Figure 3-1** individually, we define the metabolic phenotypes of the cell types implicated in these hypotheses based on observations in the literature. We integrate our interpretations of these metabolic mechanisms into FBA to obtain the uptake and production rates of metabolites (see **Table 3-1**): In our approach, we assume each cell type (e.g., healthy stromal cell) can adopt more than one metabolic phenotype (e.g., aerobic under normoxic conditions and anaerobic under hypoxic conditions). These different metabolic phenotypes are implemented as objective functions and constraints in FBA and in turn, result in different flux distributions (**Fig. 3-2**, coded by color). We then obtain yield coefficients ($Y_{i/n}$) for the i^{th} solute in the n^{th} metabolic phenotype of cells by linking maximum growth rate ($\mu_{m,n}$) of the m^{th} cell type to the uptake and production rates ($q_{i/n}$) (Equation 1 in **Fig. 3-1B**); the $Y_{i/n}$ serve as measures of the efficiency with which the metabolites generate biomass: the bigger the value of $Y_{i/n}$ is, the more efficiently the n^{th} metabolic phenotype utilizes the i^{th} metabolite to grow.

A Warburg effect

i) Stromal cell ●

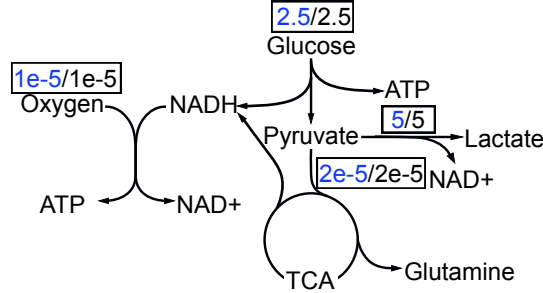


ii) Warburg tumor cell, WN = 2 ●

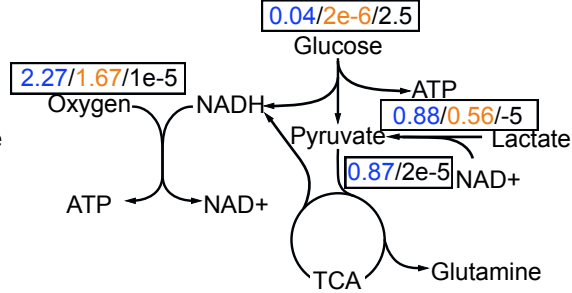


B Reverse Warburg effect

i) Hijacked stromal cell ●

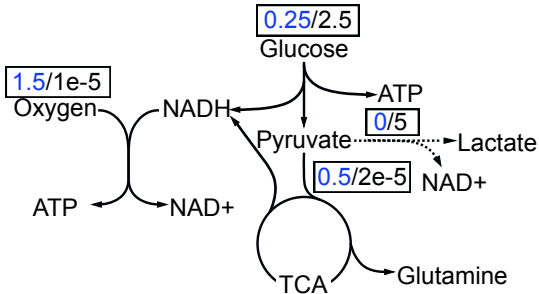


ii) Reverse Warburg tumor cell ●



C Glutamine addiction

i) Stromal cell ●



ii) Glutamine-addicted tumor cell ●

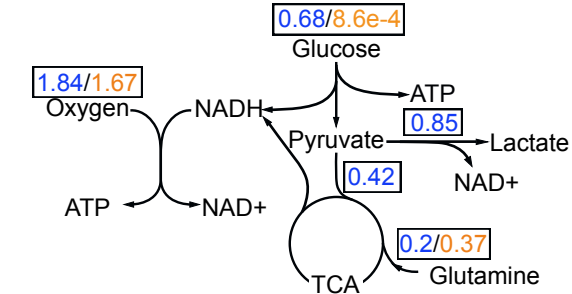


Figure 3-2: Metabolic profiles of various cell types in different hypotheses. Values of metabolic fluxes [mmol/g-DW-hr] under different metabolic phenotypes obtained from the FBA are shown in boxes. Green: normoxic phenotype. Orange: hypoglycemic phenotype. Black: hypoxic phenotype. (A) Representation of the Warburg Effect hypothesis includes: (i) Stromal cells: Normoxic stromal cells are quiescent and aerobic (use mainly OXPHOS to generate ATP for maintenance) (green values). Hypoxic stromal cells are quiescent and anaerobic (use primarily glycolysis to generate ATP for maintenance) (black values). (ii) Warburg tumor cells: Normoxic Warburg tumor cells are highly proliferative and aerobically

glycolytic (use mainly glycolysis to generate ATP to grow — green values). The values of flux shown represent the metabolic phenotype of Warburg Number, $WN = 2$. Hypoxic Warburg tumor cells are quiescent and anaerobically glycolytic (use glycolysis to generate ATP for maintenance — black values). **(B)** Representation of the Reverse Warburg Effect includes: (i) Hijacked stromal cells: Normoxic hijacked stromal cells are quiescent and undergo aerobic glycolysis (use mainly glycolysis to generate ATP for maintenance — green values). Hypoxic hijacked stromal cells are quiescent and anaerobic (use mainly glycolysis for maintenance — black values). (ii) Reverse Warburg tumor cells: Normoxic reverse Warburg tumor cells are highly proliferative and uptake lactate aerobically; however they utilize OXPHOS to generate ATP to grow fueled by lactate and oxygen instead of undergoing glycolysis with glucose (green values). Hypoglycemic reverse Warburg tumor cells are quiescent and consume lactate to fuel mitochondria for maintenance (orange values). Hypoxic reverse Warburg tumor cells are quiescent and undergo anaerobic glycolysis to produce lactate (black values). Note the different direction of arrows for lactate fluxes. **(C)** Representation of Glutamine Addiction includes: (i) Stromal cell: Normoxic stromal cell is quiescent and aerobic (use mainly OXPHOS to generate ATP for maintenance — green values). Hypoxic stromal cell is quiescent and anaerobic (use primarily glycolysis to generate ATP for maintenance — black values). (ii) “Glutamine-addicted” tumor cell: Normoxic “glutamine-addicted” tumor cells are highly proliferative and aerobic; instead of utilizing glucose in glycolysis, it undergoes OXPHOS to generate ATP to grow fueled by glutamine and oxygen (green values). Hypoglycemic “glutamine-addicted” tumor cells are quiescent and consumes glutamine to fuel mitochondria for maintenance (orange values). Hypoxic “glutamine-addicted” tumor cells do not consume glutamine. They are quiescent and undergo anaerobic glycolysis (black values). Note the different direction of arrow for glutamine flux.

Figure 3-2 summarizes predictions from FBA for the metabolic profiles of these cell types under distinct metabolic phenotypes. The metabolic switch from normoxia to hypoxia or to hypoglycemia leads to drastic changes in metabolic fluxes; the values in box represent fluxes of the specific metabolites when they display different metabolic profiles, coded by color (see caption). These flux distributions in turn lead to different use of metabolites as reflected in yield coefficients (presented in **Table 3-1**). We present detailed description of each phenotype of the cells in the following subsections.

3-2-2-1 The Warburg effect

In our exploration of the Warburg effect, we use healthy quiescent cells to define the tissue that hosts the tumor cells (**Figs. 3-2A i**) and **3-2C i**). We refer to these cells as stromal cells. This metabolic scenario imposes a direct competition for resources between the two sub-populations (stromal cells and tumor cells).

To define the metabolic character of stromal cells under normoxia at the intracellular scale with FBA, we set an objective function that targets an extremely low growth rate ($1 \times 10^{-6} \text{ hr}^{-1}$, equivalent to a doubling time of 28881 days) to represent the quiescent nature of healthy somatic cells (**Fig. 3-2A i**), green). Additionally, we put unconstrained bounds (0 to ∞) on all fluxes in the network.

To define the stromal metabolic phenotype at the cellular scale, we express the growth kinetics in terms with oxygen and glucose as the limiting metabolites. We choose a Monod form that captures the Pasteur effect:

$$\frac{dX_S}{dt} = \left(\mu_{S,aer} \frac{C_G}{K_G + C_G} \frac{C_O}{K_O + C_O} + \mu_{S,ana} \frac{C_G}{K_G + C_G} \frac{K_O}{K_O + C_O} \right) X_S \quad (5)$$

where X_S [g] is the biomass of the stromal cells, $m_{S,aer}$ [hr^{-1}] is the maximum growth rate under normoxia, $m_{S,ana}$ [hr^{-1}] is the maximum growth rate under hypoxia, C_G [g/L] is the concentration of glucose, K_G [g/L] is the half saturation constant for glucose, C_O [g/L] is the concentration of oxygen, and K_O [g/L] is the half saturation constant for oxygen. The Monod form in Equation 1 (**Fig. 3-1B**) approximates the behavior of a quiescent somatic cell whose growth is under regulatory control that follows Pasteur effect [46]: when oxygen concentration the cells experience is high ($C_O \gg K_O$), the first term on the right-hand side of Equation 5 dominates, simulating oxidative phosphorylation (OXPHOS); when oxygen concentration becomes low ($C_O \ll K_O$), the second term (Equation 5, right-hand side)

becomes dominant, capturing cells undergoing anaerobic glycolysis. We set the half saturation constants of the metabolites (except lactate, which is set to be the same as that of glucose) to be 1/10 of their physiological concentrations in blood circulation (See Table 3-2) with the assumption that cells would experience phenotypic change when concentrations of the limiting metabolites drop by an order of magnitude. Since we use the same maximum growth rates under normoxia and hypoxia ($m_{S,aer} = m_{S,ana} = 1 \times 10^{-6} \text{ hr}^{-1}$), Equation 5 can be further simplified to the following form:

$$\frac{dX_S}{dt} = \mu_S \frac{C_G}{K_G + C_G} X_S \quad (6)$$

Although this form indicates that the growth of stromal cells only depends on glucose availability, driven by the imposed weak growth rate, the FBA accounts for the demand for cellular maintenance under different cellular phenotypes (aerobic vs. anaerobic) such that the predicted yield coefficients for both O_2 and glucose depend strongly on local concentration of O_2 (**Table 3-1**). The different utilization of metabolites (represented by yield coefficients) under the influence of O_2 availability in turn impacts local concentrations of both O_2 and glucose, and thus leads to different growth rate of cells.

To define the character of a Warburg tumor cells under normoxia (**Fig. 3-2A i**), green), we used the ratio of the flux of pyruvate to lactate to its flux into the mitochondrion; we call this ratio the Warburg number (WN). A literature survey suggested that a typical value of the WN in tumor cells is 2 (two pyruvates go to lactate for every one that enters the TCA cycle), though significant uncertainty remains and WN may be as large as ~ 10 [15,47,48]. In this study, we explore a range of WN in our simulations, from 0 to 34.

To define the Warburg phenotype at the intracellular scale in FBA, we chose the objective function to achieve a growth rate of 0.018 hr^{-1} (doubling time = 38 hrs), a typical doubling rate for cancer cells [47,48]. We then iteratively changed the uptake rate of oxygen to achieve a desired WN. This iterative process was done by setting the upper bound of the constraint on the oxygen uptake rate to be the same as that of the unconstrained FBA solution (the case of $\text{WN} = 0$) and then lowering it in each iteration until the desired WN was reached. This constraint on oxygen forced the uptake of more glucose and led to production of lactate (① in **Fig. 3-1A**, green in **Fig. 3-2A ii**). Without this imposed constraint, our flux distribution did not display the characteristics of the Warburg effect (i.e., there was no lactate production such that $\text{WN} = 0$); an observation also made previously [21,49]. We found that a constraint directly imposed on lactate production could also be used to produce the same flux distribution predicted with constrained oxygen uptake. The equivalence of these two constraints is due to the requirement of ATP and redox balance to meet the growth demand; this balance can only be achieved via either OXPHOS or aerobic glycolysis [9,11]. As illustrated in **Fig. 3-2A ii** ($\text{WN} = 2$), when a Warburg phenotype is imposed ($\text{WN} > 0$), the metabolic behavior of tumor cells under normoxia (green) is very distinct from the Pasteur behavior of the healthy stromal cells (**Fig. 3-2A i**), as tumor cells undergo aerobic glycolysis. The Warburg phenotype under normoxia forces tumor cells to use glycolysis in addition to OXPHOS for ATP generation; this situation leads to a shift in utilization from oxygen to glucose, reflected in uptake rates of glucose ($q_{\text{Glu/aer}} = -0.078 \text{ g/g-DW-hr}$ for $\text{WN} = 0$ vs. $q_{\text{Glu/aer}} = -0.183 \text{ g/g-DW-hr}$ for $\text{WN} = 2$) as well, shown in **Table 3-1**.

To define the Warburg phenotype at the cellular scale, we select a Monod form of growth kinetics that captures a Pasteur-like switch from rapid growth in normoxic conditions

(aerobic growth, $m_{W,aer} = 0.018 \text{ hr}^{-1}$) to slow growth under hypoxic conditions (anaerobic growth, $m_{W,ana} = 1 \times 10^{-6} \text{ hr}^{-1}$):

$$\frac{dX_W}{dt} = \left(\mu_{W,aer} \frac{C_G}{K_G + C_G} \frac{C_O}{K_O + C_O} + \mu_{W,ana} \frac{C_G}{K_G + C_G} \frac{K_O}{K_O + C_O} \right) X_W \quad (7)$$

where X_W [g] is the biomass of the tumor cell, C_G [g/L] is the concentration of glucose, K_G [g/L] is the half saturation constant for glucose, C_O [g/L] is the concentration of oxygen, and K_O [g/L] is the half saturation constant for oxygen (**Table 3-1**).

3-2-2-2 *The reverse Warburg effect*

In the reverse Warburg hypothesis, oxidative tumor cells have been observed to uptake lactate as a carbon source in addition to glucose (**Fig 3-1A**, ②) [22,23,50].

Additionally, up-regulation of glycolytic enzymes such as PKM2 has been observed in tumor-associated fibroblast suggesting an aerobic glycolytic phenotype for tumor-associated stromal cells [12,51]. This metabolic scenario represents an example of a host-parasite effect in which the hijacked stromal cells (the “host”) are feeding the tumor cells (the “parasite”) lactate by adopting an aerobic glycolytic phenotype [52]. This type of behavior between the oxidative and hypoxic tumor cells as well as between the tumor cells and the stromal cells has also been previously referred to as a symbiosis [14,16,24,25,29,53].

In the exploration of the reverse Warburg hypothesis, we used the “hijacked” stromal cells described by Sotgia et al. to define the tissue in which tumor grows [54]. These metabolically reprogrammed stromal cells can be tumor-associated fibroblasts or macrophages. Unlike the quiescent healthy stromal cells that undergo the Pasteur effect, they commit to a glycolytic phenotype in which they uptake glucose and produce lactate under both normoxic (green in **Fig. 3-2B i**) and hypoxic (black in **Fig. 3-2B i**) conditions.

To capture the metabolic phenotype of aerobic glycolysis in hijacked stromal cells under normoxic conditions in FBA, we used an objective function to minimize oxygen uptake rate while constraining the cell at a low growth rate, m_{HS} ($1 \times 10^{-6} \text{ hr}^{-1}$, same as for healthy stromal cells). Hence, the metabolic flux distributions are identical in normoxic and hypoxic conditions, as shown in **Fig. 3-2B i**).

We define the biomass growth of such reprogrammed stromal cells at the cellular scale as follows:

$$\frac{dX_{HS}}{dt} = \mu_{HS} \frac{C_G}{K_G + C_G} X_{HS} \quad (8)$$

where X_{HS} [g] is the biomass of the tumor cell, C_G [g/L] is the concentration of glucose, and K_G [g/L] is the half saturation constant for glucose (**Table 3-1**). As with healthy stromal cells, this Monod form is also independent of oxygen. However, in this case, we follow the proposal by Sotgia et al. that these reprogrammed stromal cells are committed to a glycolytic phenotype that favors the use of oxygen and lactate by the adjacent Reverse Warburg tumor cells. Therefore, the yield coefficients of O_2 and glucose for the hijacked stromal cells remain the same under both normoxia and hypoxia (**Table 3-1**).

To investigate the hypothesis of reverse Warburg effect, we define the normoxic reverse Warburg phenotype of tumor cells at the intracellular scale in FBA by using an objective function to minimize the uptake of glucose to simulate the ability to utilize lactate as the preferred substrate by the tumor cells while constraining the growth rate, $m_{RW,aer}$, to be high under normoxic conditions (0.018 hr^{-1} as with the Warburg phenotype) (green in **Fig. 3-2B ii**).

At the cellular scale, based on our interpretation of the reverse Warburg tumor cells from the literature [12,16,23], we allowed them to adapt to different metabolic phenotypes in response to changes in local concentration of metabolites (i.e., lactate, glucose and oxygen), captured by the Monod-like growth kinetics. Specifically, in addition to the normoxic Warburg and hypoxic phenotypes (**Fig. 3-2A ii**), we introduced two more metabolic phenotypes, the normoxic reverse Warburg (green in **Fig. 3-2B ii**) and hypoglycemic phenotypes (orange in **Fig. 3-2B ii**) to describe the reverse Warburg tumor cells:

$$\frac{dX_{RW}}{dt} = \mu_{RW,aer} \frac{C_G}{K_G+C_G} \frac{C_L}{K_L+C_L} \frac{C_O}{K_O+C_O} + \mu_{W,aer} \frac{C_G}{K_G+C_G} \frac{K_L}{K_L+C_L} \frac{C_O}{K_O+C_O} + \mu_{hypogly} \frac{C_L}{K_L+C_L} \frac{C_O}{K_O+C_O} \frac{K_G}{K_G+C_G} + \mu_{RW,ana} \frac{C_G}{K_G+C_G} \frac{K_O}{K_O+C_O} X_{RW} \quad (9)$$

where X_{RW} [g] is the biomass of the stromal cells, $m_{W,aer}$ [hr^{-1}] is the maximum growth rate of the Warburg phenotype under normoxia, $m_{hypogly}$ [hr^{-1}] is the maximum growth rate under hypoglycemia, and $m_{RW,ana}$ [hr^{-1}] is the maximum growth rate under hypoxia; C_G , C_O , and C_L [g/L] are the concentrations of glucose, oxygen and lactate, and K_G , K_O and K_L [g/L] are the half saturation constant for glucose, oxygen and lactate (**Table 3-1**).

Equation 9 encodes the following characteristics of our interpretation of the reverse Warburg hypothesis: 1) when lactate is abundant ($C_L \gg K_L$), the tumor cells preferably uptake lactate over glucose and undergo OXPHOS aided by oxygen to grow under normoxia (green in **Fig. 3-2B ii**), normoxic reverse Warburg phenotype, term 1 in Equation 9, aerobic growth, $m_{RW,aer} = 0.018 \text{ hr}^{-1}$). 2) When lactate is limited ($C_L \ll K_L$), we allow the tumor cells under the hypothesis of reverse Warburg effect to revert back to the Warburg phenotype described above and grow by taking up glucose while producing lactate (term 2 in Equation 9, aerobic growth, $m_{W,aer} = 0.018 \text{ hr}^{-1}$). We note that due to the equality in the maximum growth rates in both Reverse Warburg and Warburg phenotypes, term 1 and 2 in Equation 9

can be combined leading to an independence of lactate in the aerobic growth conditions. 3) When glucose is limiting, we allow the tumor cells to stay quiescent (orange in **Fig. 3-2B ii**), hypoglycemic phenotype, term 3 in Equation 9, $m_{hypogly} = 1 \times 10^{-6} \text{ hr}^{-1}$) by having lactate and oxygen generate the energy necessary for cell maintenance. We achieve this hypoglycemic metabolic phenotype by imposing the same objective function and constraints as the reverse Warburg phenotype in FBA but at a growth rate, $m_{hypogly} = 1 \times 10^{-6} \text{ hr}^{-1}$ (see Methods). 4) The reverse Warburg tumor cells are also sensitive to local oxygen concentration. When oxygen becomes limiting, they utilize glucose in anaerobic fermentation to stay quiescent ((black in **Fig. 3-2B ii**)), hypoxic phenotype, term 4 in Equation 9, $m_{RW,ana} = 1 \times 10^{-6} \text{ hr}^{-1}$), same as the Warburg tumor cell, and healthy stromal cells under hypoxic conditions (also see Methods).

3-2-2-3 *Glutamine addiction*

Glutamine addiction has emerged as one of the most acknowledged hypotheses in the field of cancer metabolism [6]: Although glutamine addiction is not observed in all tumor cells, the community has started to recognize the role of glutamine in growth as a hallmark of metabolic rewiring in cancer [6,13,55,56]. Numerous studies reported that tumor cells consume glutamine via glutaminolysis to feed their tricarboxylic acid (TCA) cycle, a process termed anaplerosis (**Fig. 3-1A**). In this study, we aim to explore specifically the role of glutamine in anaplerosis by considering glutamine as an alternative substrate for glucose-derived carbon in the mitochondria of tumor cells. Here, we make a simplified assumption that the growth of tumor cells is hindered under glucose deprivation due to the dependence on upstream glycolysis and Pentose Phosphate Pathways, capturing a coupled utilization of glucose and glutamine in cancer metabolism [55]. Following this assumption, we model glutamine-addicted tumor cells that cannot survive on glutamine as the sole carbon source,

consistent with the behavior of Myc-positive tumor cells [57,58]. Since the Warburg effect and glutamine addiction are not mutually exclusive hypotheses [59], we created the glutamine-addicted tumor cells by adding the dependence of glutamine to the previously defined Warburg phenotype of tumor cells (with a WN of 2). Hence, glutamine-addicted tumor cells utilize both glucose and glutamine as non-equivalent carbon sources to grow, with glutamine used in anaplerosis only.

To define the glutamine-addicted phenotype of tumor cells, at the intracellular level with FBA, in addition to the constraints that result in a WN of 2, we also constrained the network such that the ratio of glutamine to glucose uptake rates was 3 to 10 as observed experimentally [48]. This specific constraint forces the FBA network to uptake glutamine as a carbon source that would not occur autonomously. Specifically, we set the growth rate to be 0.018 hr^{-1} , increased the upper bound of the constraint on glucose while decreasing the upper bound of the constraint on oxygen and sought for a value for glutamine uptake by changing the upper bound of the constraint on glutamine that allowed the ratio of fluxes of glutamine to glucose to be 3 to 10 and $\text{WN} = 2$ (green in **Fig. 3-2C ii**). As in the treatment of Reverse Warburg tumor cells, we allow the glutamine-addicted tumor cells to remain quiescent under hypoglycemic conditions by having both glutamine and oxygen fuel their mitochondria to generate the energy necessary for cell maintenance (orange in **Fig. 3-2C ii**). We achieve this hypoglycemic metabolic phenotype by setting the objective function to minimize glucose uptake rate while constraining the growth rate at $1 \times 10^{-6} \text{ hr}^{-1}$ as well as allowing uptake of glutamine (also see Methods). We note that due to the requirement of oxygen for the utilization of glutamine in energy production, growth of glutamine-

addicted tumor cells under hypoxia depends on the oxygen. Hence, we describe the growth kinetics of glutamine-addicted tumor cells at the cellular scale as follows:

$$\frac{dX_{GA}}{dt} = \left(\mu_{GA,aer} \frac{C_G}{K_G+C_G} \frac{C_N}{K_N+C_N} \frac{C_O}{K_O+C_O} + \mu_{hypogly} \frac{C_N}{K_N+C_N} \frac{C_O}{K_O+C_O} \frac{K_G}{K_G+C_G} \right) X_{GA} \quad (10)$$

where N refers to glutamine, $m_{GA,aer}$ [hr^{-1}] is the maximum growth rate of the glutamine-addicted phenotype under normoxia, $m_{hypogly}$ [hr^{-1}] is the maximum growth rate under hypoglycemic conditions, C_N [g/L] is the concentration of glutamine and K_N [g/L] is the half saturation constant of glutamine (**Table 3-1**).

Again, we used healthy quiescent cells to define the tissue that hosts the tumor cells (**Fig. 3-2A i**) and **3-2C i**).

3-3 Results

3-3-1 Radial simulations

To gain a qualitative understanding of the impact of the various metabolic scenarios on tumor growth in a diffusion-limited microenvironment, we first ran simulations in an unconstrained 2-D domain, as shown in **Fig. 3-1C i**); metabolites were delivered through a diffusive boundary layer of fixed thickness that surrounds the growing tissue (see Methods). **Figure 3-3** presents the form of the tumors at initiation ($t = 0$) and after 100 days of growth for Warburg tumor cells with healthy stromal cells ($WN = 2$ – top row), Reverse Warburg cells with hijacked stromal cells (middle row), and glutamine-addicted tumor cells with healthy stromal cells (bottom row). The three columns are for initial seeding of tumor cells beneath 1, 3, and 5 layers of stromal cells, as indicated in the images of the initial configuration of the cells ($t = 0$). As the number of layers of stromal cells increased, the growth of tumor cells became compromised due to the reduced access to the metabolites. By hindering diffusion and consuming oxygen and glucose, the stromal cells decrease the

accessibility of these metabolites to the tumor cells. In all cases, we note that the proliferation of the tumor cells led to their breaking through the layers of stromal cells; for the cases with significant growth, the stromal cells became engulfed within the tumor, as is frequently observed in actual tumors [60]. We also note the emergence of irregular front of the tumor in the scenario of reverse Warburg effect. We suspect that this irregularity arises from growth instability due to the moderate availability of metabolites at the growth front [35]. We note qualitatively different effects of the addition of layers of stromal cells on tumor growth for the different scenarios: with 5 layers of stromal cells, the growth of both Warburg and Glutamine-addicted tumor cells was strongly delayed, whereas the impact on the growth of Reverse Warburg cells was modest. These observations motivate a deeper investigation of the mechanisms that control response to metabolic stress in these scenarios.

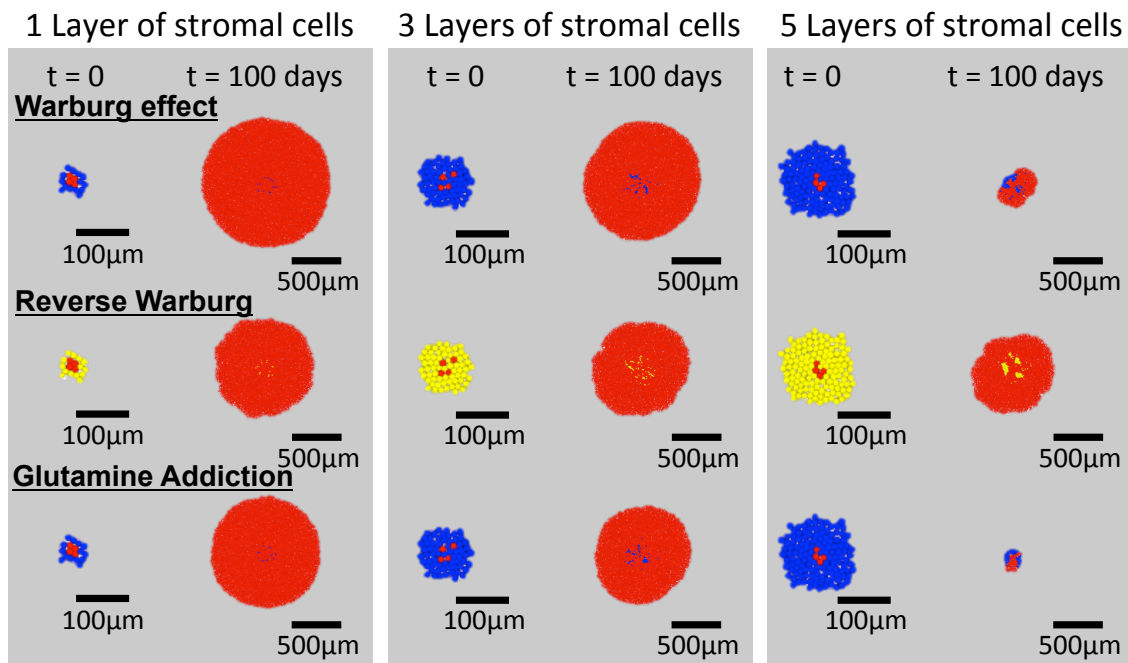


Figure 3-3: Distribution of cells in radial simulations. Initial conditions ($t = 0$) and end points ($t = 100$ days) are shown for the three hypotheses with cells seeded initially with 1, 3 and 5 layers of stromal cells surrounding the tumor cells.

3-3-2 Impact of reaction-diffusion on tumor growth

We proceeded to dissect the metabolic scenarios further with simulations in a confined geometry in which solute diffusion and tissue expansion were constrained along a single direction, as shown in **Figure 3-1C ii**). This axial scenario approximates the local environment adjacent to a blood vessel (upper boundary). **Figure 3-4** presents an overview of the growth behavior in this geometry. For this overview, we simulated the Warburg scenario, with Warburg tumor cells ($WN = 2$) and healthy stromal cells (also see **Fig. 3-2**).

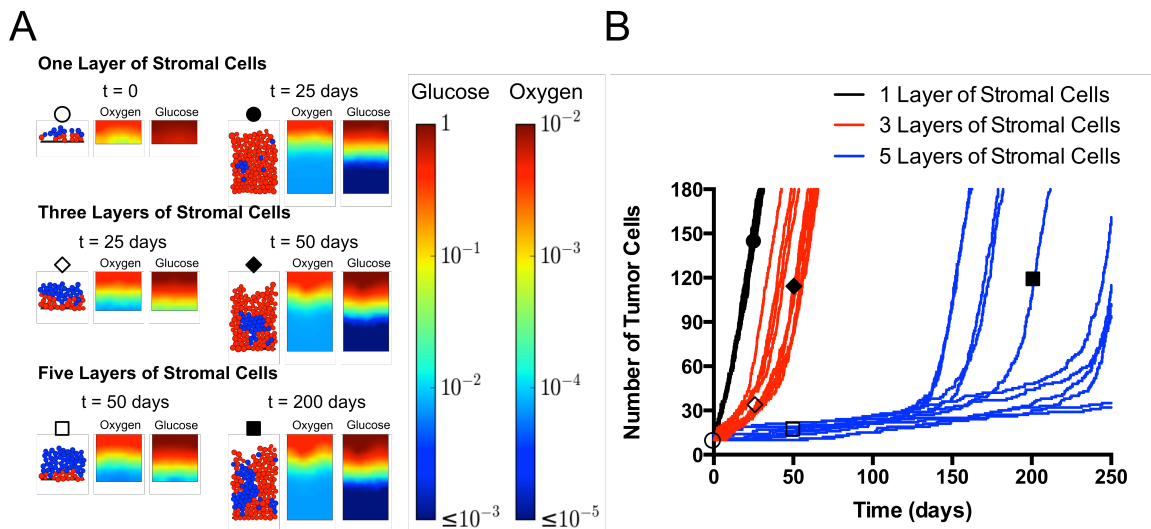


Figure 3-4: Axial agent-based model of growth of Warburg tumor cells in a perivascular tissue. (A) Snapshots of predicted cellular structure and concentration fields of metabolites at different times. Tumor cells with 1, 3, and 5 of layers of healthy stromal cells separating them from the source of nutrients (top, representing interface with blood). Color bars present concentrations of oxygen and glucose in g/L. **(B)** Growth trajectories of tumor cells from simulations in three cases in (A). For each case, the trajectories for 11 independent simulations are shown. Initial positions of cells were randomly generated within the corresponding stromal or tumor compartment (see Methods). \circ : one layer of stroma; time = 0 day. \bullet : one layer of stroma, $t = 25$ days. \diamond : three layers of stroma; $t = 25$ days. \blacklozenge : three layers of stroma; $t = 50$ days. \square : five layers of stroma; time = 50 days. \blacksquare : five layer of stroma; $t = 200$ days.

Figure 3-4A shows the snapshots of tumor growth and the corresponding concentration fields of oxygen and glucose at various time-points for tumors initiated beneath

1, 3, and 5 layers of stromal cells. In the colormaps of the concentration fields, we see that when the tumor initiated closer to the source (top row with 1 layer of stromal cells), the Warburg tumor cells had access to ample oxygen and glucose to fuel their growth at early time ($t = 0$, \circ); at late times ($t = 25$ days, \bullet), significant depletion of both oxygen and glucose occurred, but the uppermost layer of tumor cells still benefited from high metabolite concentrations to grow. However, when the tumor initiated farther away from the source (middle and bottom rows), the diffusion limitations and consumption by the stromal cells limited the metabolites available to the tumor cells, even at early times (\diamond , \square). This limitation persisted until the tumor cells broke through the stromal layer and gained access to higher concentrations of metabolites (\blacklozenge , \blacksquare).

Figure 3-4B presents the trajectories of tumor growth from 11 simulation runs in each case shown in **Figure 3-4A**. We first note that for all initial conditions, the growth appears to proceed through two phases, starting with slower growth that then transitions to faster growth; these two regimes are most evident for 3 and 5 layers of stromal cells. By observing the cellular configurations in the simulations, we identify that the transition occurs when the tumor cells break through the layers of stromal cells and gain access to high concentrations of metabolites. When the tumor cells started to grow, the reaction-diffusion in the intact layers of stromal cells limited the supply of metabolites to the tumor cells. Under such conditions, the growth of tumor cells was significantly compromised due to the lack of oxygen (note the more severe depletion of oxygen relative to glucose in **Figure 3-4A**, also see Equation 7 in Model); the microtumor was nearly quiescent. Once this slow growth led to the penetration of one or more tumor cells through the layers of stromal cells, those tumor cells transitioned toward their aerobic growth regime (term 1 in Equation 7) and quickly

overwhelmed the stroma. Interestingly, the growth rates after breakthrough were constant (the growth curves are linear in time) and independent of initial conditions (all late time slopes are the same in **Fig. 3-4B**). This constant growth rate is distinct from the exponential growth that one would expect resulting from saturating Monod-like growth kinetics (Equations 5 - 9 in Model). This observation illustrates an important consequence of a diffusively limited microenvironment. We will comment further on the origin of this constant rate below.

In the case of 1 layer of stromal cells (black curves), the growth transitions rapidly (within the first days) to a high, constant rate. Furthermore, the trajectories of all the random initial seeding conditions are very similar. For 3 and 5 layers of stromal cells (blue and red curves), the first, slow phase lasts longer because the tumor cells experienced more severe limitations in their initial configurations. Additionally, in these cases, the trajectories of different initial conditions diverge strongly from one another due to the differences in the moment of transition from slow to fast growth. This observation reflects the fact that the time for tumor cells to break through the stroma is sensitive to small differences in the initial configuration of cells.

3-3-3 Fitness conferred by metabolic scenarios

We now proceed to use axial simulations like those in **Figures 3-1C ii)** and **3-4** to investigate the growth dynamics in each of the three metabolic scenarios.

3-3-3-1 The Warburg effect

In order to investigate the impact of the strength of Warburg effect on tumor growth in a resource-limited microenvironment, **Figure 3-5** presents growth in the axial simulation (as in **Fig. 3-4**) run with tumor cells that display various levels of the Warburg effect, as

defined by the value of the Warburg Number ($WN = 0, 2, 10, 34$). Although all four different metabolic phenotypes of tumor cells grow at the same maximum growth rate under aerobic growth regime, due to different flux distribution of metabolites, tumor cells with higher WN have higher yield coefficients of oxygen and lower yield coefficients of glucose, as shown in **Table 3-1**.

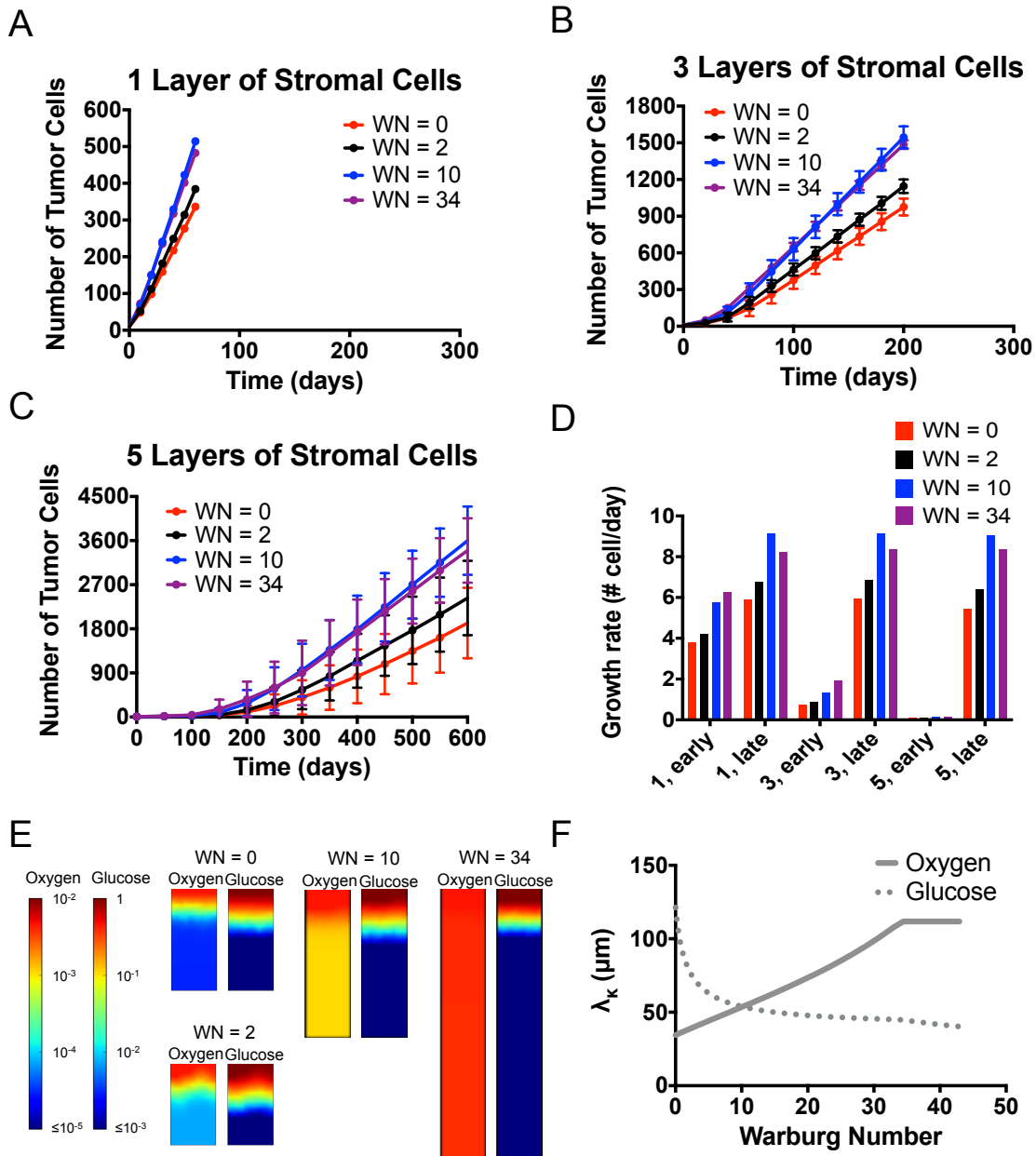


Figure 3-5: Warburg tumor cells. (A-C) Comparisons of growth curves from axial simulations as in **Figure 3-4A** for Warburg tumor cells with Warburg Number, $WN = 0$

(Control), 2, 10, and 34 with 1, 3 and 5 layers of stromal cells on top. Each time point represents the average of 11 simulations; error bars represent standard deviation. Note differences in vertical scales on plots. **(D)** Comparison of growth rate of tumor cells at early and late times (see Methods), extracted from the average growth curves in (A-C). **(E)** Concentration fields of metabolites in the case of five layers of stroma at $t = 150$ days. **(F)** Krogh lengths of oxygen and glucose based on consumption of tumor cells vs. Warburg Number. Solid line: Oxygen. Dotted line: Glucose.

Figures 3-5A-C present the comparison of growth curves of tumor cells with three different thicknesses of stromal cells (**Fig. 3-4**; circle: 1 layer of stromal cells; diamond: 3 layers of stromal cells; square: 5 layers of stromal cells). We first note that the two-phase growth regime is present for 3 and 5 layers of stromal cells across all four metabolic tumor phenotypes (**Figs. 3-5B** and **3-5C**). As before, the late-time rates are constant (linear growth curves). We note that the rate of late-stage growth increases with increasing WN up to $WN = 10$, before saturating or decreasing slightly ($WN = 34$).

To further quantify both early- and late-stage growths across these scenarios, **Figure 5D** presents growth rates extracted from the average curves in **Figures 3-5A-C** (see Methods). In the cases of 1 and 3 layers of stromal cells at early times (**Fig. 3-5D**, “1, early”, “3, early”), we observe that higher WN leads to faster growth. This observation suggests that when tumor cells experience moderate to high concentrations of metabolites near the blood vessels, the higher yields on oxygen at higher WNs provide a growth advantage. However, this trend is not obvious in the early-time growth rate of tumor cells in the case of 5 layers of stromal cells: the growth rates increase monotonically with WN, such that breakthrough occurs earlier for the more glycolytic cells ($WN = 34$, see **Fig. 3-4C**). The late-time growth rates (**Fig. 3-5D**, “late”) represent the cell growth after breaking through layers of stromal cells, when the outer most tumor cells have direct access to high

concentrations of both oxygen and glucose regardless of the initial number of layers of stromal cells; these growth rates are a strong function of WN. Distinct from the early time behavior, the late-time growth rate of tumor cells is non-monotonic in WN: it rises from 0 to a maximum at $WN = 10$ before falling again at $WN = 34$.

To understand this non-monotonic dependence on WN, **Figure 3-5E** presents the late-time concentration fields of metabolites for the case of 5 layers of stromal cells. These distributions show that the depletion of oxygen becomes significantly less severe as WN increases due to the increase in yield coefficients on oxygen (**Table 3-1**). More subtly, the depletion of glucose increases with increasing WN. We further calculated the Krogh lengths of metabolites based on tumor cell consumptions to provide insights into the predictions of growth rate from simulations at late times. **Figure 3-5F** shows the changes in Krogh lengths of oxygen (solid curve) and glucose (dotted curve) as WN increases. At low WN, the Krogh length of oxygen is smaller, indicating that the growth of tumor cells is mainly limited by the availability of oxygen. As WN increases, the Krogh length of oxygen increases (with increasing yield coefficient) whereas Krogh length of glucose decreases, and the two cross at $WN \cong 10$. At higher WNs, growth is glucose-limited and the growth rate decreases with the decreasing Krogh length for glucose, as observed in the simulations (**Fig. 3-5D** – “late”). Interestingly, this observation suggests that tumor cells may have optimal growth fitness at intermediate WN.

The observations of the late-time concentration fields in **Figure 3-5E** and the consideration of Krogh lengths allow us to explain the constant, late-time growth rates that we have noted above. The depletion of metabolites (oxygen and glucose) over a fixed distance within the growing tumor means that only cells within this peripheral zone (i.e.,

within a Krogh length of the source) grow while cells deeper within the tissue are essentially quiescent. A fixed number of cells growing at a constant rate leads to the constant growth of the tumor, in contrast to the more familiar scenario in which a homogeneous population grows exponentially with individual cell growing at a fixed rate. Our model thus captures and explains an important characteristic of solid tumor growth that has been observed experimentally [61,62].

3-3-3-2 The reverse Warburg effect

To study the population-scale effects of the reverse Warburg effect under resource limitations, we performed agent-based simulations by seeding hijacked stromal cells (Fig. 3-2B i) and the reverse Warburg tumor cells (Fig. 3-2B ii) in the axial geometry (Figs. 3-1C ii) and 3-4A).

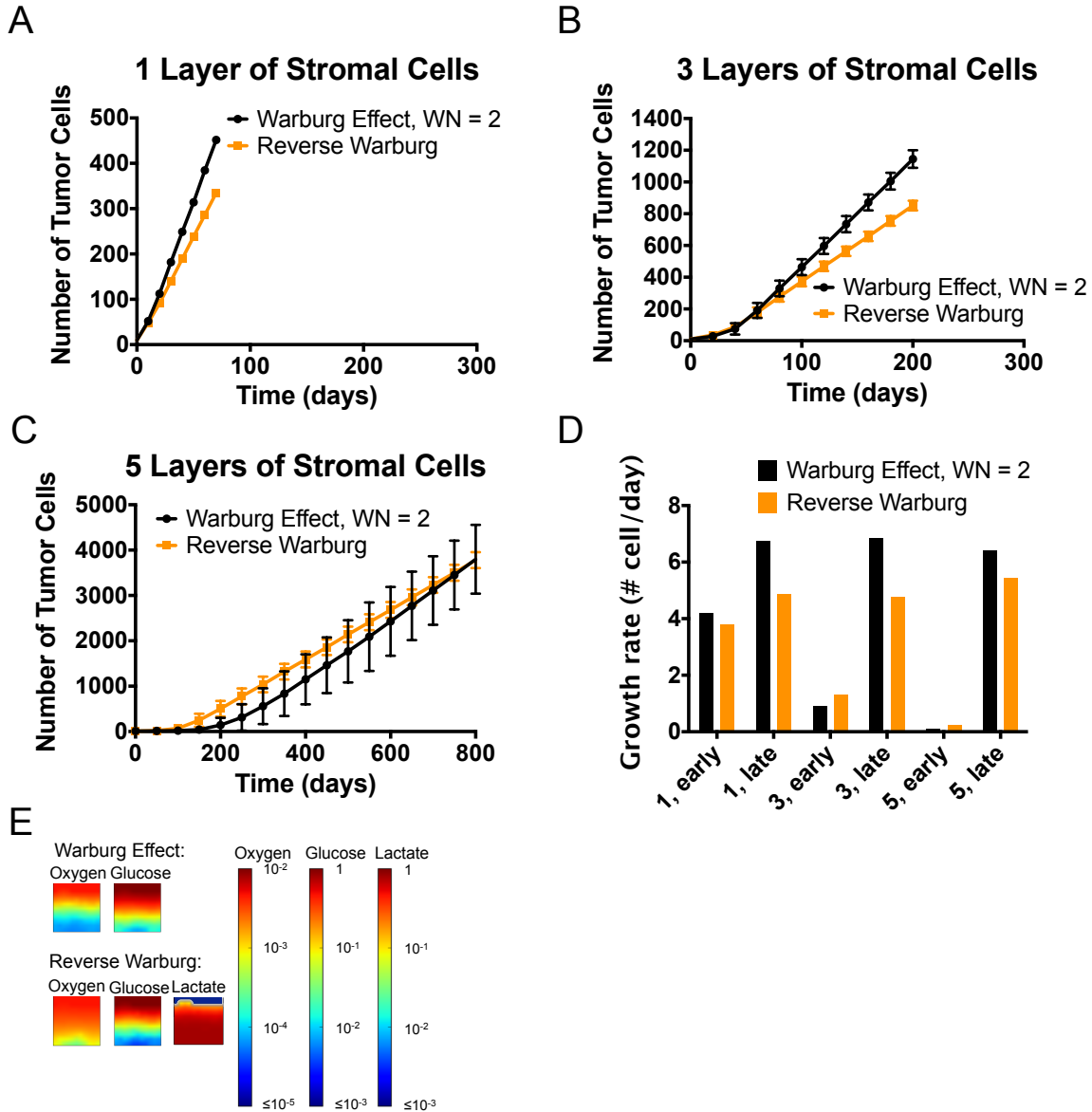


Figure 3-6: Reverse Warburg Effect: (A-C) Comparison of growth curves from axial simulations of tumor cells between the Warburg effect (WN = 2) and Reverse Warburg effect when one, three and five layers of hijacked stromal cells are seeded between the source and

tumor cells. Each time point represents the average of 11 simulations; error bars represent standard deviation. Note differences in vertical scales on plots. **(D)** Comparison of growth rate of tumor cells at early and late times, extracted from average growth curves in (A-C). **(E)** Concentration field of metabolites in the case of five layers of stromal cells at $t = 0$.

Figures 3-6A-C present the comparison of the growth curves of reverse Warburg tumor cells with their hijacked stromal cells (orange) to that of Warburg tumor cells with healthy stromal cells ($WN = 2$; black; same as black curves in **Figs. 3-5A-C**) with 1, 3, and 5 layers of stromal cells. Again, we observe two phases of growth, as in **Figures 3-4B** and **3-5A-C**. As we concluded previously, the two stages of growth correspond to the pre- and post-breakthrough of tumor cells. For 1 layer of stromal cells (**Fig. 3-6A**), it appears that Warburg tumor cells grew faster in both regimes. On the other hand, for 3 and 5 layers of stromal cells (**Figs. 3-6B** and **3-6C**), reverse Warburg tumor cells grew faster at early times when they were buried beneath the layers of hijacked stromal cells (i.e., pre-breakthrough), whereas Warburg tumor cells grew faster in the second regime, once breakthrough had occurred.

To investigate these distinctions further, we present the growth rates of tumor cells under these two metabolic scenarios at early and late times in **Figure 3-6D**. At early times, we confirm that Warburg tumor cells grew faster than reverse Warburg tumor cells in the case of 1 layer of stromal cells. In this case, the availability of metabolites in tumor-cell compartment was not significantly compromised by diffusion limitations and the consumption by the stromal cells; both phenotypes adopted the aerobic growth regime. According to Equations 5 and 7, both phenotypes of tumor cells depend on both oxygen and glucose to grow under aerobic conditions. Looking at the yield coefficients on oxygen and glucose shown in **Table 3-1**, we can see that reverse Warburg tumor cells have slightly lower yields on oxygen ($Y_{O_2/aer} = 0.247$ g-DW/g for the reverse Warburg phenotype vs. $Y_{O_2/aer} =$

0.349 g-DW/g for the Warburg phenotype, $WN = 2$) and much higher yields on glucose ($Y_{\text{Glu/aer}} = 2.68$ g-DW/g for the reverse Warburg phenotype vs. $Y_{\text{Glu/aer}} = 0.098$ for the Warburg phenotype, $WN = 2$). This lower yield on oxygen is a cost of using lactate instead of glucose in the TCA cycle (which in turn affects the ATP production in OXPHOS), underlining the fact that lactate is not an equivalent carbon source to glucose for tumor cells. Therefore, within a favorable metabolic environment (e.g., 1 layer of stromal cells), Warburg tumor cells grew faster due to their better yields on oxygen. Further, upon breaking through the layer of stroma, they obtained direct access to higher concentrations of metabolites, and their growth advantage was amplified, as is reflected in the larger disparity in growth rates at all late times (**Fig. 3-6D**).

As number of layers of stromal cells increases, the initial tumor growth is more strongly affected by the consumption of metabolites by the stromal cells. This impact is reflected in the opposite trend present in growth rates at early times in the case of 3 and 5 layers of stromal cells (**Fig. 3-6D**, “3, early”, “5, early”): reverse Warburg tumor cells grew faster than Warburg tumor cells in these cases. We attribute this early-time growth advantage in reverse Warburg tumor cells to the reduced consumption of oxygen by hijacked stromal cells (due to their higher yields on oxygen than healthy stromal cells, **Table 3-1**); this effect represents a host (hijacked stromal cells) –parasite (reverse Warburg tumor cells) interaction between the two sub-populations.

We present in **Figure 3-6E** the concentration fields of metabolites at $t = 0$ in the case of 5 layers of stromal cells. At the initial stage of tumor growth, we note that oxygen penetrated deeper into the tissue in the reverse Warburg scenario. Although a large number of stromal cells were present, their adoption of aerobically glycolytic phenotype allowed

them to use glucose to generate ATP while producing lactate and allowing oxygen to diffuse into the tumor cell compartment; this penetration of oxygen allowed the reverse Warburg tumor cells to grow aerobically and thus faster such that they reached breakthrough more quickly (**Fig. 3-6C**). After breakthrough, due to the lower yields of biomass on oxygen for reverse Warburg tumor cells, the Warburg tumor cells grew faster and eventually outgrew the reverse Warburg tumor cells (**Figs. 3-6C-D**).

These observations suggest that the host-parasite relationship between hijacked stromal cells and tumor cells that characterized the reverse Warburg effect can provide growth advantage to tumors that initiate farther away from blood vessels [12], but that this advantage may not persist after the tumor has escaped from its initial, resource-limited environment.

3-3-3-3 *Glutamine addiction*

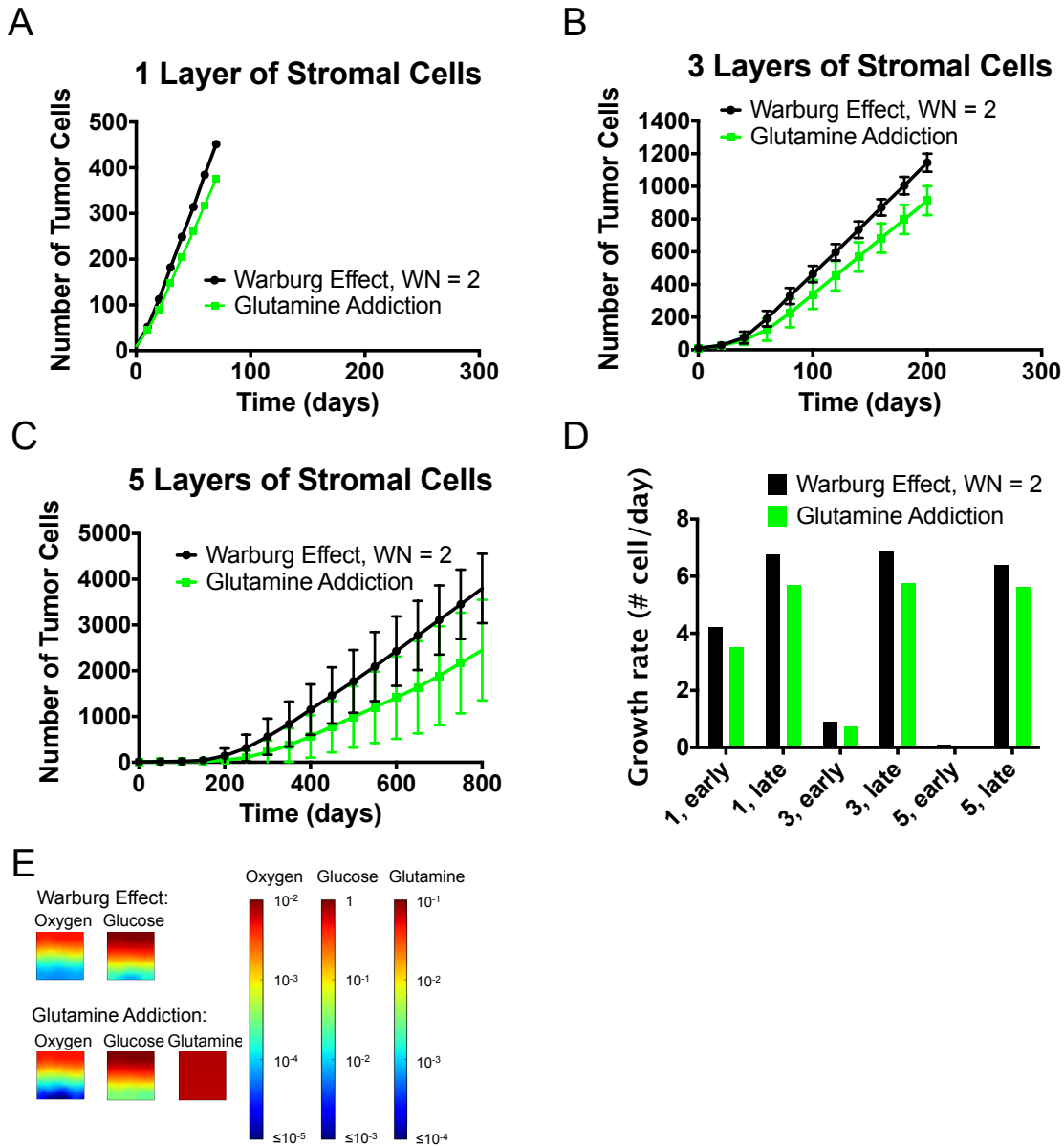


Figure 3-7: Glutamine Addiction: (A - C) Comparison of growth curves from axial simulations of tumor cells between the Warburg effect and Glutamine addiction when one, three and five layers of stromal cells is imposed in between the source and tumor cells, respectively. Note differences in vertical scales on plots. Each time point represents the average of 11 simulations; error bars represent standard deviation. (D) Comparison of growth rate of tumor cells at early and late times (see Methods). (E) Concentration field of metabolites in the case of five layers of stromal cells at $t = 0$.

Figures 3-7A-C present the comparison of tumor growth between Warburg tumor (with $WN = 2$) cells and glutamine-addicted tumor cells. The growth curves of Warburg tumor cells rise above the ones of glutamine-addicted tumor cells in all three cases, indicating a growth advantage in the Warburg scenario. This growth advantage of the Warburg tumor cells increased as tumor cells initiated more deeply in the tissue (from 1 layer (**Fig. 3-7A**) to 5 layers (**Fig. 3-7C**) of stromal cells). This observation can be explained as follow: from FBA results shown in **Table 3-1**, the use of glutamine by glutamine-addicted tumor cells allows them to uptake much less glucose (higher yields on glucose at 0.148) compared to Warburg tumor cells (lower yields on glucose at 0.098) under aerobic growth regime. However, the required uptake rate of oxygen for glutamine-addicted tumor cells is higher (lower yield coefficient on oxygen at 0.305 vs. 0.349 for Warburg tumor cells in **Table 3-1**). This lower yield on oxygen occurs because glutamine passes as α -ketoglutarate via glutamate into the TCA cycle to produce biomass precursors; this pathway leads to lower demand for glucose in the TCA cycle. Subsequently, due to the constraint of $WN = 2$, there is less lactate production and hence less regeneration of NADH from this pathway. Therefore, more oxygen is required to maintain the redox balance in glutamine-addicted tumor cells. As seen in **Figure 3-7D**, the higher demand of oxygen by glutamine-addicted tumor cells led to lower growth rates at both the early and late times and for all initial conditions. Additionally, as illustrated in **Figure 3-7E**, even in the case of 5 layers of stromal cells, glutamine was never limiting. We attribute this abundance of glutamine to the growth of stromal cells being independent of glutamine and the initiation site of glutamine-addicted tumor cells being oxygen depleted. We conclude that oxygen and glucose remain the limiting metabolites in this metabolic scenario.

Based on our assumptions and results, we infer that for a typical value of $WN = 2$, the role of glutamine in anaplerosis does not confer improved fitness to tumor population relative to Warburg effect in a geometrically confined microenvironment. Therefore, unless glutamine-addicted tumor cells utilize oxygen at a similar efficiency as Warburg tumor cells, for example by adopting a metabolic phenotype with higher Warburg Number than Warburg tumor cells (e.g., being Myc-positive may allow tumor cells to have even higher glycolytic rate [59]), the experimentally observed glutamine addiction in diverse tumor cell types cannot be explained by its role in supplying carbon to the TCA cycle for population-scale growth advantage. Therefore, we speculate that some other biological role of glutamine, not included in the current model, must underlie this phenomenon.

3-4 Discussion

3-4-1 Warburg effect improves tumor fitness in resource-limited microenvironment

Within our scope of study of the Warburg effect through the multi-scale modeling approach (Figs. 3-4 and 3-5), we confirmed a common hypothesis that Warburg effect impacts tumor cell fitness in metabolically limited microenvironments [63]. Interestingly, our predictions suggest that there may exist an optimal level of Warburg effect (reflected by the ratio of pyruvate fluxes to lactate and to the TCA cycle; the Warburg Number) for tumor cells to adopt depending on the details of the metabolic microenvironment in which the tumor cells initiate. This observation may help explain the experimentally observed phenotypic heterogeneity in cancer metabolism [64,65]. Such adaptation could occur via modification of the fluxes of pyruvate, for example with changes in enzymatic rates along either the TCA cycle or glycolytic pathways. From an ecological perspective, our predictions

indicate that the Warburg effect may provide a basis for adaptation of tumor cells to different environmental metabolic stresses [66].

3-4-2 Reverse Warburg effect provides tumor growth advantage depending on the initial microenvironment

For the reverse Warburg effect scenario (**Fig. 3-6**), we provide the first mathematical description of the multi-cellular metabolic interactions proposed by Sotgia et al. [54]. We used our framework to explore the intracellular and multicellular consequences of reverse Warburg effect due to the interaction between glycolytic stromal cells (hijacked stromal cells) and lactate-consuming tumor cells (reverse Warburg tumor cells). We predict that the hijacked stromal cells have higher yields on oxygen than healthy stromal cells (**Fig. 3-2B i** and **Table 3-1**). This information confirmed the intuitive proposal of Sotgia et al. that the hijacked stromal cells assist in the growth of tumors that initiate deep within the stroma by allowing more oxygen to penetrate into the tumor compartment (**Figs. 3-6C-E**). We further note that, due to the adaptive character of reverse Warburg tumor cells, they are not sensitive to local lactate concentration in aerobic growth regimes (terms 1 and 2 on the right-hand side of Equation 9 can be combined); this characteristic means their aerobic growth remains limited by oxygen and glucose only. Additionally, due to the utilization of lactate as carbon source in energy production in these tumor cells, their yield on oxygen is lower compared to tumor cells in the scenario of the Warburg effect (requiring more oxygen for the same mole of carbon consumed). Therefore, the reverse Warburg effect leads to slower growth in favorable metabolic microenvironments (i.e., abundant source of metabolites available). However, when tumors initiate in microenvironments where resources are significantly reduced, the host-parasite relationship implied by the reverse Warburg effect (via cooperative

utilization of oxygen between hijacked stromal cells and tumor cells) can provide a growth advantage to tumors. Given that such growth advantage depends on the detailed structure of the metabolic microenvironment, we suggest that one must use a multi-scale framework like the one presented here to investigate the implications of these metabolic scenarios.

3-4-3 Glutamine addiction as a hallmark of cancer metabolism

In the exploration of glutamine addiction (**Fig. 3-7**), we defined the metabolic phenotype by hypothesizing that glutamine addiction coexists with the Warburg effect. This hypothesis led us to propose a coupled contribution to biomass synthesis of tumor cells from glucose and glutamine as joint carbon sources. Specifically, we aimed to explore the role of glutamine in anaplerosis (as a carbon source to replenish the TCA cycle). We demonstrated with FBA that under our interpretation, glutamine addiction led to an increase uptake of oxygen (i.e., lower yield on oxygen) in glutamine-addicted tumor cells to maintain their redox balance and to meet the energy demand; this lower yield on oxygen represents a cost of using glutamine in the TCA cycle. We see the impact of this lower yield on oxygen in the reduced growth rate of glutamine-addicted tumor cells relative to Warburg tumor cells. We thereby conclude that glutamine addiction via the process of anaplerosis does not confer an advantage to the overall tumor growth primarily due to the strong dependence on oxygen. We argue that glutamine is not an effective alternative carbon source because tumor cells remain limited by glucose and oxygen.

Our study constrains future considerations of the roles of glutamine addiction in tumor growth by clearly demonstrating that the anaplerotic pathway cannot, alone, provide a growth advantage to tumors. With our focus on the anaplerotic role of glutamine using a simplified metabolic network, we did not account for other roles of glutamine in cellular

demand explicitly [67,68]. For example, glutamine is known to be an important nitrogen source in nucleic acids and amino acids synthesis [56,69,70]. Additionally, glutamine contributes to the pool of metabolites that maintains NADPH/NADP⁺ balance [68,71] and to produce glutathione as an antioxidant to help the cell resist oxidative stress during rapid metabolism [69,71]. We conclude that a more detailed investigation that accounts for the multi-scale implications of these additional pathways is needed in the future.

3-4-4 Multi-scale modeling framework

With our approach, the growth curves captured in our spatially resolved model (a slow growth regime followed by a fast unidirectional linear growth) are compatible with the experimentally observed growth of avascular solid tumor [62,72]. Previous studies attributed the linear growth regime observed at late-time tumor growth to available space for growth and cell diffusion at the edge of the tumors [72,73]. Here, our simulations and analysis indicate that this effect can be entirely explained by diffusion limitations of metabolites.

In our exploration of the Warburg and reverse Warburg effects, our approach provided a basis for exploring the heterogeneity in metabolic phenotypes that has been suggested by recent experiments [64,65]. For example, the crossover of growth rates that we observed from early to late times (**Figs. 3-5C** and **3-6C**) suggests that adaptation of metabolic phenotypes (e.g., from high to intermediate WN or from RW to Warburg) could improve overall growth potential of tumors.

In parallel with experimental approach, computational tools allow for high throughput investigation of hypotheses that are emerging rapidly in the field of cancer study [24,29,33,34,67,74,75]. Particularly, a multi-scale modeling framework such as the one presented here can provide a basis for predicting cell-level to tissue-scale response to

therapeutic interventions. For example, the action of inhibitors of key regulators of cellular metabolism such as PI3K [76] can be accounted for in FBA and propagated through to the tissue-scale ABM in our framework.

We finish by emphasizing that our interpretations of the three metabolic scenarios studied here are not unique either with respect to the choices of constraints and objectives imposed for FBA or the details of the cellular configurations within our simulations. Our modeling framework can accommodate a large diversity of hypotheses and should serve as a powerful tool with which to evaluate emerging ideas and experimental observations from the rapidly evolving field of cancer metabolism.

3-5 *Methods*

3-5-1 Intracellular – Modeling biomass production using a stoichiometric model

To capture the intracellular details of different metabolic phenotypes of cells, we adopt the well-established framework of FBA.

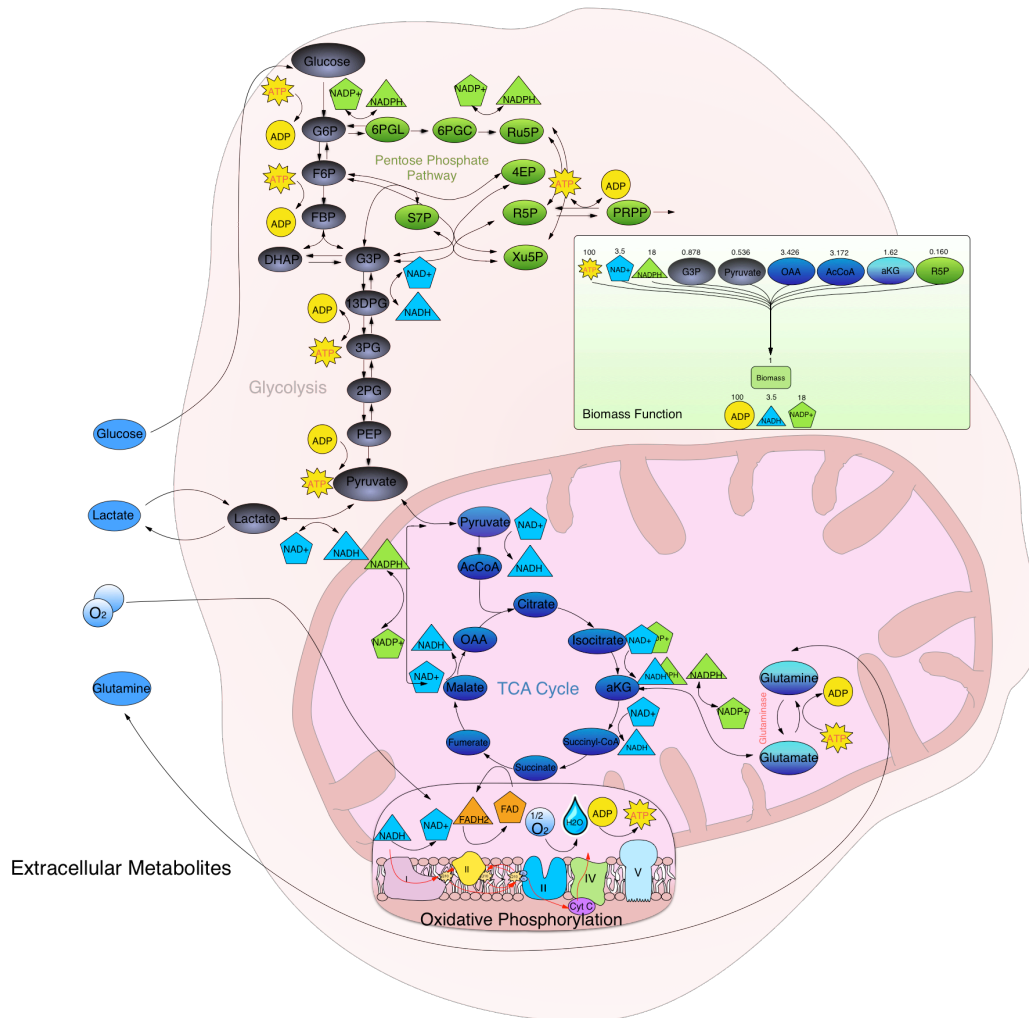


Figure 3-8: Full mammalian central metabolic network used in flux balance analysis.

In our study, the central carbon metabolism of human was constructed with 140 reactions and 92 metabolites (**Fig. 3-8**). Of those 140 reactions, 34 consist of boundary exchange of metabolites such as uptake and secretion, 26 consist of mitochondrial exchange of metabolites with the cytosol, 1 is the biomass template reaction, 1 reaction for maintenance, and the 78 remaining reactions are transformations of metabolites that occur in the cytosol and mitochondrion. The biomass template reaction for growth in the human model was adapted from the Shlomi *et al.*'s genome-scale model [21]. Shlomi *et al.*'s

biomass template reaction consists of 30 biomass compounds including amino acids (0.78 g/g-DW), nucleotides (0.06 g/g-DW), and lipids (0.16 g/g-DW). These biomass requirements were combined and reduced to their upstream precursors for simplification in our biomass template reaction. For example, stoichiometric equivalence of ribose-5-phosphate, the precursor of nucleic acids, was used in place of nucleotides in their final form. For the maintenance rate, we first sampled a range of values [77,78] and concluded that the overall qualitative trend of our FBA results was not affected by this choice. Therefore, for simplicity, a maintenance rate of 5 mmol/g-DW-hr is used consistently for all cell types. Using our reduced biomass function, our glucose yields ($Y_{G/n}$) matched closely with that of Shlomi and coworkers [21]. For example, within the metabolic phenotype of $WN = 0$, the yield coefficient (specific growth rate per glucose) of our reduced order model (0.0984 g-DW/mmol) was within 4% Shlomi et al's genome scale model (0.095 g-DW/mmol).

3-5-2 Metabolic phenotypes in hypoxic and hypoglycemic conditions

Under hypoxic conditions ($C_O < K_O$), we assumed a quiescent phenotype for all cell types. To capture the hypoxic condition, we minimized the oxygen uptake rate while maintaining a growth rate of $1 \times 10^{-6} \text{ hr}^{-1}$ to represent the quiescent state.

For tumor cells in the metabolic scenarios of reverse Warburg effect and glutamine addiction, we used a quiescent phenotype for tumor cells under hypoglycemic conditions ($C_G < K_G$). We achieve this condition in FBA by minimizing glucose uptake while allowing uptake of lactate or glutamine respectively and constraining growth rate to be $1 \times 10^{-6} \text{ hr}^{-1}$.

3-5-3 Use of agent-based simulation tool at multicellular scale — iDynoMiCS

iDynoMiCS is an individual-based modeling platform originally built for the study of microbial biofilms [17]. It allows computation of diffusion-reaction kinetics at individual cell level and has multiple built-in kinetic mechanisms, including Monod forms as in Equation 5-9. Additionally, iDynoMiCS treats the cell movement through two mechanisms: displacements due to pressure-induced convection at the global scale based on Darcy’s law, and sterically induced displacements that avoid overlapping during the expansion and division of neighboring cells at a local scale. During a simulation, the pressure that is directly proportional to the rate of biomass generation or degradation is computed first to induce global convection, followed by the computation of “shoving” (random displacement) at local scale; these displacements are selected by a relaxation algorithm to avoid steric overlap. The shoving mechanism is propagated through all cells until the number of cells that are still moving is negligible, and leads to local random displacements of cells [17].

Parameter	Description	Value	Units	Reference
D_{O_2}	Diffusion coefficient of oxygen	3.11×10^{-4}	m^2/day	MacDougall and McCabe, 1967
D_{Glu}	Diffusion coefficient of glucose	2.16×10^{-5}	m^2/day	Bashkatov, Genina and Tuchin, 2009
D_{Lac}	Diffusion coefficient of lactate	2.5×10^{-5}	m^2/hr	
D_{Gln}	Diffusion coefficient of glutamine	2.32×10^{-5}	m^2/hr	
K_O	Half saturation constant of oxygen	4.6×10^{-4}	g/L	see text
K_G	Half saturation constant of glucose	0.1	g/L	see text
K_L	Half saturation constant of lactate	0.1	g/L	see text
K_N	Half saturation constant of glutamine	7.3×10^{-3}	g/L	see text
S_O	Physiological concentration of oxygen	4.6×10^{-3}	g/L	based on Henry’s law at 37 °C and 100 mmHg
S_G	Physiological concentration of glucose	1	g/L	
S_L	Physiological concentration of lactate	0	g/L	
S_N	Physiological concentration of glutamine	7.3×10^{-2}	g/L	
ρ	dry mass density of the cell	2000	g/L	based on 3.5 ng/cell of which 30% is dry mass and radius of 10 μm
h	Boundary layer thickness in iDynoMiCS	15	μm	

Table 3-2: Summary of simulation parameters.

In our case, since we are explicitly interested in studying how diffusion-reaction kinetics impact the tumor growth under various hypotheses on cancer metabolism with no specific consideration of molecular guidance for cell movements, the random, local cell

motion provided by iDynoMiCS serves as a reasonable approximation of cell dynamics within the tissue [79]. The 2-D simulation domain is discretized into a square grid on which the reaction-diffusion equation is solved by finite difference at each time step (Equations 2 in **Fig. 3-1** and Equation 4). The domain is also divided into two compartments: the “tank” and the “biofilm”. The tank serves as the source of metabolites; we interpret this compartment to be the blood stream with which the tissue exchanges nutrients. The “biofilm” defines the tissue where the metabolites undergo diffusion and reaction; the local reaction rate for each metabolite is set by the density and metabolic character of the cells in the grid element. A boundary layer defines the resistant to diffusive mass transfer between the blood stream (“tank”) and the cells (“biofilm”). In our axial simulations, we allowed the exchange of metabolites only at the top of the domain by having zero-flux boundary condition at the bottom of the domain and periodic boundary conditions on the sides and in the 3rd dimension (**Fig. 3-9**). We set the concentrations of metabolites in the “tank” at their physiological concentrations in human blood stream (**Table 3-2**). We selected a grid size for solving reaction-diffusion process to match individual mammalian cell size (~10 μm) and a boundary layer thickness, h , to represent the thickness of the vascular endothelium (**Table 3-2**). The size of the cell was used to determine the density of the cell based on dry cell mass (**Table 3-2**) With the density of the cell fixed, we calculated the spherical volume of the cell from biomass growth by conservation of mass. This volume was then used to calculate the diameter of cells at each time step. The calculated diameter at each time step was then used to compare to a threshold value to determine the division of the cell. Once the computational domain was defined, we then specified the reactions that govern the cell growth. In each reaction, we chose parameters such as half saturation constant (**Table 3-2**). Together with

parameters such as diffusion coefficients and physiological concentrations of metabolites obtained from the literature, we checked that the calculated value of the Krogh length (e.g., ~40mm for oxygen) was in the right range for mammalian tissue.

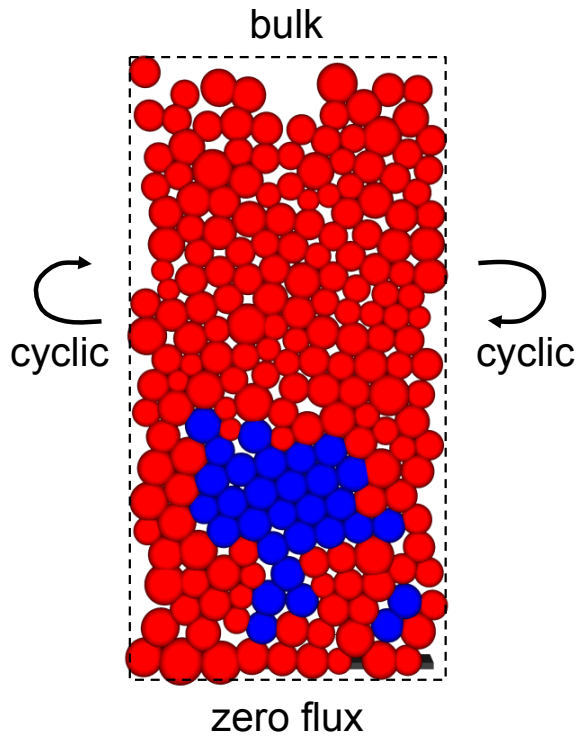


Figure 3-9: Boundary conditions in axial simulations.

3-5-4 Calculation of Krogh length

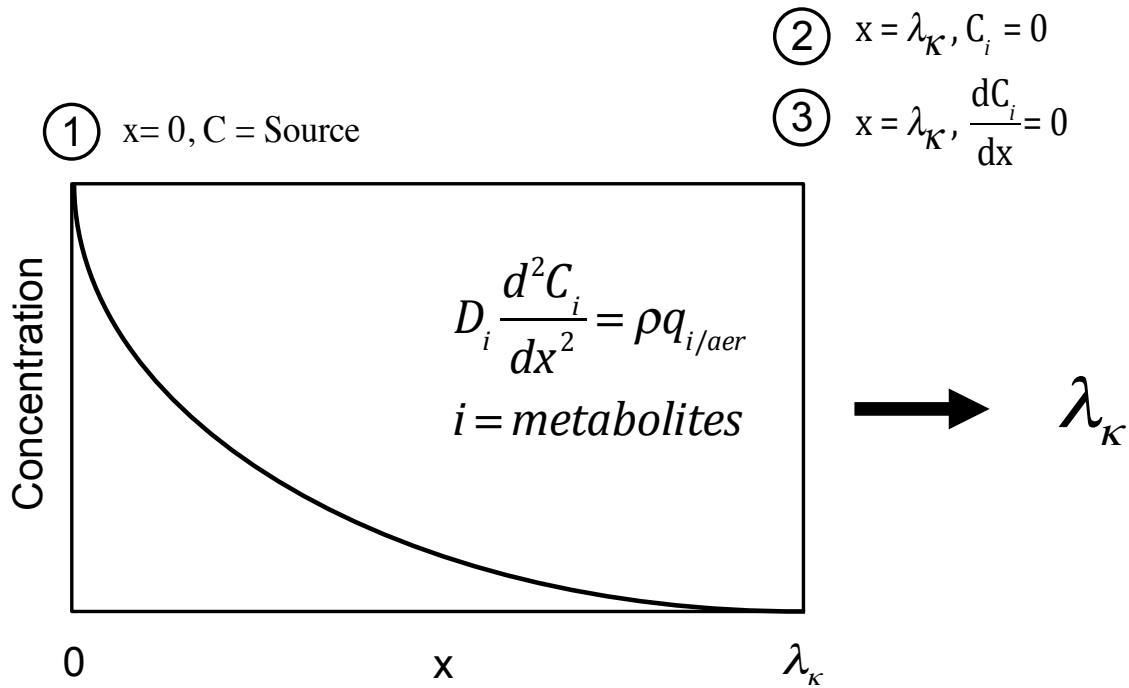


Figure 3-10: Calculation of Krogh lengths based on diffusion and zeroth order consumption by tumor cells.

In the calculation of Krogh lengths, we treat the tissue as a continuum and represent consumption of oxygen and glucose as being zeroth order within the steady state reaction-diffusion equation. We calculated the Krogh lengths to determine the limiting metabolite in tumor cell growth in different metabolic scenarios (i.e., different WNs, **Fig. 3-5F**). The Krogh lengths represent the typical depth of penetration of metabolites into the tumor compartment. We omitted the consumption contributed by anaerobic growth of the cells by assuming the metabolites get completely depleted before the cells switch to anaerobic growth regime. The calculation of Krogh lengths is illustrated in **Figure 3-10**. The metabolite with shorter Krogh length will play a more significant role in determining the growth dynamics of tumor cells.

3-5-5 Extraction of early- and late-time tumor growth rates

In **Figures 3-5 -7**, we evaluated early-time growth rates as the initial slope of the growth curves by taking the difference of the averaged number of tumor cells for the first two outputs of simulation and dividing by the time interval. The time intervals are 10 days, 20 days and 50 days for the cases of 1, 3 and 5 layers of stromal cells for all three metabolic scenarios.

Late-time growth rates were obtained in a similar fashion but evaluated at different time intervals due to the difference in breakthrough times in different cases. A growth over 30 days between the time points 30 and 60 days was used in the case of 1 layer of stromal cells. A growth over 80 days between the time points of 120 and 200 days was used for calculation of late-time growth rates in the cases of 3 layers of stromal cells. A growth over 200 days between the time points of 400 and 600 days was applied to the calculation of late-time growth rates in the cases of 5 layers of stromal cells. These choices of time ranges were applied consistently in all three metabolic scenarios.

3-6 References

- [1] N.E. Sounni, A. Noel, Targeting the Tumor Microenvironment for Cancer Therapy, *Clin. Chem.* 59 (2013) 85–93. doi:10.1373/clinchem.2012.185363.
- [2] A. Albini, M.B. Sporn, The tumour microenvironment as a target for chemoprevention., *Nat. Rev. Cancer.* 7 (2007) 139–47. doi:10.1038/nrc2067.
- [3] L. Galluzzi, O. Kepp, M.G. Vander Heiden, G. Kroemer, Metabolic targets for cancer therapy., *Nat. Rev. Drug Discov.* 12 (2013) 829–46. doi:10.1038/nrd4145.
- [4] D. Hanahan, R. a Weinberg, Hallmarks of cancer: the next generation., *Cell.* 144 (2011) 646–74. doi:10.1016/j.cell.2011.02.013.

- [5] J.H. Brown, J.F. Gillooly, A.P. Allen, V.M. Savage, G.B. West, TOWARD A METABOLIC THEORY OF ECOLOGY, *Ecology*. 85 (2004) 1771–1789. doi:10.1890/03-9000.
- [6] N.N. Pavlova, C.B. Thompson, The Emerging Hallmarks of Cancer Metabolism, *Cell Metab.* 23 (2016) 27–47. doi:10.1016/j.cmet.2015.12.006.
- [7] B. a. Teicher, W.M. Linehan, L.J. Helman, Targeting cancer metabolism, *Clin. Cancer Res.* 18 (2012) 5537–5545. doi:10.1158/1078-0432.CCR-12-2587.
- [8] P.P. Hsu, D.M. Sabatini, Cancer cell metabolism: Warburg and beyond, *Cell*. 134 (2008) 703–707. doi:10.1016/j.cell.2008.08.021.
- [9] M.G. Vander Heiden, L.C. Cantley, C.B. Thompson, Understanding the Warburg effect: the metabolic requirements of cell proliferation., *Science*. 324 (2009) 1029–1033. doi:10.1126/science.1160809.
- [10] R. a Cairns, I.S. Harris, T.W. Mak, Regulation of cancer cell metabolism., *Nat. Rev. Cancer*. 11 (2011) 85–95. doi:10.1038/nrc2981.
- [11] S.Y. Lunt, M.G. Vander Heiden, Aerobic Glycolysis: Meeting the Metabolic Requirements of Cell Proliferation, *Annu. Rev. Cell Dev. Biol.* 27 (2011) 441–464. doi:10.1146/annurev-cellbio-092910-154237.
- [12] S. Pavlides, D. Whitaker-Menezes, R. Castello-Cros, N. Flomenberg, A.K. Witkiewicz, P.G. Frank, M.C. Casimiro, C. Wang, P. Fortina, S. Addya, R.G. Pestell, U.E. Martinez-Outschoorn, F. Sotgia, M.P. Lisanti, The reverse Warburg effect: Aerobic glycolysis in cancer associated fibroblasts and the tumor stroma, *Cell Cycle*. 8 (2009) 3984–4001. doi:10.4161/cc.8.23.10238.
- [13] D.R. Wise, C.B. Thompson, Glutamine addiction: a new therapeutic target in cancer,

- Trends Biochem. Sci. 35 (2010) 427–433. doi:10.1016/j.tibs.2010.05.003.
- [14] O. Feron, Pyruvate into lactate and back: From the Warburg effect to symbiotic energy fuel exchange in cancer cells, *Radiother. Oncol.* 92 (2009) 329–333. doi:10.1016/j.radonc.2009.06.025.
- [15] O. Warburg, F. Wind, E. Negelein, THE METABOLISM OF TUMORS IN THE BODY., *J. Gen. Physiol.* 8 (1927) 519–30. <http://www.pubmedcentral.nih.gov/articlerender.fcgi?artid=2140820&tool=pmcentrez&rendertype=abstract> (accessed January 8, 2015).
- [16] E.C. Nakajima, B. Van Houten, Metabolic symbiosis in cancer: Refocusing the Warburg lens, *Mol. Carcinog.* 52 (2013) 329–337. doi:10.1002/mc.21863.
- [17] L.A. Lardon, B. V Merkey, S. Martins, A. Dötsch, C. Picioreanu, J.-U. Kreft, B.F. Smets, iDynamoCS: next-generation individual-based modelling of biofilms., *Environ. Microbiol.* 13 (2011) 2416–34. doi:10.1111/j.1462-2920.2011.02414.x.
- [18] J.W. Locasale, L.C. Cantley, Metabolic flux and the regulation of mammalian cell growth, *Cell Metab.* 14 (2011) 443–451. doi:10.1016/j.cmet.2011.07.014.
- [19] G.M. DeNicola, L.C. Cantley, Cancer’s Fuel Choice: New Flavors for a Picky Eater, *Mol. Cell.* 60 (2015) 514–523. doi:10.1016/j.molcel.2015.10.018.
- [20] J. Hu, J.W. Locasale, J.H. Bielas, J. O’Sullivan, K. Sheahan, L.C. Cantley, M.G. Vander Heiden, D. Vitkup, Heterogeneity of tumor-induced gene expression changes in the human metabolic network., *Nat. Biotechnol.* 31 (2013) 522–9. doi:10.1038/nbt.2530.
- [21] T. Shlomi, T. Benyamini, E. Gottlieb, R. Sharan, E. Ruppin, Genome-scale metabolic modeling elucidates the role of proliferative adaptation in causing the warburg effect,

- PLoS Comput. Biol. 7 (2011) 1–8. doi:10.1371/journal.pcbi.1002018.
- [22] P. Sonveaux, F. Végran, T. Schroeder, M.C. Wergin, J. Verrax, Z.N. Rabbani, C.J. De Saedeleer, K.M. Kennedy, C. Diepart, B.F. Jordan, M.J. Kelley, B. Gallez, M.L. Wahl, O. Feron, M.W. Dewhirst, Targeting lactate-fueled respiration selectively kills hypoxic tumor cells in mice, *J. Clin. Invest.* 118 (2008) 3930–3942. doi:10.1172/JCI36843.
- [23] N. Draoui, O. Feron, Lactate shuttles at a glance: from physiological paradigms to anti-cancer treatments, *Dis. Model. Mech.* 4 (2011) 727–732. doi:10.1242/dmm.007724.
- [24] J.B. Mcgillen, C.J. Kelly, A. Martínez-González, N.K. Martin, E. a Gaffney, P.K. Maini, V.M. Pérez-García, Glucose-lactate metabolic cooperation in cancer: insights from a spatial mathematical model and implications for targeted therapy., *J. Theor. Biol.* 361 (2014) 190–203. doi:10.1016/j.jtbi.2014.09.018.
- [25] B. Mendoza-Juez, A. Martínez-González, G.F. Calvo, V.M. Pérez-García, A Mathematical Model for the Glucose-Lactate Metabolism of in Vitro Cancer Cells, *Bull. Math. Biol.* 74 (2012) 1125–1142. doi:10.1007/s11538-011-9711-z.
- [26] A. a. Shestov, B. Barker, Z. Gu, J.W. Locasale, Computational approaches for understanding energy metabolism, *Wiley Interdiscip. Rev. Syst. Biol. Med.* 5 (2013) 733–750. doi:10.1002/wsbm.1238.
- [27] C. Carmona-Fontaine, V. Bucci, L. Akkari, M. Deforet, J. a Joyce, J.B. Xavier, Emergence of spatial structure in the tumor microenvironment due to the Warburg effect., *Proc. Natl. Acad. Sci. U. S. A.* 110 (2013) 19402–7. doi:10.1073/pnas.1311939110.

- [28] S. Astanin, L. Preziosi, Mathematical modelling of the Warburg effect in tumour cords, *J. Theor. Biol.* 258 (2009) 578–590. doi:10.1016/j.jtbi.2009.01.034.
- [29] C. Phipps, H. Molavian, M. Kohandel, A microscale mathematical model for metabolic symbiosis : Investigating the effects of metabolic inhibition on ATP turnover in tumors, *J. Theor. Biol.* 366 (2015) 103–114. doi:10.1016/j.jtbi.2014.11.016.
- [30] M. Archetti, D. a Ferraro, G. Christofori, Heterogeneity for IGF-II production maintained by public goods dynamics in neuroendocrine pancreatic cancer, *Proc Natl Acad Sci U S A.* 112 (2015) 1–6. doi:10.1073/pnas.1414653112.
- [31] A. Kianercy, R. Veltri, K.J. Pienta, Critical transitions in a game theoretic model of tumour metabolism., *Interface Focus.* 4 (2014) 20140014. doi:10.1098/rsfs.2014.0014.
- [32] Y. Chen, H. Wang, J. Zhang, K. Chen, Y. Li, D. Hanahan, R.A. Weinberg, D. Hanahan, R.A. Weinberg, N.M. Moore, A.T. Lefor, H.P. Greenspan, H.M. Byrne, J.R. King, D.L.S. McElwain, L. Preziosi, H.M. Byrne, L. Preziosi, T. Roose, S.J. Chapman, P.K. Maini, M.E. Hubbard, H.M. Byrne, G. Sciumé, T. Balois, M.B. Amar, A.R. Kansal, J.E. Schmitz, A.R. Kansal, S. Torquato, D. Drasdo, S. Hohme, M.L. Martins, S.C. Ferreira, M.J. Vilela, T.S. Deisboeck, Z. Wang, P. Macklin, V. Cristini, K.A. Rejniak, A.R. Anderson, B. Waclaw, A.R.A. Anderson, A.M. Weaver, P.T. Cummings, V. Quaranta, A. Giese, R. Bjerkvig, M.E. Berens, M. Westphal, K. Polyak, R.A. Weinberg, P. Nowell, T.S. Deisboeck, I.D. Couzin, V. Fodale, M. Pierobon, L. Liotta, E. Petricoin, D. Basanta, A. Deutsch, C.S. Attolini, F. Michor, C.A. Aktipis, R.M. Nesse, T.L. Vincent, R.A. Gatenby, L.M. Merlo, J.W. Pepper, B.J. Reid, C.C. Maley, N. Bellomo, M. Delitala, R.A. Gatenby, T.L. Vincent, Q. Liu, Z.

- Liu, A.S. Moustaid, M. Krzeslak, M. Martin, H. Basanta, H. Deutsch, I.P.M.
Tomlinson, W.F. Bodmer, I. Kareva, M. Archetti, A. Kaznatcheev, J.G. Scott, D.
Basanta, C. Tarrant, J.J. Cunningham, R.A. Gatenby, J.S. Brown, D. Basanta, D.
Basanta, A.R. Anderson, Y. Mansury, M. Diggory, T.S. Deisboeck, D. Basanta, M.
Simon, H. Hatzikirou, A. Deutsch, S.C. Ferreira, M.L. Martins, M.J. Vilela, S.C.
Ferreira, M.L. Martins, M.J. Vilela, D.G. Mallet, L.G. De Pillis, M.E. Kavousanakis,
Y. Jiao, S. Torquato, Y. Jiao, S. Torquato, S.C. Ferreira, M.L. Martins, M.J. Vilela, A.
Brú, F. Montel, M.A.C. Huergo, M.A.C. Huergo, M.A.C. Huergo, Simulation of
avasascular tumor growth by agent-based game model involving phenotype-phenotype
interactions, *Sci. Rep.* 5 (2015) 17992. doi:10.1038/srep17992.
- [33] M. Robertson-Tessi, R.J. Gillies, R.A. Gatenby, A.R.A. Anderson, Impact of
metabolic heterogeneity on tumor growth, invasion, and treatment outcomes, *Cancer
Res.* 75 (2015) 1567–1579. doi:10.1158/0008-5472.CAN-14-1428.
- [34] A.R. a Anderson, A.M. Weaver, P.T. Cummings, V. Quaranta, Tumor Morphology
and Phenotypic Evolution Driven by Selective Pressure from the Microenvironment,
Cell. 127 (2006) 905–915. doi:10.1016/j.cell.2006.09.042.
- [35] C.D. Nadell, K.R. Foster, J.B. Xavier, Emergence of spatial structure in cell groups
and the evolution of cooperation, *PLoS Comput. Biol.* 6 (2010).
doi:10.1371/journal.pcbi.1000716.
- [36] S. Mitri, J.B. Xavier, K.R. Foster, Social evolution in multispecies biofilms., *Proc.
Natl. Acad. Sci. U. S. A.* 108 Suppl (2011) 10839–46. doi:10.1073/pnas.1100292108.
- [37] J. Liu, A. Prindle, J. Humphries, M. Gabalda-sagarra, M. Asally, D.D. Lee, Metabolic
co-dependence gives rise to collective oscillations within biofilms, *Nature.* 523 (2015)

550–554. doi:10.1038/nature14660.

- [38] J.B. Xavier, C. Picioreanu, M.C.M. Van Loosdrecht, A framework for multidimensional modelling of activity and structure of multispecies biofilms, *Environ. Microbiol.* 7 (2005) 1085–1103. doi:10.1111/j.1462-2920.2005.00787.x.
- [39] W.F. Loomis, B. Magasanik, Glucose-lactose diauxie in *Escherichia coli.*, *J. Bacteriol.* 93 (1967) 1397–1401.
- [40] O.D.K. Maddocks, K.H. Vousden, Metabolic regulation by p53, *J. Mol. Med.* 89 (2011) 237–245. doi:10.1007/s00109-011-0735-5.
- [41] K.D. Bauer, P.C. Keng, R.M. Sutherland, Isolation of quiescent cells from multicellular tumor spheroids using centrifugal elutriation., *Cancer Res.* 42 (1982) 72–8. <http://www.ncbi.nlm.nih.gov/pubmed/7032695> (accessed May 28, 2016).
- [42] J.P. Freyer, Decreased mitochondrial function in quiescent cells isolated from multicellular tumor spheroids., *J. Cell. Physiol.* 176 (1998) 138–49. doi:10.1002/(SICI)1097-4652(199807)176:1<138::AID-JCP16>3.0.CO;2-3.
- [43] H.D. Preisler, I. Walczak, J. Renick, Y.M. Rustum, Separation of leukemic cells into proliferative and quiescent subpopulations by centrifugal elutriation., *Cancer Res.* 37 (1977) 3876–80. <http://www.ncbi.nlm.nih.gov/pubmed/71201> (accessed May 28, 2016).
- [44] M.D. Sherar, M.B. Noss, F.S. Foster, Ultrasound backscatter microscopy images the internal structure of living tumour spheroids., *Nature.* 330 (1987) 493–5. doi:10.1038/330493a0.
- [45] J. Laurent, C. Frongia, M. Cazales, O. Mondesert, B. Ducommun, V. Lobjois, Multicellular tumor spheroid models to explore cell cycle checkpoints in 3D., *BMC*

- Cancer. 13 (2013) 73. doi:10.1186/1471-2407-13-73.
- [46] J.J. Casciari, S. V. Sotirchos, R.M. Sutherland, Variations in tumor cell growth rates and metabolism with oxygen concentration, glucose concentration, and extracellular pH, *J. Cell. Physiol.* 151 (1992) 386–394. doi:10.1002/jcp.1041510220.
- [47] S.C. Dolfi, L.L.-Y. Chan, J. Qiu, P.M. Tedeschi, J.R. Bertino, K.M. Hirshfield, Z.N. Oltvai, A. Vazquez, The metabolic demands of cancer cells are coupled to their size and protein synthesis rates., *Cancer Metab.* 1 (2013) 20. doi:10.1186/2049-3002-1-20.
- [48] J. Fan, J.J. Kamphorst, R. Mathew, M.K. Chung, E. White, T. Shlomi, J.D. Rabinowitz, Glutamine-driven oxidative phosphorylation is a major ATP source in transformed mammalian cells in both normoxia and hypoxia., *Mol. Syst. Biol.* 9 (2013) 712. doi:10.1038/msb.2013.65.
- [49] I. Famili, J. Forster, J. Nielsen, B.O. Palsson, *Saccharomyces cerevisiae* phenotypes can be predicted by using constraint-based analysis of a genome-scale reconstructed metabolic network., *Proc. Natl. Acad. Sci. U. S. A.* 100 (2003) 13134–9. doi:10.1073/pnas.2235812100.
- [50] C.T. Hensley, B. Faubert, Q. Yuan, N. Lev-Cohain, E. Jin, J. Kim, L. Jiang, B. Ko, R. Skelton, L. Loudat, M. Wozzak, C. Klimko, E. McMillan, Y. Butt, M. Ni, D. Oliver, J. Torrealba, C.R. Malloy, K. Kernstine, R.E. Lenkinski, R.J. DeBerardinis, Metabolic Heterogeneity in Human Lung Tumors, *Cell.* 164 (2016) 681–694. doi:10.1016/j.cell.2015.12.034.
- [51] G. Bonuccelli, D. Whitaker-Menezes, R. Castello-Cros, S. Pavlides, R.G. Pestell, A. Fatatis, A.K. Witkiewicz, M.G. Vander Heiden, G. Migneco, B. Chiavarina, P.G. Frank, F. Capozza, N. Flomenberg, U.E. Martinez-Outschoorn, F. Sotgia, M.P.

- Lisanti, The reverse Warburg effect: Glycolysis inhibitors prevent the tumor promoting effects of caveolin-1 deficient cancer associated fibroblasts, *Cell Cycle*. 9 (2010) 1960–1971. doi:10.4161/cc.9.10.11601.
- [52] N. Solomon, I. James, N. Alphonsus, R. Nkiruka, A Review of Host-Parasite Relationships, *Annu. Res. Rev. Biol.* 5 (2015) 372–384. doi:10.9734/ARRB/2015/10263.
- [53] E. Obre, R. Rossignol, Emerging concepts in bioenergetics and cancer research: Metabolic flexibility, coupling, symbiosis, switch, oxidative tumors, metabolic remodeling, signaling and bioenergetic therapy, *Int. J. Biochem. Cell Biol.* 59 (2015) 167–181. doi:10.1016/j.biocel.2014.12.008.
- [54] F. Sotgia, U.E. Martinez-Outschoorn, M.P. Lisanti, The reverse warburg effect in osteosarcoma, *Oncotarget*. 5 (2014) 7982–7983. doi:10.18632/oncotarget.2352.
- [55] L. Alberghina, D. Gaglio, Redox control of glutamine utilization in cancer, *Cell Death Dis.* 5 (2014) e1561. doi:10.1038/cddis.2014.513.
- [56] D. Daye, K.E. Wellen, Metabolic reprogramming in cancer: Unraveling the role of glutamine in tumorigenesis, *Semin. Cell Dev. Biol.* 23 (2012) 362–369. doi:10.1016/j.semcdb.2012.02.002.
- [57] D.R. Wise, R.J. DeBerardinis, A. Mancuso, N. Sayed, X.-Y. Zhang, H.K. Pfeiffer, I. Nissim, E. Daikhin, M. Yudkoff, S.B. McMahon, C.B. Thompson, Myc regulates a transcriptional program that stimulates mitochondrial glutaminolysis and leads to glutamine addiction., *Proc. Natl. Acad. Sci. U. S. A.* 105 (2008) 18782–18787. doi:10.1073/pnas.0810199105.
- [58] M. Yuneva, N. Zamboni, P. Oefner, R. Sachidanandam, Y. Lazebnik, Deficiency in

- glutamine but not glucose induces MYC-dependent apoptosis in human cells, *J. Cell Biol.* 178 (2007) 93–105. doi:10.1083/jcb.200703099.
- [59] C. V. Dang, Rethinking the warburg effect with Myc micromanaging glutamine metabolism, *Cancer Res.* 70 (2010) 859–862. doi:10.1158/0008-5472.CAN-09-3556.
- [60] P. Lu, V.M. Weaver, Z. Werb, The extracellular matrix: A dynamic niche in cancer progression, *J. Cell Biol.* 196 (2012).
- [61] S. Benzekry, C. Lamont, A. Beheshti, A. Tracz, J.M.L. Ebos, L. Hlatky, P. Hahnfeldt, Classical Mathematical Models for Description and Prediction of Experimental Tumor Growth, *PLoS Comput. Biol.* 10 (2014) e1003800. doi:10.1371/journal.pcbi.1003800.
- [62] A.D. Conger, M.C. Ziskin, Growth of mammalian multicellular tumor spheroids., *Cancer Res.* 43 (1983) 556–60. <http://www.ncbi.nlm.nih.gov/pubmed/6848179> (accessed December 7, 2016).
- [63] R. a Gatenby, R.J. Gillies, Why do cancers have high aerobic glycolysis?, *Nat. Rev. Cancer.* 4 (2004) 891–899. doi:10.1038/nrc1478.
- [64] T.L. Yuan, G. Wulf, L. Burga, L.C. Cantley, Cell-to-cell variability in PI3K protein level regulates PI3K-AKT pathway activity in cell populations, *Curr. Biol.* 21 (2011) 173–183. doi:10.1016/j.cub.2010.12.047.
- [65] P. Tsou, B. Zheng, C.H. Hsu, A.T. Sasaki, L.C. Cantley, A fluorescent reporter of AMPK activity and cellular energy stress, *Cell Metab.* 13 (2011) 476–486. doi:10.1016/j.cmet.2011.03.006.
- [66] S.-H. Jiang, J. Li, F.-Y. Dong, J.-Y. Yang, D.-J. Liu, X.-M. Yang, Y.-H. Wang, M.-W. Yang, X.-L. Fu, X.-X. Zhang, Q. Li, X.-F. Pang, Y.-M. Huo, J. Li, J.-F. Zhang, H.-Y. Lee, S.-J. Lee, W.-X. Qin, J.-R. Gu, Y.-W. Sun, Z.-G. Zhang, Increased Serotonin

- Signaling Contributes to the Warburg Effect in Pancreatic Tumor Cells Under Metabolic Stress and Promotes Growth of Pancreatic Tumors in Mice., *Gastroenterology*. 153 (2017) 277–291.e19. doi:10.1053/j.gastro.2017.03.008.
- [67] M.A. Keibler, T.M. Wasylenko, J.K. Kelleher, O. Iliopoulos, M.G. Vander Heiden, G. Stephanopoulos, Metabolic requirements for cancer cell proliferation, *Cancer Metab.* 4 (2016) 16. doi:10.1186/s40170-016-0156-6.
- [68] D.C. Zielinski, N. Jamshidi, A.J. Corbett, A. Bordbar, A. Thomas, B.O. Palsson, Systems biology analysis of drivers underlying hallmarks of cancer cell metabolism., *Sci. Rep.* 7 (2017) 41241. doi:10.1038/srep41241.
- [69] R.J. DeBerardinis, T. Cheng, Q's next: the diverse functions of glutamine in metabolism, cell biology and cancer, *Oncogene*. 29 (2010) 313–324. doi:10.1038/onc.2009.358.
- [70] M.J. Lukey, W.P. Katt, R.A. Cerione, Targeting amino acid metabolism for cancer therapy, *Drug Discov. Today*. 22 (2017) 796–804. doi:10.1016/j.drudis.2016.12.003.
- [71] J. Son, C. a Lyssiotis, H. Ying, X. Wang, S. Hua, M. Ligorio, R.M. Perera, C.R. Ferrone, E. Mullarky, N. Shyh-Chang, Y. Kang, J.B. Fleming, N. Bardeesy, J.M. Asara, M.C. Haigis, R. a DePinho, L.C. Cantley, A.C. Kimmelman, Glutamine supports pancreatic cancer growth through a KRAS-regulated metabolic pathway, *Nature*. 496 (2013) 101–105. doi:10.1038/nature12040.
- [72] A. Brú, S. Albertos, J. Luis Subiza, J.L. García-Asenjo, I. Brú, The universal dynamics of tumor growth., *Biophys. J.* 85 (2003) 2948–2961. doi:10.1016/S0006-3495(03)74715-8.
- [73] B. Waclaw, I. Bozic, M.E. Pittman, R.H. Hruban, B. Vogelstein, M. a. Nowak, A

- spatial model predicts that dispersal and cell turnover limit intratumour heterogeneity, Nature. (2015). doi:10.1038/nature14971.
- [74] Z. Dai, A.A. Shestov, L. Lai, J.W. Locasale, A Flux Balance of Glucose Metabolism Clarifies the Requirements of the Warburg Effect, Biophys. J. 111 (2016) 1088–1100. doi:10.1016/j.bpj.2016.07.028.
- [75] O. Resendis-Antonio, A. Checa, S. Encarnación, Modeling core metabolism in cancer cells: Surveying the topology underlying the warburg effect, PLoS One. 5 (2010). doi:10.1371/journal.pone.0012383.
- [76] L.M. Thorpe, H. Yuzugullu, J.J. Zhao, PI3K in cancer: divergent roles of isoforms, modes of activation and therapeutic targeting, Nat. Rev. Cancer. 15 (2015) 7–24. doi:10.1038/nrc3860.
- [77] S. Selvarasu, D.S.-W. Ow, S.Y. Lee, M.M. Lee, S.K.-W. Oh, I.A. Karimi, D.-Y. Lee, Characterizing *Escherichia coli* DH5 α growth and metabolism in a complex medium using genome-scale flux analysis, Biotechnol. Bioeng. 102 (2009) 923–934. doi:10.1002/bit.22119.
- [78] A.M. Feist, C.S. Henry, J.L. Reed, M. Krummenacker, A.R. Joyce, P.D. Karp, L.J. Broadbelt, V. Hatzimanikatis, B.Ø. Palsson, K. Albe, M. Butler, B. Wright, K. Alexander, I. Young, E. Almaas, B. Kovacs, T. Vicsek, Z. Oltvai, A. Barabasi, H. Alper, K. Miyaoku, G. Stephanopoulos, T. Baba, T. Ara, M. Hasegawa, Y. Takai, Y. Okumura, M. Baba, K. Datsenko, M. Tomita, B. Wanner, H. Mori, C. Barrett, C. Herring, J. Reed, B. Palsson, D. Beard, S. Liang, H. Qian, S. Becker, A. Feist, M. Mo, G. Hannum, B. Palsson, M. Herrgard, M. Calhoun, K. Oden, R. Gennis, M. de Mattos, O. Neijssel, R. Caspi, H. Foerster, C. Fulcher, R. Hopkinson, J. Ingraham, P. Kaipa,

M. Krummenacker, S. Paley, J. Pick, S. Rhee, C. Tissier, P. Zhang, P. Karp, M. Covert, E. Knight, J. Reed, M. Herrgard, B. Palsson, M. Covert, B. Palsson, J. Edwards, R. Ibarra, B. Palsson, J. Edwards, B. Palsson, S. Elena, R. Lenski, A. Feist, J. Scholten, B. Palsson, F. Brockman, T. Ideker, E. Fischer, N. Zamboni, U. Sauer, S. Fong, A. Burgard, C. Herring, E. Knight, F. Blattner, C. Maranas, B. Palsson, C. Ghim, K. Goh, B. Kahng, G. Grass, M. Otto, B. Fricke, C. Haney, C. Rensing, D. Nies, D. Munkelt, M. Hakobyan, H. Sargsyan, K. Bagramyan, R. Helling, C. Henry, L. Broadbelt, V. Hatzimanikatis, C. Henry, M. Jankowski, L. Broadbelt, V. Hatzimanikatis, C. Herring, A. Raghunathan, C. Honisch, T. Patel, M. Applebee, A. Joyce, T. Albert, F. Blattner, D. van den Boom, C. Cantor, B. Palsson, R. Ibarra, J. Edwards, B. Palsson, M. Imielinski, C. Belta, A. Halasz, H. Rubin, P. Janssen, L. Goldovsky, V. Kunin, N. Darzentas, C. Ouzounis, A. Joyce, B. Palsson, A. Joyce, J. Reed, A. White, R. Edwards, A. Osterman, T. Baba, H. Mori, S. Lesely, B. Palsson, S. Agarwalla, I. Keseler, J. Collado-Vides, S. Gama-Castro, J. Ingraham, S. Paley, I. Paulsen, M. Peralta-Gil, P. Karp, S. Kikuchi, I. Shibuya, K. Matsumoto, A. Kümmel, S. Panke, M. Heinemann, A. Kümmel, S. Panke, M. Heinemann, S. Lee, H. Woo, D. Lee, H. Choi, T. Kim, H. Yun, M. Lotierzo, B.T.S. Bui, D. Florentin, F. Escalettes, A. Marquet, R. Mahadevan, C. Schilling, R. Majewski, M. Domach, N. Mnatsakanyan, K. Bagramyan, A. Trchounian, E. Nikolaev, A. Burgard, C. Maranas, Y. Noguchi, Y. Nakai, N. Shimba, H. Toyosaki, Y. Kawahara, S. Sugimoto, E. Suzuki, C. Pal, B. Papp, M. Lercher, C. Pal, B. Papp, M. Lercher, P. Csermely, S. Oliver, L. Hurst, B. Palsson, S. Pirt, J. Pramanik, J. Keasling, J. Pramanik, J. Keasling, N. Price, J. Reed, B. Palsson, J. Reed, I. Famili, I. Thiele, B. Palsson, J. Reed, B. Palsson, J. Reed, T.

Patel, K. Chen, A. Joyce, M. Applebee, C. Herring, O. Bui, E. Knight, S. Fong, B. Palsson, J. Reed, T. Vo, C. Schilling, B. Palsson, M. Riley, T. Abe, M. Arnaud, M. Berlyn, F. Blattner, R. Chaudhuri, J. Glasner, T. Horiuchi, I. Keseler, T. Kosuge, H. Mori, N. Perna, G. Plunkett, K. Rudd, M. Serres, G. Thomas, N. Thomson, D. Wishart, B. Wanner, S. Silver, J. Stelling, R. Thauer, K. Jungermann, K. Decker, P. Vander Horn, A. Backstrom, V. Stewart, T. Begley, A. Varma, B. Boesch, B. Palsson, A. Varma, B. Palsson, A. Varma, B. Palsson, I. Williams, L. Frank, A genome-scale metabolic reconstruction for *Escherichia coli* K-12 MG1655 that accounts for 1260 ORFs and thermodynamic information., *Mol. Syst. Biol.* 3 (2007) 121.
doi:10.1038/msb4100155.

- [79] L. Li, S.F. Nørrelykke, E.C. Cox, Persistent Cell Motion in the Absence of External Signals: A Search Strategy for Eukaryotic Cells, *PLoS One.* 3 (2008) e2093.
doi:10.1371/journal.pone.0002093.

CHAPTER 4

MITOCHONDRIAL REDOX HOMEOSTASIS IN BREAST CANCER CELLS UNDER CHRONIC HYPOXIA

4-1 Introduction

Cancer is a tissue-scale disease. In tumors, uncontrolled proliferation of the malignant cells leads to exhaustion of local metabolites and imposes diffusion limitations on nutrients in the tumor microenvironment due to the tumor expansion [1]. Depending on the stage of tumor progression, these conditions along with others could be either beneficial or obstructive to tumor growth [2].

One of the outcomes of these conditions is hypoxia. Tumor hypoxia is a common trait in tumors and acts as a double-edged sword in regulating tumor progression. The immediate effect of hypoxia on the cell populations (both the malignant and non-malignant cells) in a tumor tissue is through proteomic changes [1,3]. This acute effect of hypoxia is known to impair cellular growth via arrest of the cell cycle that eventually leads to cellular quiescence and even apoptosis. At this first glance, it seems that hypoxia regulates tumor growth negatively. However, hypoxia promotes tumor growth chronically via many other mechanisms. For instance, tumor cells adapt to a glycolytic metabolic phenotype upon hypoxia and this adaptation makes them become less dependent on oxygen for energy and growth [4]. Additionally, proteomic changes such as inhibition of gene expression in integrins [5] and secretion of signaling molecules (e.g., pro-angiogenic factors, [6]) that alter the extracellular matrices also promote tumor metastasis. On larger time scales, tumor hypoxia contributes to tumor progression by promoting clonal

heterogeneity and genomic instability by serving as a selection pressure [7]. These complications that result from tumor hypoxia have led to difficulties in treating tumors with non-surgical interventions (e.g. radiation therapy, chemotherapy etc.). Therefore, understanding how tumor cells adapt to, survive and proliferate under prolonged hypoxia is crucial for developing new therapeutic strategies to alleviate the challenge of treating hypoxic tumors with traditional methods.

The proteomic changes in tumor cells due to hypoxia are mediated through reactive oxygen species (ROS). Upon hypoxia, generation of ROS increases in the mitochondria via the electron transport chain (ETC) due to the lack of oxygen supply. ROS further participate in regulation of cellular functions in diverse ways: at high levels, ROS activate autophagic/apoptotic pathways that lead to cell death; at low levels, ROS act as signaling agents that drive phenotypic changes in the tumor cells [8,9]. Therefore, redox balance is critical for the fate of the tumor cells. When ROS is elevated, antioxidants need to be in place to prevent damages to the cell from ROS.

4-2 *NADPH generation in tumor cells*

The abundance of antioxidants (e.g., glutathione) in the cell is dependent upon the generation of NADPH as the reducing agent [10]. Depending on the compartment of the cell, NADPH can be produced via several different metabolic pathways. Classically, the cytosolic oxidative pentose phosphate pathway (PPP) is considered the primary source of NADPH. However, it is known that NADPH cannot be transported across the intracellular membranes [11], and multistep shuttles need to be involved for the NADPH transfer between compartments [12]. Therefore, compartment-specific metabolic processes need to be in place to maintain the proper subcellular NADP⁺/NADPH ratio and subsequently ROS levels. Importantly, hypoxia-induced

ROS production mainly comes from the ETC in the mitochondria. Several potential sources of mitochondrial NADPH have been reported in the literature, including reactions catalyzed by isozymes of malic enzyme (i.e., ME3, [13,14]), isocitrate dehydrogenase (i.e., IDH2, [15]), aldehyde dehydrogenase (i.e., ALDH1L2, [16]) and methylene tetrahydrofolate dehydrogenase (i.e., MTHFD2/2L, [17,18]) (**Fig. 4-1**).

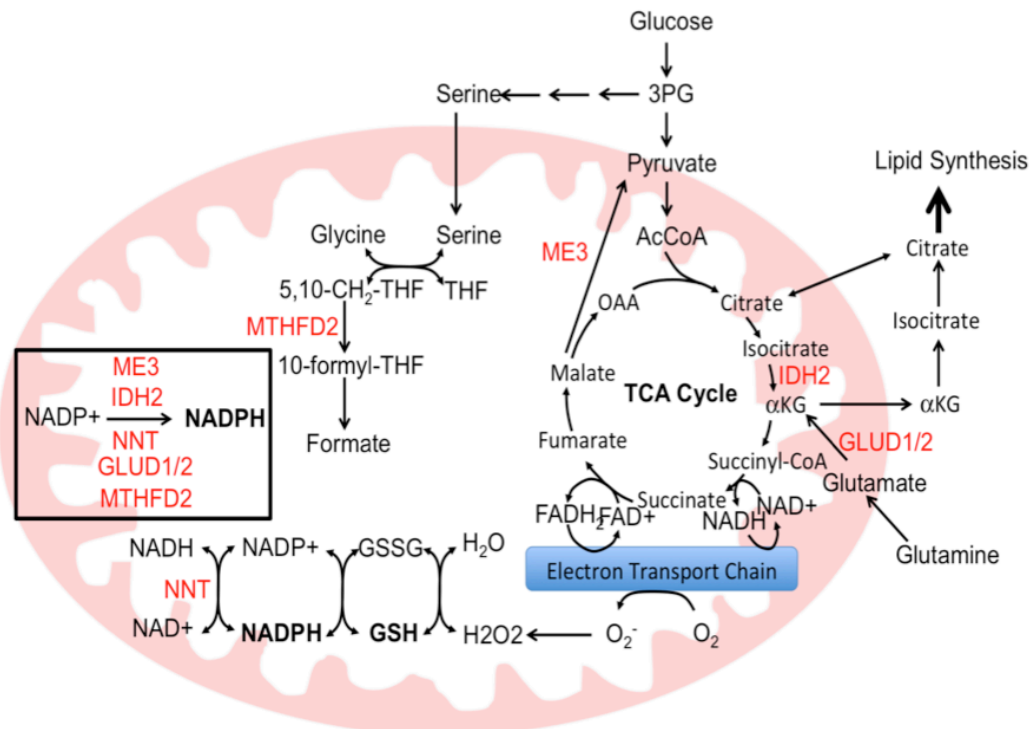


Figure 4-1: Major NADP⁺/NADPH coupled metabolic pathways in the mitochondria. Red: metabolic enzymes catalyzing reactions coupled with NADPH regeneration.

Previous studies have demonstrated the importance of one-carbon metabolism in mitigating mitochondrial ROS in tumor cells [12,19]. Specifically, the mechanism proposed [20–22] by Ye *et al.* and Samanta *et al.* starts with serine synthesis from glucose in the cytosol catalyzed by a series of enzymes including phosphoglycerate dehydrogenase (PHGDH). Serine can further participate in the one-carbon (folate) cycle in the mitochondria with the first step catalyzed by serine hydroxymethyl transferase 2 (SHMT2). The subsequent pathways involved

in NADPH regeneration are catalyzed by MTHFD2/2L and ALDH1L2 (**Fig. 4-2**). However, these studies focused on cancer cells with short-term exposure (within 24 hours) to hypoxia and do not necessarily capture the adapted metabolic state of tumor cells under prolonged hypoxia (a more physiological representation of hypoxic tumors *in vivo*).

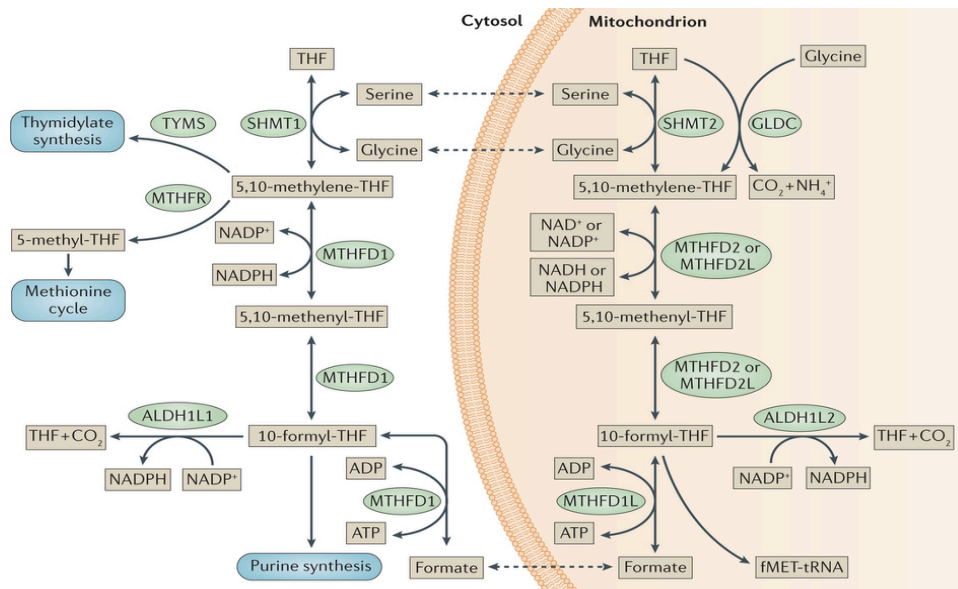


Figure 4-2: NADPH regeneration in mitochondrial one-carbon (folate) cycle. (Adapted from Yang and Vousden, 2016; [22])

In this study, we aim to explore how tumor cells adapt metabolically in the mitochondria under prolonged hypoxia *in vitro* to mitigate ROS levels via production of NADPH. Since genetic and epigenetic profiles vary drastically across different tumor types, we constrain our study to breast cancer cells (see **Section 4.3**). We first examined the viability of these tumor cells under normoxia vs. hypoxia by performing proliferation assays. Our results show that tumor cells continue to proliferate under prolonged hypoxia *in vitro*, indicating that cellular mechanisms are in place to maintain redox balance within the cells. We further demonstrate that tumor cells were indeed experiencing hypoxia in our hypoxia culture conditions by showing the changes in hypoxia-induced protein expressions and ¹³C isotope labeling profiles. By performing

immunoblot assays to examine the expression of proteins (i.e., enzymes) in the mitochondrial NADPH-coupled pathways, we found that the expression of IDH2 is up-regulated while the others become down-regulated under prolonged hypoxia, which led us to propose an IDH-mediated redox shuttle transferring NADPH into the mitochondria to mitigate mitochondrial ROS, possibly fueled by glutamine metabolism. I discuss the results in detail under *Section 4.4*.

4-3 *Materials and Methods*

4-3-1 *Cell Culture and proliferation assay*

Breast cancer cell lines BT-474, T-47D, MCF7, MDA-MB-468, BT-549, Hs578T, MDA-MB-453, HCC38 and MDA-MB-231 were obtained from the American Type Cell Culture Collection (ATCC). The TSE breast cancer cell line was kindly supplied by Dr. Steven Abcouwer (University of Michigan). All breast cancer cell lines were maintained at 37 °C, 5% CO₂ atmosphere, in RPMI 1640 medium containing 2 mM glutamine (Gibco) and supplemented with 10% FBS (Gibco) for normoxia experiments. Hypoxia experiments were performed using a hypoxia incubator at 37 °C, 5% CO₂ and 1% O₂. To obtain the doubling time, breast cancer cell lines were cultured on 6-well plate in biological triplicates for each end-time point and media changed every other day. End-time points were 2, 4, and 6 days. Cell lines were periodically tested for Mycoplasma contamination.

4-3-2 *Immunoblot assays*

Immunoblot assays were performed as described previously [23]. Briefly, whole-cell lysates were prepared in lysis buffer (50 mM HEPES pH 8.0, 150 mM NaCl, 1 mM Na₃VO₄, 25 mM NaF, 1% (v/v) Triton X-100, 1 mM MgCl₂, 50 mM β-glycerophosphate, 30 mg/ml leupeptin, 5 mg/ml aprotinin) followed by centrifugation to remove any insoluble debris. Protein concentration was then determined by Bradford assay (Bio-Rad), and lysate proteins denatured

by boiling for 5 min in reducing SDS-sample buffer. Equal amount of proteins ($\leq 20\text{mg/lane}$) for each sample were resolved on Novex 4–20% Tris-glycine mini or midi protein gels (Life Technologies), transferred to polyvinylidene difluoride membranes (PerkinElmer) and detected by immunoblotting using the following antibodies: α/β -tubulin (CST, 1:5000), HIF1a (CST, 1:5000), GLUT1 (CST, 1:4000), PDHK1 (CST, 1:4000), PHGDH (CST, 1:8000), MTHFD2 (CST, 1:4000), MTHFD1L (CST, 1:4000), IDH2 (Invitrogen, 1:4000) and succinyl-CoA synthetase (CST, 1:4000).

4-3-3 Metabolomics

Breast cancer cell lines were grown to $\sim 80\%$ confluence in growth medium (RPMI 1640, 2mM glutamine, 10% FBS) under either hypoxia or normoxia on 6-well plates in biological triplicate. To trace glutamine metabolism, breast cancer cell lines were grown as above and then transferred into glutamine-free RPMI 1640 containing 10% dialysed FBS and supplemented with 2mM U-13C-glutamine for 11 hours. For all metabolomics experiments, the quantity of the metabolite fraction analysed was adjusted to the corresponding protein concentration calculated upon processing a parallel well in a 6-well dish.

To collect the metabolites, the medium was removed at the end of labeled media treatment and the cell lysate harvested with ice cold 80% MeOH on dry ice. The soluble metabolite fractions were cleared by centrifugation, dried under nitrogen, then resuspended in 50:50 MeOH:H₂O mixture for LC–MS analysis.

Analysis was performed on an Agilent 1260 UHPLC combined with a 6520 Accurate-Mass Q-TOF LC/MS. Agilent MassHunter Workstation Software LC/MS Data Acquisition for 6200 series TOF/6500 series Q-QTOF (version B.06.01) was used for calibration and data acquisition. For chromatography, a Phenomenex Luna NH₂ column (5 μm , 1.0 x 150mm, 1.7 μm) was used

with mobile phase (A) consisting of 20mM ammonium acetate, pH 9.6 in water; mobile phase (B) consisting of acetonitrile. Gradient program: mobile phase (B) was at 80% B, increased to 100% A in 15 min, held for 5 min before return to 80% B and held for 20 min of initial condition. The column was at 25 °C and 5 µl of sample was injected into the LC-MS with a flow rate of 0.09 ml/min. Calibration of TOF MS was achieved through Agilent ESI-Low Concentration Tuning Mix. In negative acquisition mode, key parameters were: mass range 50-1000 da, Gas temp 350 °C, Fragmentor 150 V, Skimmer 65 v, Drying Gas 10 l/min, Nebulizer at 20 psi and Vcap 3500 V, reference ions were 119.0363 and 980.01637 infused from a reference bottle B at pressure of 5 psi. All samples were acquired in centroid data formats. For data analysis, we used Agilent MassHunter Workstation Software Profinder B.08.00 with Batch Targeted Feature Extraction and Batch Isotopologue Extraction and Qualitative Analysis B.07.00. Various parameter combinations, e.g. mass and RT tolerance, were used to find best peaks and signals by manual inspection. Key parameters were: mass tolerance = 20 or 10 ppm and RT tolerance = 1 or 0.5 min. Isotopologue ion thresholds, the anchor ion height threshold was set to 250 counts and the threshold of the sum of ion heights to 500 counts. Co-elution correlation threshold was set to 0.3.

4-4 Results and Discussion

Before we investigated the metabolic change in the cells, we performed proliferation assays to see how hypoxia impacts their proliferation rates. We subjected 7 breast cancer cell lines to normoxia (20% O₂) and hypoxia (1% O₂) over a time course of 6 days and performed cell counting on days 2, 4, and 6 to determine the doubling time. Surprisingly, most cell lines retain their proliferation under hypoxia (**Fig. 4-3**). It is worth noting that hypoxia impacts the proliferation of luminal breast cancer cells more significantly compared to basal cell lines, which

indicates a higher dependence on oxygen metabolism via oxidative phosphorylation (OXPHOS) in luminal breast cancer cell lines for survival and proliferation.

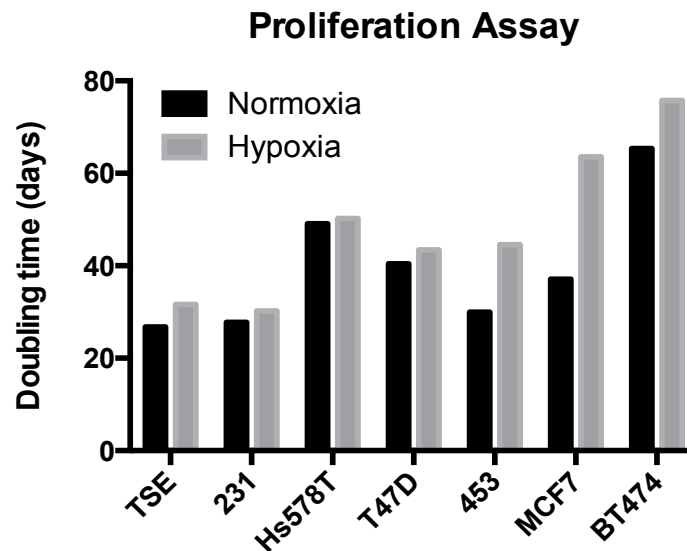


Figure 4-3: Doubling time of breast cancer cell under normoxia vs. hypoxia. TSE, MDA-MB-231 (231), Hs578T and T47D are basal breast cancer cell lines. MDA-MB-453 (453), MCF7 and BT474 are luminal cancer cell lines. Values are averaged over measurements with three replicates.

We then asked whether the cells are indeed experiencing hypoxia by looking at the expression level of several hypoxia-activated proteins. One of the primary enzymes activated upon hypoxia is hypoxia-induced factor 1-alpha (HIF1a) [24]. HIF1a further binds to hypoxic response elements (HREs) of target genes to modulate metabolism such as through activation of the glucose transporter 1 (GLUT1) and pyruvate dehydrogenase kinase 1 (PDHK1) [4]. These two enzymes shift tumor cell metabolism from OXPHOS-dependent to glycolysis-dependent energy production by promoting glucose uptake and blocking pyruvate entry into the mitochondria [25].

Figure 4-4 presents the protein expression of HIF1a, GLUT1 and PDHK1 at different time points under hypoxia (1% O₂). In all four of the cell lines, HIF1 α is up-regulated under

hypoxia with peaked expression at 48 hours and 24 hours for basal cell lines and luminal cell lines respectively (**Fig. 4-4**). The more immediate response of luminal cell lines in HIF1a activation supports the previous observation that hypoxia has a greater impact on growth of luminal cells than that of basal cell lines (**Fig. 4-3**). It is interesting that after 24 or 48 hours in hypoxia, HIF1a expression decreases, indicating ROS-regulating mechanisms are in place in the cells at this adapted metabolic state. Following HIF1a activation, GLUT1 is activated and persists under prolonged hypoxia ($t = 72$ hours in **Fig. 4-4**). Additionally, PDHK1 is also up-regulated, preventing pyruvate from going into mitochondria and possibly facilitating in shunting of pyruvate into lactate (a Warburg trait). The unregulated expression of these proteins confirms that hypoxia was present and suggests that it modulated the metabolic changes in breast cancer cells.

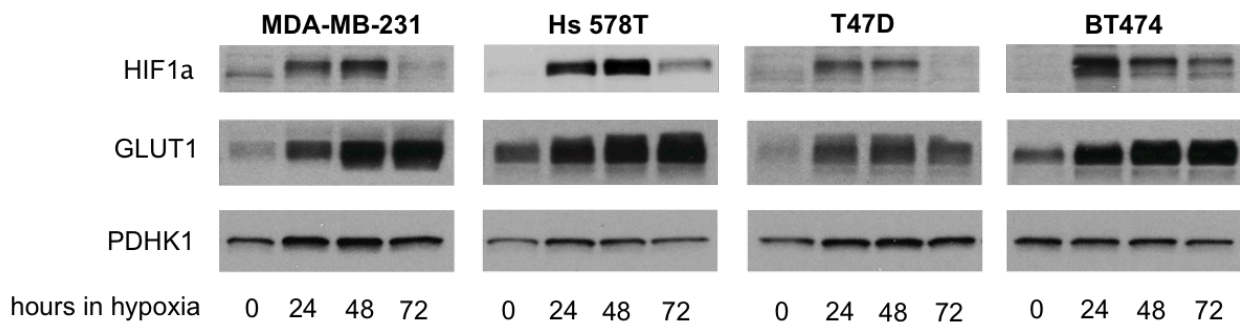


Figure 4-4: Hypoxia induces expression of enzymes associated with glycolysis. Immunoblot assay of lysates prepared with MDA-MB-231, Hs578T, T47D and BT474 cultured in 1% O₂ and terminated at different end-time points. $t=0$ represents normoxia.

We next explored the metabolic changes in one-carbon metabolism of the breast cancer cells (**Fig. 4-5(a)**). We exposed breast cancer cell lines to 1% O₂ for 82 hours and performed immunoblot assays to see the protein expression along the one-carbon pathways shown in **Figure 4-5(c)**. Surprisingly, our results indicate an opposite trend compared to what was reported in the literature [20,21]. Specifically, GLUT1 remains up-regulated under this

prolonged hypoxic culture condition suggesting an altered metabolic state in the cells, consistent with the data shown in **Figure 4-4**. However, PHGDH, MTHFD2 and methylene tetrahydrofolate dehydrogenase 1 like (MTHFD1L) are all significantly down regulated at 82 hours in hypoxia. Previous studies have proposed that mitochondrial one-carbon metabolism is up-regulated and required to maintain mitochondrial redox homeostasis as an NADPH source under acute hypoxia (24 hours) [20,21]. The fact that our results show a different trend after longer exposure to hypoxia suggests that the metabolic adaption of breast cancer cells is time-dependent and points to the possibility of a transient metabolic state at 24 hours. Our data suggests that one-carbon metabolism is not likely to be utilized for NADPH generation under prolonged hypoxia and an alternative mechanism needs to be in place to mitigate mitochondrial ROS in breast cancer cells.

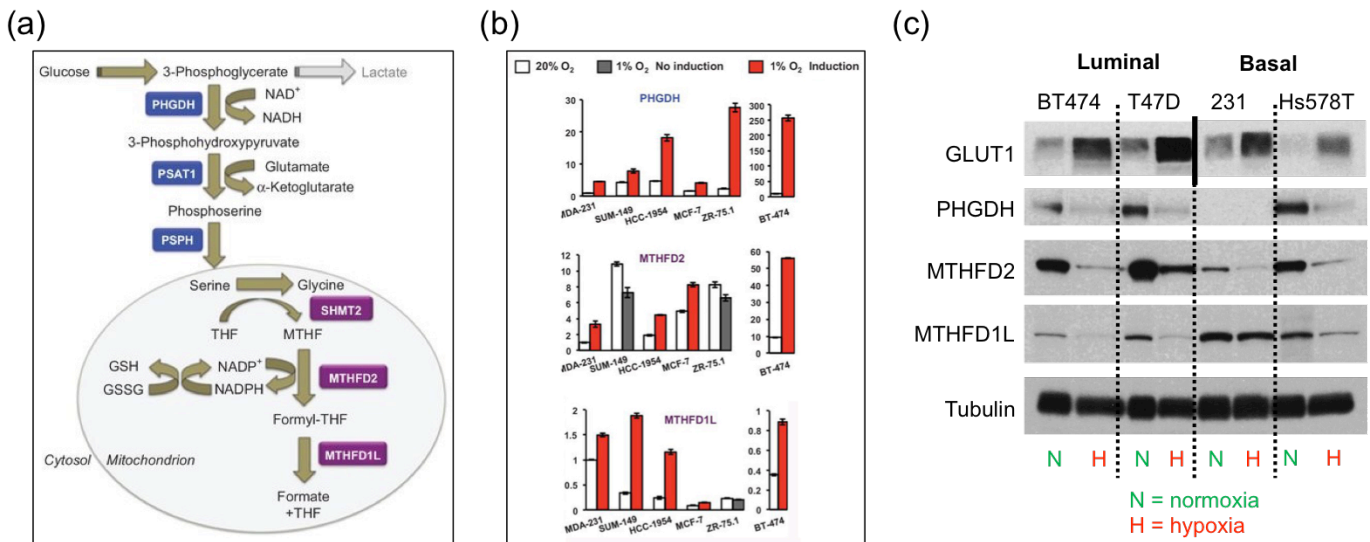


Figure 4-5: Enzymes in one-carbon metabolism are down regulated under prolonged hypoxia. (a) Schematic of one-carbon metabolism of mammalian cells. (b) Samanta *et al.* showed up-regulated mRNA expression of mitochondrial one-carbon metabolism under 1% O₂ for 24 hours. (c) Immunoblot assays of enzymes catalyzing mitochondrial one-carbon

metabolism are down regulated under prolonged hypoxia (1%O₂ for 82 hours). (Figs. 4(a) and 4(b) are adapted from Samanta et al., 2016; [21])

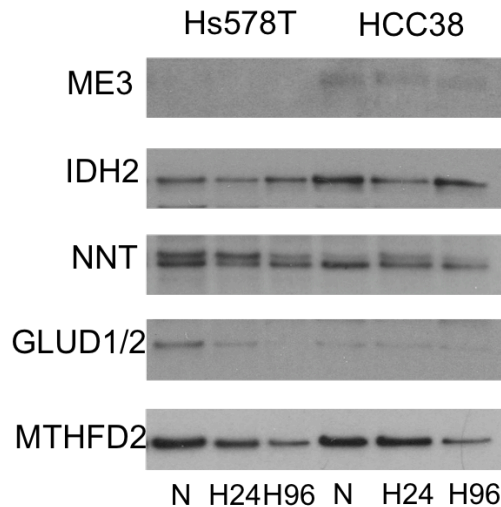


Figure 4-6: Metabolic enzymes catalyzing reactions coupled with NADP⁺/NADPH are down regulated under prolonged hypoxia.

We then went on to explore several other possible sources of NADPH in the mitochondria. Other than the aforementioned ME3 and IDH2, glutamate dehydrogenase (GLUD1/2) and nicotinamide nucleotide transhydrogenase (NNT) have also been reported to contribute to the pool of NADPH in the mitochondria [26,27]. However, our immunoblot results indicate down regulations of NNT, GLUD1/2 and ME3 at different levels after exposure to prolonged hypoxia (**Fig. 4-6**). Interestingly, significant up-regulation of IDH2 is present in several breast cancer cell lines we looked at, especially the basal types (**Figs. 4-6 and 7(a)**). Across the 6 basal cell lines, inconsistent protein expression levels are present at 24-hour hypoxia with a mix of up- and down-regulation of IDH2. However, looking at the data points at 96-hr hypoxia, there is a clear up-regulation across all cell lines. This result again suggests that the breast cancer cells are at a transient metabolic state at 24-hour hypoxia. Although IDH2 has been previously proposed to run in the reductive carboxylation pathway consuming

mitochondrial NADPH under hypoxia to fuel citrate and downstream lipid synthesis [28,29], it is classically considered to be running in the oxidative direction of TCA cycle producing NADPH under normoxia [30,31]. We further note that the TCA cycle in these breast cancer cells is truncated due to significant down-regulation of succinyl-CoA synthetase (**Fig. 4-7(b)**). Together, these results led us to propose an IDH-mediated redox shuttle transferring NADPH into the mitochondria (**Fig. 4-8**).

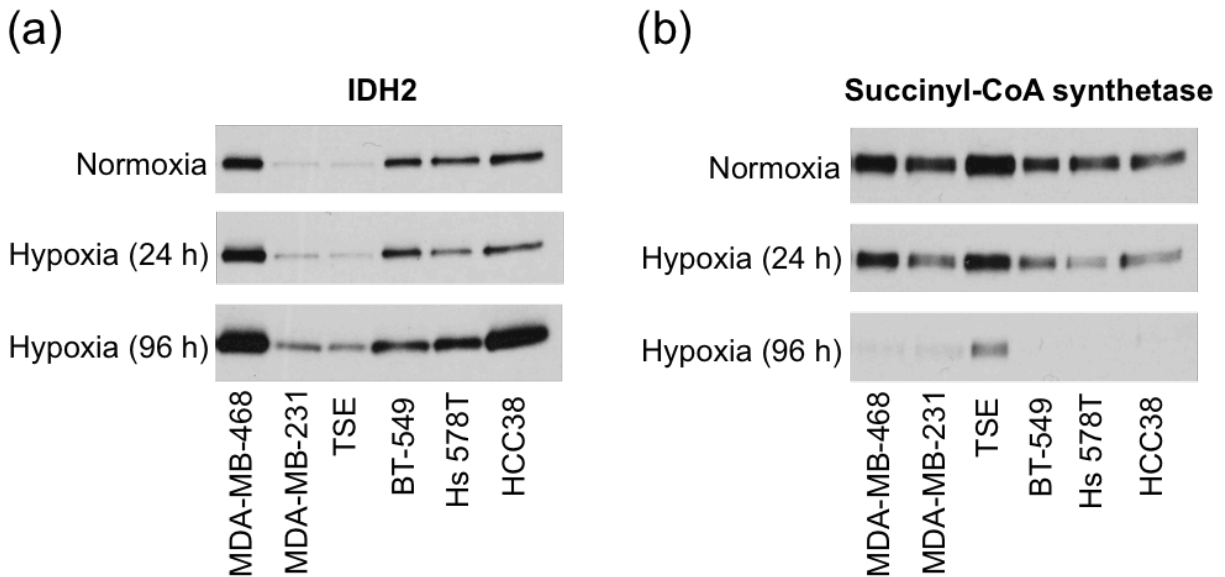


Figure 4-7: Immunoblots of IDH2 and succinyl-CoA synthetase across different basal breast cancer cell lines.

Figure 4-8 presents our hypothesis on the IDH-mediated redox shuttle in breast cancer cells under prolonged hypoxia. Specifically, the reaction catalyzed by IDH2 persists in the oxidative direction of TCA cycle consuming isocitrate and NADP⁺ to produce alpha-ketoglutarate (α KG) and NADPH. α KG further travels into the cytosol and participates in the reductive carboxylation catalyzed by IDH1 to consume NADPH (e.g. produced by oxidative PPP) and produce isocitrate (and subsequently citrate) that can further contribute to lipid synthesis.

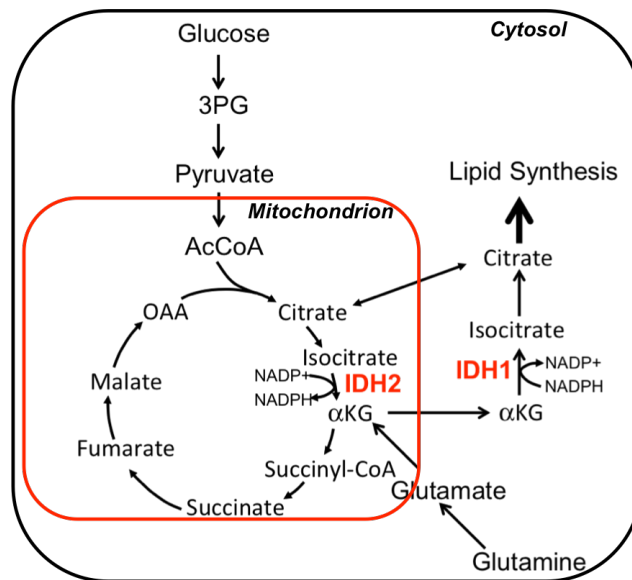


Figure 4-8: Hypothesis of IDH-mediated redox shuttle under prolonged hypoxia in breast cancer cells.

Jiang *et al.* have previously proposed this mechanism for shuttling NADPH from cytosol to mitochondria to mitigate elevated mitochondrial ROS evolved from anchorage-independent tumor growth [32]; it has not been previously reported in the context of chronic hypoxia. As an initial step to validate our hypothesis, we performed ^{13}C -labeling experiment using U- ^{13}C glutamine with liquid chromatography-mass spectrometry (LC-MS) (**Fig. 4-9(a)**). The use of U- ^{13}C glutamine allows us to use the ratio of m+4 to m+5 for citrate and the ratio of m+3 to m+4 for malate accordingly as a metric to determine the level of reductive carboxylation in the cells [33]. **Figure 9(b)** presents the labeling experiment performed with Hs578T. We see clearly that m+5 glutamine enters the cells and is converted into m+5 glutamate via glutaminase (GLS1/2) followed by production of m+5 αKG under both normoxia and hypoxia (top row). However, we observe drastically different labeling distributions between normoxia and hypoxia in the downstream metabolites, citrate and malate. Under normoxia, the fraction of labeling remains diversely distributed among citrate isotopologues from the turning of TCA cycle. Once the TCA

cycle is interrupted due to hypoxia, the citrate m+5 isotopologue constitutes almost 80% of the total abundance of citrate. Additionally, we observe a significant shift from m+4 to m+3 isotopologues for malate. Together, these results suggested the establishment of reductive carboxylation mediated via glutamine metabolism in Hs578T under prolonged hypoxia. Nonetheless, this data alone does not allow us to specify the compartment in which the reductive carboxylation occurs, whether it is in the cytosol or the mitochondria of the cells. To confirm the direction-specific shuttling mechanism we proposed, further validation needs to be carried out, as we discuss in the following section.

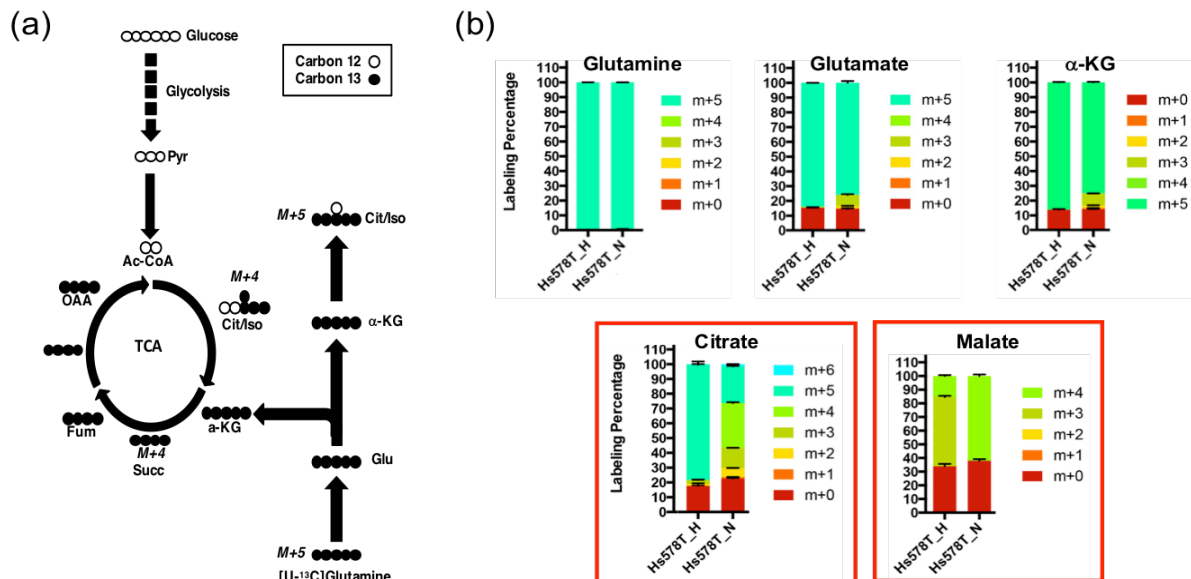


Figure 4-9: ^{13}C -labeling experiment with $\text{U-}^{13}\text{C}$ glutamine under normoxia vs. hypoxia. (a) Schematic of distribution of ^{13}C from $\text{U-}^{13}\text{C}$ glutamine. (Figure courtesy of Ahmad Cluntun) (b) Hs578T was exposed to 1% O_2 for 3 days and then labeled with $\text{U-}^{13}\text{C}$ glutamine for 11 hours in RPMI without glutamine. The relative amount of metabolites was measured using LC-MS.

4-5 Conclusions and future works

In this study, we explored how breast cancer cells mitigate mitochondrial ROS under prolonged hypoxia. Our preliminary results suggested that breast cancer cells survive and proliferate under such conditions. The breast cancer cells also exhibit distinct metabolic profiles

at different exposure times to hypoxia indicating that tumor cells do not commit to a fixed metabolic phenotype upon hypoxia but instead undergo metabolic adaptation over a period of time that spans from hours to days. More importantly, while others have pointed to one-carbon metabolism for the mitigation of mitochondrial ROS under hypoxia [20,21], by showing the enzyme expression in NADPH-coupled mitochondrial reactions (under short and long exposures to hypoxia), we infer that an IDH-mediated redox transfer mechanism mediated via glutamine metabolism is in place for mitochondrial redox regulation (**Fig. 4-8**).

To further validate our proposed IDH-mediated redox transfer mechanism, a few follow-up experiments need to be performed with the first one being the knockdown of IDHs (IDH1 and IDH2) in the cells after being exposed to prolonged hypoxia combined with measurement of ^{13}C labeling in citrate. The knockdown of IDHs can be induced upon dosage of doxycycline by infecting cells with doxycycline-inducible constructs targeting IDH1/2 shRNAs beforehand. By looking at the relative level of M+5 citrate with LC-MS, this experiment will inform us on either IDH1 or IDH2 as the direct contributor to reductive carboxylation. Once this insight is gained, we can further measure mitochondrial ROS level upon knockdown of IDHs. If our hypothesis of the IDH-mediated redox shuttle is valid, ROS elevation in the mitochondria will be observed and the knockdown of IDH2 will be more disastrous to the survival/proliferation of breast cancer cells as it is the primary NADPH source in the mitochondria under prolonged hypoxia.

Our study elucidates the extended metabolic adaptation in breast cancer cells to tumor microenvironment (i.e., hypoxia) and underlines the importance of a previously overlooked redox-regulating mechanism in breast cancer cells under chronic hypoxia. Our results will add significant values to our knowledge of the fundamentals in cancer metabolism, and points to the importance of addressing the specific conditions (e.g., duration of experimental treatment) and

contexts (e.g., tissue of origin) in which experiments are conducted in the field of cancer study. We infer that future studies should extend this effort to tumor cells that originated from other types of tissue to determine the comprehensiveness of this IDH-mediated redox shuttle among cancer types. Additionally, our findings serve as a crucial piece of information added to the overall picture of the metabolic profile of hypoxia-adapted tumor cells and hence must be taken into account in the design of therapeutic strategies that target redox regulation in tumor cells.

4-6 *References*

- [1] P. Vaupel, Tumor Hypoxia: Causative Factors, Compensatory Mechanisms, and Cellular Response, *Oncologist*. 9 (2004) 4–9. doi:10.1634/theoncologist.9-90005-4.
- [2] D.F. Quail, J.A. Joyce, Microenvironmental regulation of tumor progression and metastasis., *Nat. Med.* 19 (2013) 1423–37. doi:10.1038/nm.3394.
- [3] M. Hockel, P. Vaupel, Tumor Hypoxia: Definitions and Current Clinical, Biologic, and Molecular Aspects, *JNCI J. Natl. Cancer Inst.* 93 (2001) 266–276. doi:10.1093/jnci/93.4.266.
- [4] K.L. Eales, K.E.R. Hollinshead, D.A. Tennant, Hypoxia and metabolic adaptation of cancer cells, *Oncogenesis*. 5 (2016) e190. doi:10.1038/oncsis.2015.50.
- [5] N.M. Hasan, G.E. Adams, M.C. Joiner, J.F. Marshall, I.R. Hart, Hypoxia facilitates tumour cell detachment by reducing expression of surface adhesion molecules and adhesion to extracellular matrices without loss of cell viability., *Br. J. Cancer*. 77 (1998) 1799–1805. doi:10.1038/bjc.1998.299.
- [6] B.L. Krock, N. Skuli, M.C. Simon, Hypoxia-Induced Angiogenesis: Good and Evil, *Genes and Cancer*. 2 (2011) 1117–1133. doi:10.1177/1947601911423654.
- [7] K.R. Luoto, R. Kumareswaran, R.G. Bristow, Tumor hypoxia as a driving force in genetic

- instability, *Genome Integr.* 4 (2013) 1. doi:10.1186/2041-9414-4-5.
- [8] M. Schieber, N.S. Chandel, ROS function in redox signaling and oxidative stress, *Curr. Biol.* 24 (2014) R453–R462. doi:10.1016/j.cub.2014.03.034.
- [9] B. Poljsak, D. Šuput, I. Milisav, Achieving the balance between ROS and antioxidants: When to use the synthetic antioxidants, *Oxid. Med. Cell. Longev.* 2013 (2013) 956792. doi:10.1155/2013/956792.
- [10] D.N. Ekoue, C. He, A.M. Diamond, M.G. Bonini, Manganese superoxide dismutase and glutathione peroxidase-1 contribute to the rise and fall of mitochondrial reactive oxygen species which drive oncogenesis, *Biochim. Biophys. Acta - Bioenerg.* 1858 (2017) 628–632. doi:10.1016/j.bbabi.2017.01.006.
- [11] N. Pollak, M. Niere, M. Ziegler, NAD kinase levels control the NADPH concentration in human cells, *J. Biol. Chem.* 282 (2007) 33562–33571. doi:10.1074/jbc.M704442200.
- [12] C.A. Lewis, S.J. Parker, B.P. Fiske, D. McCloskey, D.Y. Gui, C.R. Green, N.I. Vokes, A.M. Feist, M.G. Vander Heiden, C.M. Metallo, Tracing Compartmentalized NADPH Metabolism in the Cytosol and Mitochondria of Mammalian Cells, *Mol. Cell.* 55 (2014) 253–263. doi:10.1016/j.molcel.2014.05.008.
- [13] G. Loeber, M.B. Dworkin, A. Infante, H. Ahorn, Characterization of cytosolic malic enzyme in human tumor cells, *FEBS Lett.* 344 (1994) 181–186. doi:10.1016/0014-5793(94)00386-6.
- [14] R.L. Pongratz, R.G. Kibbey, G.I. Shulman, G.W. Cline, Cytosolic and mitochondrial malic enzyme isoforms differentially control insulin secretion, *J. Biol. Chem.* 282 (2007) 200–207. doi:10.1074/jbc.M602954200.
- [15] K. Smolková, P. Ježek, The role of mitochondrial NADPH-dependent isocitrate

- dehydrogenase in cancer cells, Hindawi, 2012. doi:10.1155/2012/273947.
- [16] N.I. Krupenko, M.E. Dubard, K.C. Strickland, K.M. Moxley, N. V Oleinik, S.A. Krupenko, ALDH1L2 is the mitochondrial homolog of 10-formyltetrahydrofolate dehydrogenase, *J. Biol. Chem.* 285 (2010) 23056–23063. doi:10.1074/jbc.M110.128843.
- [17] M. Shin, J. Momb, D.R. Appling, Human mitochondrial MTHFD2 is a dual redox cofactor-specific methylenetetrahydrofolate dehydrogenase/methenyltetrahydrofolate cyclohydrolase, *Cancer Metab.* 5 (2017) 11. doi:10.1186/s40170-017-0173-0.
- [18] P.M. Tedeschi, A. Vazquez, J.E. Kerrigan, J.R. Bertino, Mitochondrial Methylenetetrahydrofolate Dehydrogenase (MTHFD2) Overexpression Is Associated with Tumor Cell Proliferation and Is a Novel Target for Drug Development, *Mol. Cancer Res.* 13 (2015) 1361–1366. doi:10.1158/1541-7786.MCR-15-0117.
- [19] J. Fan, J. Ye, J.J. Kamphorst, T. Shlomi, C.B. Thompson, J.D. Rabinowitz, Quantitative flux analysis reveals folate-dependent NADPH production, *Nature.* 510 (2014) 298–302. doi:10.1038/nature13236.
- [20] J. Ye, J. Fan, S. Venneti, Y.W. Wan, B.R. Pawel, J. Zhang, L.W.S. Finley, C. Lu, T. Lindsten, J.R. Cross, G. Qing, Z. Liu, M. Celeste Simon, J.D. Rabinowitz, C.B. Thompson, Serine catabolism regulates mitochondrial redox control during hypoxia, *Cancer Discov.* 4 (2014) 1406–1417. doi:10.1158/2159-8290.CD-14-0250.
- [21] D. Samanta, Y. Park, S.A. Andrabi, L.M. Shelton, D.M. Gilkes, G.L. Semenza, PHGDH expression is required for mitochondrial redox homeostasis, breast cancer stem cell maintenance, and lung metastasis, *Cancer Res.* 76 (2016) 4430–4442. doi:10.1158/0008-5472.CAN-16-0530.
- [22] M. Yang, K.H. Vousden, Serine and one-carbon metabolism in cancer, *Nat. Rev. Cancer.*

- 16 (2016) 650–662. doi:10.1038/nrc.2016.81.
- [23] M.J. Lukey, K.S. Greene, J.W. Erickson, K.F. Wilson, R.A. Cerione, The oncogenic transcription factor c-Jun regulates glutaminase expression and sensitizes cells to glutaminase-targeted therapy, *Nat. Commun.* 7 (2016). doi:10.1038/ncomms11321.
- [24] P.D. Ray, B.-W. Huang, Y. Tsuji, Reactive oxygen species (ROS) homeostasis and redox regulation in cellular signaling, *Cell. Signal.* 24 (2012) 981–990.
doi:10.1016/j.cellsig.2012.01.008.
- [25] I. Papandreou, R.A. Cairns, L. Fontana, A.L. Lim, N.C. Denko, HIF-1 mediates adaptation to hypoxia by actively downregulating mitochondrial oxygen consumption, *Cell Metab.* 3 (2006) 187–197. doi:10.1016/j.cmet.2006.01.012.
- [26] L. Jin, D. Li, G.N. Alesi, J. Fan, H.B. Kang, Z. Lu, T.J. Boggon, P. Jin, H. Yi, E.R. Wright, D. Duong, N.T. Seyfried, R. Egnatchik, R.J. DeBerardinis, K.R. Magliocca, C. He, M.L. Arellano, J.H.J. Khoury, D.M. Shin, F.R. Khuri, S. Kang, Glutamate Dehydrogenase 1 Signals through Antioxidant Glutathione Peroxidase 1 to Regulate Redox Homeostasis and Tumor Growth, *Cancer Cell.* 27 (2015) 257–270.
doi:10.1016/j.ccell.2014.12.006.
- [27] P.A. Gameiro, L.A. Laviolette, J.K. Kelleher, O. Iliopoulos, G. Stephanopoulos, Cofactor balance by nicotinamide nucleotide transhydrogenase (NNT) coordinates reductive carboxylation and glucose catabolism in the tricarboxylic acid (TCA) cycle, *J. Biol. Chem.* 288 (2013) 12967–12977. doi:10.1074/jbc.M112.396796.
- [28] A.R. Mullen, W.W. Wheaton, E.S. Jin, P.-H. Chen, L.B. Sullivan, T. Cheng, Y. Yang, W.M. Linehan, N.S. Chandel, R.J. DeBerardinis, Reductive carboxylation supports growth in tumour cells with defective mitochondria., *Nature.* 481 (2011) 385–8.

doi:10.1038/nature10642.

- [29] D.R. Wise, P.S. Ward, J.E.S. Shay, J.R. Cross, J.J. Gruber, U.M. Sachdeva, J.M. Platt, R.G. DeMatteo, M.C. Simon, C.B. Thompson, Hypoxia promotes isocitrate dehydrogenase-dependent carboxylation of α -ketoglutarate to citrate to support cell growth and viability, *Proc. Natl. Acad. Sci.* 108 (2011) 19611–19616.
doi:10.1073/pnas.1117773108.
- [30] D.T. Hartong, M. Dange, T.L. McGee, E.L. Berson, T.P. Dryja, R.F. Colman, Insights from retinitis pigmentosa into the roles of isocitrate dehydrogenases in the Krebs cycle, *Nat. Genet.* 40 (2008) 1230–1234. doi:10.1038/ng.223.
- [31] C.M. Metallo, P.A. Gameiro, E.L. Bell, K.R. Mattaini, J. Yang, K. Hiller, C.M. Jewell, Z.R. Johnson, D.J. Irvine, L. Guarente, J.K. Kelleher, M.G. Vander Heiden, O. Iliopoulos, G. Stephanopoulos, Reductive glutamine metabolism by IDH1 mediates lipogenesis under hypoxia, *Nature.* 481 (2012) 380–384. doi:10.1038/nature10602.
- [32] L. Jiang, A. a Shestov, P. Swain, C. Yang, S.J. Parker, Q. a Wang, L.S. Terada, N.D. Adams, M.T. McCabe, B. Pietrak, S. Schmidt, C.M. Metallo, B.P. Dranka, B. Schwartz, R.J. DeBerardinis, Reductive carboxylation supports redox homeostasis during anchorage-independent growth., *Nature.* 532 (2016) 255–258. doi:10.1038/nature17393.
- [33] J. Zhang, W.S. Ahn, P.A. Gameiro, M.A. Keibler, Z. Zhang, G. Stephanopoulos, ^{13}C isotope-assisted methods for quantifying glutamine metabolism in cancer cells, *Methods Enzymol.* 542 (2014) 369–389. doi:10.1016/B978-0-12-416618-9.00019-4.

CHAPTER 5

CONCLUDING REMARKS AND FUTURE DIRECTIONS

In this dissertation, I have presented three individual research projects that fall under my broad research interest.

5-1 Chapter 2

In Chapter 2, I discussed our experimental efforts towards understanding of anastomosis *in vitro*. In this study, we exploited a three-dimensional (3-D) culture platform to examine the dynamics of endothelial cells (ECs) during and after vascular anastomosis by allowing angiogenesis and vasculogenesis to proceed in parallel. We showed that anastomosis occurs between sprouts formed by angiogenesis from an endothelium and tubes formed by vasculogenesis in the bulk of a 3-D matrix. This fusion leads to highly connected vessels that span from the surface of the matrix into the bulk in a manner that depends on cell density and identity. We further observed and analyzed intermixing of endothelial cells of distinct origin (surface versus bulk) within the vessels structures that are formed. Additionally, we provided evidence that the cells migrate along pre-existing vessels segments as part of this intermixing process. We concluded that anastomosis can occur between vessels emerging by angiogenesis and vasculogenesis and that this process may play an important role in contexts such as wound healing.

The experimental configuration we proposed in this study can potentially provide a new route to study anastomosis *in vitro*. With this platform, anastomosis can be

quickly established, allowing for high throughput examination of impact on anastomosis due to various tunable variables. The strategy of achieving anastomosis through induction of angiogenesis and vasculogenesis in parallel can also be exploited and applied to a microfluidic platform, a step closer towards generating large constructs of vascularized engineered tissue.

Here, I propose a few future directions that can be extended upon this study. From the fundamental perspective, a protocol that leads to initiation of angiogenesis and vasculogenesis utilizing a more physiological relevant agent other than PMA needs to be established. Previous literature has pointed to S1P as a potential candidate to replace PMA for inducing angiogenesis *in vitro* [1]. However, detailed analysis comparing PMA and S1P in angiogenesis, vasculogenesis and anastomosis needs to be performed, possibly enabled by our experimental configuration discussed in Chapter 2. From the application perspective, extending our strategy of inducing anastomosis to a microfluidic platform could significantly simplify the design of the device itself to achieve the same percolated vascular structure *in vitro* at a larger scale. However, to scale from a static 3-D culture system to a microfluidic format, several challenges remain to be addressed. For example, interstitial fluid pressure needs to be established and maintained at physiological level to sustain the health of established vasculature [2].

There still exist numerous questions that must be explored to enable the construction of large-scale living tissues. Our study nonetheless provides a basis for the fundamental and application perspectives towards this ultimate goal.

5-2 Chapter 3

In Chapter 3, I discussed how we developed a multi-scale modeling platform to elucidate the distinct outcomes in population-scale growth dynamics under three different metabolic scenarios: the Warburg effect, the reverse Warburg effect and glutamine addiction. At the intracellular level, we constructed a reduced representation of central metabolism and performed flux balance analysis (FBA) to estimate metabolic fluxes; at the cellular level, we exploited this metabolic network to calculate parameters for a coarse-grained description of cellular growth kinetics; and at the multicellular level, we incorporated these kinetic schemes into the cellular automata of an agent-based model (ABM), iDynoMiCS. This ABM evaluates the reaction-diffusion of the metabolites, cellular division and motion over a simulation domain.

Our multi-scale simulations suggested that the Warburg effect provides a growth advantage to the tumor cells under resource limitation. Further, we identified a non-monotonic dependence of growth rate on the strength of glycolytic pathway. On the other hand, the reverse Warburg scenario provides an initial growth advantage in tumors that originate deeper in the tissue. The metabolic profile of stromal cells considered in this scenario allows more oxygen to reach the tumor cells in the deeper tissue and thus promotes tumor growth at earlier stages. Lastly, we suggested that glutamine addiction does not confer a selective advantage to tumor growth with glutamine acting as a carbon source in the tricarboxylic acid (TCA) cycle; any advantage of glutamine uptake must come through other pathways not included in our model (e.g., as a nitrogen donor). Our analysis illustrated the importance of accounting explicitly for spatial and temporal evolution of tumor microenvironment for the interpretation of metabolic scenarios and

hence provided a basis for further studies, including evaluation of specific therapeutic strategies that target metabolism.

Additionally, our modeling platform can be exploited to study the impact of tumor phenotypic heterogeneity [3–5] on solid tumor growth. The phenotypic heterogeneity can be interpreted as diverse metabolic states at the intracellular level; integrated into the ABM at the cellular level and potentially made dynamically adaptive based on local microenvironment (e.g. concentration of metabolites) at the tissue scale.

As the field of cancer metabolism quickly advances, novel observations and hypotheses are being made every day to address the metabolic profile of different tumor types. Our scale-bridging computational framework can serve as a powerful tool that enables rapid evaluation of these emerging hypotheses in cancer metabolism.

5-3 *Chapter 4*

In Chapter 4, I presented some of our initial efforts exploring how breast cancer cells mitigate mitochondrial redox stress under chronic hypoxia. I discussed the state-of-the-art understanding of tumor hypoxia in regulating cellular functions and the potential strategies that tumor cells adopt to combat the redox stress induced by hypoxia. I further emphasized the importance of compartmentalized metabolic reactions to modulate NADP⁺/NADPH ratio and thus regulating the subcellular ROS levels. Our immunoblot results revealed that most of the NADPH sources are “turned off” and pointed to IDH2 in producing NADPH under chronic hypoxia. Our results contradicted what has been established in the literature with experimental supports collected under short-term hypoxia and thus clarified the time-dependence of hypoxia-induced metabolic adaptations in breast cancer cells. These results have also led us to propose an IDH-

mediated redox shuttle that transfers NADPH into the mitochondria. In this hypothesis, the mitochondrial isocitrate dehydrogenase (IDH2) catalyzes the reaction from isocitrate to α KG in the oxidative direction under hypoxia and yields NADPH to mitigate mitochondrial ROS. On the other hand, the produced α KG transfers to cytosol and participates in reductive carboxylation via IDH1 to produce isocitrate and further citrate to fuel lipid synthesis.

Apart from the follow-up experiments mentioned in **Chapter 4**, one significant question remains: what is the primary role of glutamine via anaplerosis under chronic hypoxia – does it serve as a redox regulator or simply a carbon source for lipid synthesis? To determine whether glutamine is the main contributor to redox regulation in the mitochondria, glutaminase inhibitors such as BPTES can be used to treat breast cancer cells followed by ROS measurement. Additionally, proliferation assays can be performed for BPTES-treated breast cancer cells supplemented with or without citrate to determine the contribution of glutamine to lipid synthesis as a carbon source under chronic hypoxia. Since glutamine addiction is a tissue-specific metabolic trait and often influenced by tumor microenvironment [6,7], it is important to study the specific roles of glutamine in tumor metabolism under defined contexts such as chronic hypoxia. These proposed explorations of glutamine metabolism in tumor cells can advance our understanding in the fundamentals of tumor metabolism and further points to potential therapeutic strategies in treating cancer.

Additionally, as an extension to both the intracellular scale computational tool depicted in chapter 4 (FBA) and this study, a small-scale FBA network concerning only

the redox-coupled metabolic reactions in the cells can be established and allows for more vigorous testing of our hypothesis.

In summary, the three research studies in this dissertation represent my ambitious attempts at exploring different perspectives revolved around the cell-tissue dynamics. While these works remain preliminary, the findings in these works nonetheless contribute a piece of knowledge to the foundation of the corresponding research field.

5-4 *References*

- [1] K.J. Bayless, G.E. Davis, Sphingosine-1-phosphate markedly induces matrix metalloproteinase and integrin-dependent human endothelial cell invasion and lumen formation in three-dimensional collagen and fibrin matrices, *Biochem. Biophys. Res. Commun.* 312 (2003) 903–913. doi:10.1016/j.bbrc.2003.11.017.
- [2] J. Tien, L. Li, O. Ozsun, K.L. Ekinici, Dynamics of Interstitial Fluid Pressure in Extracellular Matrix Hydrogels in Microfluidic Devices, *J. Biomech. Eng.* 137 (2015) 91009. doi:10.1115/1.4031020.
- [3] T.L. Yuan, G. Wulf, L. Burga, L.C. Cantley, Cell-to-cell variability in PI3K protein level regulates PI3K-AKT pathway activity in cell populations, *Curr. Biol.* 21 (2011) 173–183. doi:10.1016/j.cub.2010.12.047.
- [4] M. Robertson-Tessi, R.J. Gillies, R.A. Gatenby, A.R.A. Anderson, Impact of metabolic heterogeneity on tumor growth, invasion, and treatment outcomes, *Cancer Res.* 75 (2015) 1567–1579. doi:10.1158/0008-5472.CAN-14-1428.
- [5] B. Waclaw, I. Bozic, M.E. Pittman, R.H. Hruban, B. Vogelstein, M. a. Nowak, A spatial model predicts that dispersal and cell turnover limit intratumour heterogeneity, *Nature.* (2015). doi:10.1038/nature14971.

- [6] A. Muir, L. V Danai, D.Y. Gui, C.Y. Waingarten, C.A. Lewis, M.G. Vander Heiden, Environmental cystine drives glutamine anaplerosis and sensitizes cancer cells to glutaminase inhibition, *Elife*. 6 (2017) e27713. doi:10.7554/eLife.27713.
- [7] A.A. Cluntun, M.J. Lukey, R.A. Cerione, J.W. Locasale, Glutamine Metabolism in Cancer: Understanding the Heterogeneity, *Trends in Cancer*. 0 (2017) 1–12. doi:10.1016/j.trecan.2017.01.005.